


University of Alberta

**Sorption of Athabasca Vacuum Residue on Acidic, Neutral
and Basic Surfaces**

by

Cheng Xing 

A thesis submitted to the Faculty of Graduate Studies and Research
in partial fulfillment of the requirements for the degree of

Master of Science
In
Chemical Engineering

Department of Chemical and Materials Engineering

Edmonton, Alberta

Fall 2008



Library and
Archives Canada

Bibliothèque et
Archives Canada

Published Heritage
Branch

Direction du
Patrimoine de l'édition

395 Wellington Street
Ottawa ON K1A 0N4
Canada

395, rue Wellington
Ottawa ON K1A 0N4
Canada

Your file *Votre référence*
ISBN: 978-0-494-47444-0
Our file *Notre référence*
ISBN: 978-0-494-47444-0

NOTICE:

The author has granted a non-exclusive license allowing Library and Archives Canada to reproduce, publish, archive, preserve, conserve, communicate to the public by telecommunication or on the Internet, loan, distribute and sell theses worldwide, for commercial or non-commercial purposes, in microform, paper, electronic and/or any other formats.

The author retains copyright ownership and moral rights in this thesis. Neither the thesis nor substantial extracts from it may be printed or otherwise reproduced without the author's permission.

AVIS:

L'auteur a accordé une licence non exclusive permettant à la Bibliothèque et Archives Canada de reproduire, publier, archiver, sauvegarder, conserver, transmettre au public par télécommunication ou par l'Internet, prêter, distribuer et vendre des thèses partout dans le monde, à des fins commerciales ou autres, sur support microforme, papier, électronique et/ou autres formats.

L'auteur conserve la propriété du droit d'auteur et des droits moraux qui protègent cette thèse. Ni la thèse ni des extraits substantiels de celle-ci ne doivent être imprimés ou autrement reproduits sans son autorisation.

In compliance with the Canadian Privacy Act some supporting forms may have been removed from this thesis.

Conformément à la loi canadienne sur la protection de la vie privée, quelques formulaires secondaires ont été enlevés de cette thèse.

While these forms may be included in the document page count, their removal does not represent any loss of content from the thesis.

Bien que ces formulaires aient inclus dans la pagination, il n'y aura aucun contenu manquant.


Canada

ABSTRACT

Asphaltene deposition occurs in hydrocarbon resource production, transport and refining processes and remains a challenging problem for industry. Zou and Shaw (2002) showed that Athabasca Bitumen Vacuum Residue (ABVB) + pentane mixtures deposit thin adherent films on stainless steel surfaces at unexpected conditions. This finding is the starting point for work reported here where deposit thickness and composition from this mixture are explored on well defined acidic (FeS, SiO₂), basic (FeO) and neutral (Ni/NiO) surfaces. Control experiments involving model compound deposition were used to confirm experimental protocols, and to address surface contamination issues, which interfere with organic deposit composition measurements, particularly if the organic deposit is thin, or surface coverage is partial. The XPS results show that for both model compounds and ABVB, surface properties affect both deposit thickness and deposit composition. Organic deposits from ABVB + pentane mixtures comprise a mix of asphaltenes + other constituents on all surfaces. On the neutral and basic surfaces, the deposit is asphaltene enriched relative to the feed; on the acidic surfaces, the deposit is depleted in asphaltenes relative to ABVB. Further chemical analysis of organic deposits is warranted.

ACKNOWLEDGEMENTS

I am deeply grateful to those people whose support and assistance have accompanied me along the journey of this work. The project would not have been successful without the incessant guidance and endless encouragement from my supervisor Dr. John Shaw. He has been an invaluable resource and his direction is truly outstanding.

I would like to thank Bei Zhao, Nima Saber, Kasra Nikooyeeh and Xiaohui Zhang for their constructive criticism and valuable suggestions, which made this project successful.

A helpful discussion with Amit Rudrake from Queens University is also greatly appreciated. I would also like to thank all the members in Petroleum Thermodynamics group and all supporting staff in the Department of Chemical and Materials Engineering at the University of Alberta. Without their help and cooperation, this undertaking would not have been possible.

I am grateful to the NanoFab and machine shop at the University of Alberta for the preparation of piranha solution and construction of batch reactors in a timely manner. I am thankful to Prof. Dave Mitlin, Colin Ophus and Christopher Harrower for their help with sputtering and to Prof. Gray for use of the sand bath. I am indebted to the Alberta Centre for Surface Engineering and Science for XPS analysis. Special thanks should go

to Dr. Dimitre Karpuzov, Dr. Anquang He and Shihong Xu for their contribution to this project.

I gratefully acknowledge the scholarship program at the University of Alberta and research funds from the sponsors of the NSERC Industrial Research Chair in Petroleum Thermodynamics (Alberta Energy Research Institute, ConocoPhillips, Halliburton Energy Services Ltd., Imperial Oil Resources, KBR, NEXEN, Shell Canada Ltd., Total E&P Canada, and NSERC).

Special thanks to my girl friend, Siyan Wu, for her love and encouragement, to make one of the most important steps in my life successful.

No words could express my deep gratitude to my parents, my father Dunping Xing and my mother Zhenggui Zhou, for their sacrifices and for giving me this opportunity to pursue a higher education. The success of this work is attributed to their ceaseless encouragement, support and love.

TABLE OF CONTENTS

Chapter 1	Introduction	1
1.1	Background	1
1.1.1	Heavy Oil and Bitumen: Prospective Energy Resource	1
1.1.2	Characteristics and Upgrading of Heavy Oil and Bitumen	1
1.1.3	Asphaltene Deposition in Heavy Oil and Bitumen Production Transport and Refining	5
1.2	Motivation	6
1.3	Objectives	8
1.4	Thesis outline	9
Chapter 2	Literature Review	10
2.1	Bitumen Characterization	10
2.2	Asphaltene Precipitation	11
2.2.1	What are Asphaltenes?	11
2.2.2	Molecular Structure of Asphaltenes	14
2.2.3	Asphaltene Precipitation	17
2.3	Naphthenic Acid Corrosion and Deposition	18
2.3.1	What is Naphthenic Acid?	18
2.3.2	Characterization of Naphthenic Acid	19

2.3.3 Metal Naphthenate Deposition	22
2.4 Surfaces	24
2.5 Surface Sorption	25
2.5.1 Definitions	25
2.5.2 Organic molecule sorption on to Metal oxide/sulfide surfaces	26
2.6 Literature Review Summary	28
Chapter 3 Experimental	30
3.1 Introduction	30
3.2 Materials	30
3.3 Surface Construction	35
3.3.1 Removal of the Surface Oxidation Layer from Silicon Wafers	35
3.3.2 Iron Oxide, Nickel Surface Formation (Sputtering)	39
3.3.3 Iron Sulfide Surface Formation (Sulfidation of Iron Sulfide Surface)	41
3.4 Surface Compositions	42
3.5 Control Experiments	43
3.5.1 Negative Controls	43
3.5.2 Positive Controls	43
3.6 Bitumen Deposition Experiments	44
3.6.1 Experimental Surfaces	44
3.6.2 Experimental Approach and Procedure	45
3.6.3 Experimental Matrix	47

3.7 Deposit Property Measurement -----	49
3.7.1 X-ray Photoelectron Spectroscopy (XPS) -----	49
3.7.2 Thickness of Deposit -----	52
3.7.3 Composition of Deposit -----	55
3.8 Error Analysis -----	60
3.8.1 Errors from Sample Preparation -----	60
3.8.2 Errors from Analysis -----	61
Chapter 4 Results and Discussion -----	63
4.1 Introduction -----	63
4.2 Surface Composition and Contamination -----	63
4.2.1 Contaminated Surface Compositions -----	63
4.2.2 Composition and Contamination of the Iron Oxide Surface -----	64
4.2.3 Composition and Contamination of the Iron Sulfide Surface -----	66
4.2.4 Composition and Contamination of the Nickel Surface -----	69
4.2.5 Composition and Contamination of the Silicon Surface -----	72
4.2.6 Substrate Composition Summary -----	74
4.3 Deposition of Model Compounds -----	75
4.3.1 Negative Controls -----	75
4.3.2 Positive Controls -----	76
4.4 Deposition of Athabasca Bitumen Constituents -----	82
4.4.1 Thickness of Deposits on Basic Surfaces -----	82

4.4.2 Thickness of Deposits on Neutral Surfaces -----	84
4.4.3 Thickness of Deposits on Acidic Surfaces-----	85
4.4.4 Comparison of Thickness of Deposits on all Surfaces-----	86
4.5 ABVB Deposit Composition -----	89
4.5.1 Composition of Deposit on Basic Surfaces-----	89
4.5.2 Composition of Deposit on Neutral Surfaces -----	91
4.5.3 Composition of Deposit on Acidic Surfaces -----	93
4.5.3 Composition of Deposit on Acidic Surfaces -----	94
4.5.4 Comparison of Composition of ABVB Deposits on all Surfaces -----	95
Chapter 5 Conclusions and Future Work -----	99
5.1 Conclusions -----	99
5.2 Future Work-----	100
REFERENCES-----	102

LIST OF TABLES

Table 1.1: Definition of oil type by API gravity and density-----	2
Table 2.1: Major naphthenic acid types -----	21
Table 3.1: Composition of ABVB -----	32
Table 3.2: Chemicals used, their purities and suppliers -----	33
Table 3.3: Physical and chemical properties of pentane -----	33
Table 3.4: Sputtering targets -----	34
Table 3.5: Sputtering parameters -----	41
Table 3.6: Iron oxide surface characterization -----	42
Table 3.7: Experimental matrix for evaluation of mixtures of ABVB and pentane on iron oxide, nickel and silica surfaces with fixed ABVB mass fraction -----	48
Table 3.8: Experimental matrix for evaluation of mixtures of ABVB and pentane on iron oxide, nickel and silica surfaces at different ABVB composition -----	49
Table 3.9: Elemental composition of ABVB -----	57
Table 3.10: Elemental composition of ABVB relative to sulfur -----	57
Table 3.11: Surface composition of iron oxide film (137 nm) -----	58
Table 3.12: Raw composition data on the iron oxide surface -----	59
Table 3.13: Data corrected for contamination layer 1-----	59
Table 4.1: Composition of iron oxide, iron sulfide, nickel and silica surfaces (raw data) --- -----	64

Table 4.2: Surface composition on iron oxide and silica surfaces for pentane -----	75
Table 4.3: Surface composition on iron oxide and silica surfaces for pentane + pyrene--	76
Table 4.4: Surface composition on iron oxide and silica surfaces for naphthenic acid ---	77
Table 4.5: Surface composition on iron oxide and silica surfaces for naphthenic acid (15 wt %) + pentane -----	78
Table 4.6: Surface composition on iron oxide and silica surfaces for zinc naphthenate (45 wt %) + pentane -----	79
Table 4.7: Surface composition on iron oxide and silica surfaces for zinc TPP (15 wt %) + pentane -----	80
Table 4.8: Surface composition on iron oxide and silica surfaces for nickel TPP (15 wt %) + pentane -----	81
Table 4.9: Deposit thickness for model compounds-----	82
Table 4.10: Organic deposit thickness from experiment Set 1 and 2-----	88
Table 4.11: C1/S ratio from experiment Set 1 and 2-----	98

LIST OF FIGURES

Figure 1.1: A simplified bitumen upgrading scheme -----	4
Figure 1.2: Temperature at which the stirrer sticks to the base plate -----	7
Figure 1.3: Phase behaviour of ABVB + pentane mixtures at 160 C -----	8
Figure 2.1: Simplified petroleum fractionation method -----	11
Figure 2.2: Examples of the appearance (magnified about 15 times) of asphaltenes separated from Mars-P crude oil with an excess of (a) pentane (n-C5) and (b) heptane (n-C7)-----	13
Figure 2.3: “Long diagram” shows that the asphaltenes include the crude oil material highest in molecular weight, polarity, and/or aromaticity molecular weight, polarity, and/or aromaticity -----	14
Figure 2.4: Average structure of Athabasca asphaltene molecules -----	16
Figure 2.5: (a) General naphthenic acid; (b) Cyclopentane -----	20
Figure 2.6: Naphthenate deposits in crude oil processing equipment -----	22
Figure 2.7: Summary of pyridine bonding modes: (a) $\eta^1(\text{N})\text{-Py-}90^\circ$; (b) $\eta^6\text{-Py-}0^\circ$; (c) $\eta^1(\text{C}2)\text{-Py-}90^\circ$; (d) $\eta^2(\text{C}2,\text{C}3)\text{-Py-}90^\circ$; (e) $\eta^2(\text{N},\text{C}2)\text{-Py-}90^\circ$; (f) $\eta^2(\text{N},\text{C}2)\text{-}$ pyridyl; (g) $\mu_2, \eta^1(\text{N})\text{-Py-}90^\circ$; (h) $\mu_2, \eta^2(\text{N},\text{C}2)\text{-Py-}90^\circ$ -----	27
Figure 2.8: Adsorption configurations of pyrrole on Mo(110): (a) $\mu_3, \eta^5\text{-Pyr-}0^\circ$; (b) $\mu_3,$ $\eta^4(\text{N},\text{C}2,\text{C}4,\text{C}5)\text{-Pyr-}0^\circ$; (c) $\mu_3, \eta^4(\text{N},\text{C}2,\text{C}3,\text{C}4)\text{-Pyr-}5^\circ$ -----	28
Figure 3.1: Silicon wafer -----	34

Figure 3.2: Oxidation of silicon wafer surface -----	35
Figure 3.3: Schematic diagram of sputtering process -----	39
Figure 3.4: ATC ORION 5 UHV Sputtering system -----	40
Figure 3.5: An idealized model of the deposition substrate -----	45
Figure 3.6: Experimental setup (a) wafer sample; (b) batch reactor; (c) reactor in oven detail; (d) Oven-----	46
Figure 3.7: (a) Deposition schematic; (b) Image of liquid film + deposit; (c) Image of surface deposit following a pentane wash -----	47
Figure 3.8: Schematic diagram of X-ray photoelectron spectroscopy -----	51
Figure 3.9: Diagram of P(d) function -----	53
Figure 3.10: Model of film thickness calculation -----	54
Figure 3.11: Contamination model -----	58
Figure 4.1: The O 1s high-resolution XPS spectrum for the iron oxide surface -----	65
Figure 4.2: The C 1s high-resolution XPS spectrum for the iron oxide surface -----	65
Figure 4.3: The O 1S high-resolution spectrum for the iron sulfide surface -----	68
Figure 4.4: The C 1S high-resolution spectrum for the iron sulfide surface -----	68
Figure 4.5: The O 1s high-resolution XPS spectrum for the nickel surface -----	71
Figure 4.6: The C 1s high-resolution XPS spectrum for the nickel surface -----	71
Figure 4.7: The O 1s high-resolution XPS spectrum for the silicon surface -----	73
Figure 4.8: The C 1s high-resolution XPS spectrum for the silicon surface -----	73
Figure 4.9: Surface used in the organic deposition experiments -----	74

Figure 4.10: Thickness of deposit on the iron oxide surface vs. t_1 at $t_2 = 30$ minutes----	83
Figure 4.11: Thickness of deposit on the iron oxide surface vs. t_2 at $t_1 = 3.5$ hours-----	83
Figure 4.12: Thickness of deposit on the nickel surface vs. t_1 at $t_2 = 30$ minutes-----	84
Figure 4.13: Thickness of deposit on the silica surface vs. t_1 at $t_2 = 30$ minutes-----	85
Figure 4.14: Thickness of deposits on iron oxide, nickel, iron sulfide and silica surfaces vs. t_1 at $t_2 = 30$ minutes-----	87
Figure 4.15: Thickness of deposits on iron Oxide, nickel and silica surfaces vs. ABVB mass fraction at $t_1 = 3.5$ hours and $t_2 = 30$ minutes. The numbers of repetitions of each experiment is a parameter.)-----	87
Figure 4.16: Connection between thickness of deposit and phase behavior -----	88
Figure 4.17: C1/S on iron oxide surface vs. t_1 at $t_2 = 30$ minutes and ABVB composition = 15 wt %-----	90
Figure 4.18: C1/S on iron oxide surface vs. t_2 at $t_1 = 3.5$ hours-----	90
Figure 4.19: C1/S on iron oxide surface at different ABVB mass fractions in pentane---	91
Figure 4.20: C1/S on nickel surface vs. t_1 $t_2 = 30$ minutes and ABVB composition = 15 wt %-----	93
Figure 4.21: C1/S on nickel surface at different ABVB mass fractions in pentane-----	93
Figure 4.22: C1/S on silica surface vs. t_1 at $t_2 = 30$ minutes and ABVB composition = 15 wt % -----	94
Figure 4.23: C1/S on silica surface at different ABVB mass fractions in pentane-----	95
Figure 4.24: C1/S ratio vs. t_1 on iron oxide, nickel and silica surfaces at $t_2 = 30$ minutes--	

-----96

Figure 4.25: C1/S ratio on iron oxide, nickel and silica surfaces as a function of ABVB wt

% in pentane-----97

Figure 4.26: Connection between C1/S ratio and phase behaviour ----- 97

NOMENCLATURE

Notation

t1	The time that substrate exposed to mixtures above phase boundary
t2	The time that substrate exposed to pentane at room temperature

Symbol

λ	Inelastic Mean Free Path
-----------	--------------------------

Abbreviations

ABVB	Athabasca Bitumen Vacuum Bottom
ACSES	Alberta Centre for Surface Engineering and Science
DC	Direct Current
DFT	Density-Functional Theory
FABMS	Fast Atom Bombardment Mass Spectrometry
FAT	Fixed Analyzer Transmission
FT-IR	Fourier Transform Infrared
GC-MS	Gas Chromatography-Mass Spectrometry
HOMO	Highest Occupied Orbital
LUMO	Lowest Unoccupied Orbital
IMPF	Inelastic Mean Free Path
MS	Mass Spectrometry
Nickel TPP	Tetraphenylporphine Nickel
NMR	Nuclear Magnetic Resonance
RF	Radio Frequency
SCO	Synthetic crude oil
SARA	Saturates, Aromatics, Resins, and Asphaltenes analysis

TAN	Total Acid Number
TPD	Temperature-Programmed Desorption
XPS	X-ray Photoelectron Spectroscopy
Zinc TPP	Tetraphenylporphine Zinc

Chapter 1 Introduction

1.1 Background

1.1.1 Heavy Oil and Bitumen: Prospective Energy Resource

As the world's supply of conventional light and sweet crude oil becomes depleted, heavy oil and bitumen have started playing a more and more crucial role in the energy industry. The petroleum industry is focusing on refining heavy oil and bitumen into light and sweet hydrocarbons to serve the increasing demand for fuels and petrochemicals. Oil Sands reserves are found in over 70 countries in the world. However, three quarters of the reserves are found in Venezuela and Canada, both of which have oil sands reserves approximately equal to the world's reserves of conventional crude oil. There are at least 1.7 trillion barrels of bitumen in Canada, particularly in Northern Alberta, which is about one third of world's petroleum resource. It is estimated that the production volume of synthetic crude oil (SCO) could be boosted to 3 million barrels per day by 2012, and even to 5 million barrels per day by 2030 to cover 16% of North America's demand for oil and gas¹.

1.1.2 Characteristics and Upgrading of Heavy Oil and Bitumen

Heavy Oil and bitumen are defined in terms of their physical properties. The characteristics of heavy oil and bitumen are quite different from those of conventional

crude oil. The American Petroleum Institute gravity (API gravity) is a measure of how heavy or light a petroleum liquid is compared to water. A classification of crude oil by API gravity and density is indicated in Table 1.1^{2,3}.

Table 1.1: Definition of oil type by API gravity and density

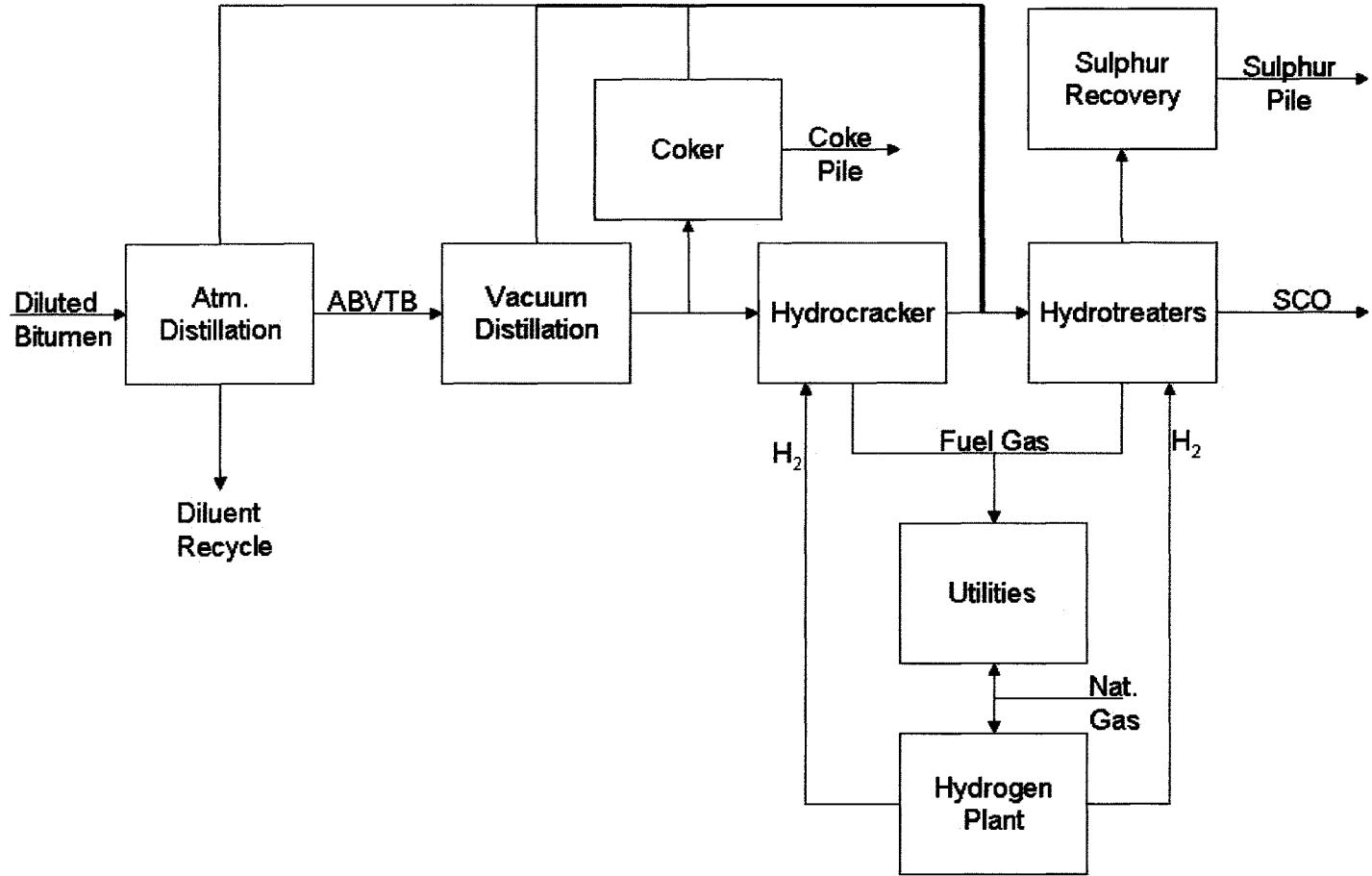
Crude Oil Type	Density	Viscosity	°API Gravity
	(g/cm ³)	(mPa·S)	
Light	0.87	< 10	> 31.1
Medium	0.92 - 0.87	10 - 100	22.3 - 31.1
Heavy	0.92 - 1.00	100 – 10,000	10 - 22.3
Extra-heavy or Bitumen	>1.00	> 10,000	<10

* API gravity and density are reported at a standard temperature of 15.6 °C.

The lighter the crude oil the easier the production of light valuable hydrocarbon and petrochemical products, i.e. naphtha, gasoline and diesel becomes. Moreover, high yields are usually achieved. Heavy crudes normally contain a significant amount of asphaltenes, vanadium, nickel, heteroatoms and inorganic fine solids⁴. Their hydrogen to oxygen ratio is also low. Consequently, the yield of production of light hydrocarbons is also low if only physical separation processes are used⁵. Reaction based upgrading processes are required to remove heteroatoms, and metals and to convert part of the heavy ends to lighter distillates before these heavy crudes can be used as feedstocks for existing conventional refinery processes.

A number of upgrading schemes have been developed and can be roughly classified into three types: first, catalytic cracking which includes the use of catalyst and heat to produce smaller molecules than those existing in the feedstock; second, hydrocracking which involves the use of hydrogen in the presence of a catalyst to produce compounds with higher H/C ratio; and third, thermal cracking which comprises the use of energy (high temperatures) to produce lighter compounds⁶. The product of upgrading processes is called synthetic crude oil, with no residue content, and can be sold as conventional light crude. A simplified bitumen upgrading scheme is presented in Figure 1.1⁷. There are two basic steps in this upgrading process, that is, primary upgrading and secondary upgrading. In primary upgrading, bitumen is separated into various streams of hydrocarbons by undertaking a series of physical separations. This stage begins with diluted bitumen fed into diluent recovery units where water is removed and naphtha is recovered to be recycled to extraction. The dry bitumen is then sent to a vacuum distillation unit. Light and heavy gas oil cuts are distilled off and sent to hydrotreaters while the vacuum residue (VTB) is sent to cokers or hydrocrackers. The vacuum residue, which comprises approximately 50 wt % of the bitumen, is significantly enriched in asphaltenes, heteroatoms and metals relative to the feed. Naphtha, light and heavy gas oil are produced in cokers through chemical reactions and then sent to hydrotreaters. Light and heavy gas oils are formed in hydrocrackers by hydrogen addition and then sent to hydrotreaters. In the second stage of upgrading, the impurities such as sulfur and nitrogen are removed from naphtha, light and heavy gas oil, which lead to the production of synthetic crude oil (SCO).

Figure 1.1: A simplified bitumen upgrading scheme



1.1.3 Asphaltene Deposition in Heavy Oil and Bitumen Production Transport and Refining

Many challenges are presented in heavy oil and bitumen production, transport and refining. One of the major challenges is solids drop out which results from high asphaltene and fine solids contents. It is widely recognized that asphaltene tend to form aggregates in hydrocarbon liquids⁸⁻¹¹. Asphaltene precipitation leads to a number of severe problems in reservoirs, in wells, in pipelines and in oil production and processing facilities^{11, 12}. Solid particles suspended in the crude oil may stick to the walls of the conduits and reservoirs. Asphaltenes can act as glue in consolidating deposits and, as a result, cause barriers to flow. For example, in Venezuela, the formation of asphaltene rich sludge has resulted in partial or complete plugging of wells¹³. Organic deposits in the North Sea and in the Gulf of Mexico have caused under-sea pipeline plugging with a substantial economic loss for oil production operations^{12, 14, 15}.

Other challenges in heavy oil and bitumen production process are due to the presence of heavy metals and heteroatom, mostly vanadium, nickel, nitrogen and oxygen. Although the mass fraction of these elements is quite small, they are concentrated in the asphaltene fraction and their impact is significant. They are responsible for problems from catalyst fouling to environmental damage^{2, 3, 16-18}.

1.2 Motivation

Asphaltene deposition arises in both current and proposed bitumen production (e.g., VAPEX) and refining (e.g., solvent de-asphalting) technologies where bitumen is diluted as a normal part of process operations. Previous work by our group has shown that, for example, Athabasca Bitumen Vacuum Residue (ABVB) + pentane mixtures deposit a thin adherent and sticky film on the stainless steel surfaces which can prevent a magnetically driven stirrer from rotating¹⁹. Figure 1.2 indicates that the temperature below which the stirrer sticks to the base plate even when no deposit is visible. Mixtures comprising 40 to 50 % ABVB are readily agitated at room temperature. At higher ABVB mass fractions, the stirrer becomes imbedded in bulk semi-solid organic material. This behavior is expected. However, the behavior at low ABVB mass fractions is unexpected. For example, mixtures comprising as little as 5% ABVB generate adherent and sticky deposits at a temperature even greater than 150 °C. It is this latter behavior that is the subject of this research and is expected to affect technology development and technology selection for numerous process applications.

This work is not being conducted in isolation. The phase behavior of ABVB + pentane mixtures has been studied previously¹⁹. A partial phase diagram is presented in Figure 1.3 where complex phase transitions and phase equilibria are observed over the mass fraction of ABVB range 0 to 100% at 160 C, a temperature just above where the deposition

becomes an issue. A link between the bulk phase behavior and deposit formation is anticipated. However, the composition of deposits is unknown. The impact of surface properties on deposition thickness or nature is also unknown. Considering the urgent need to deal with deposition and fouling problems, in general, a study aimed at understanding this well defined case is readily justified. Anticipated results are likely to be of broad interest.

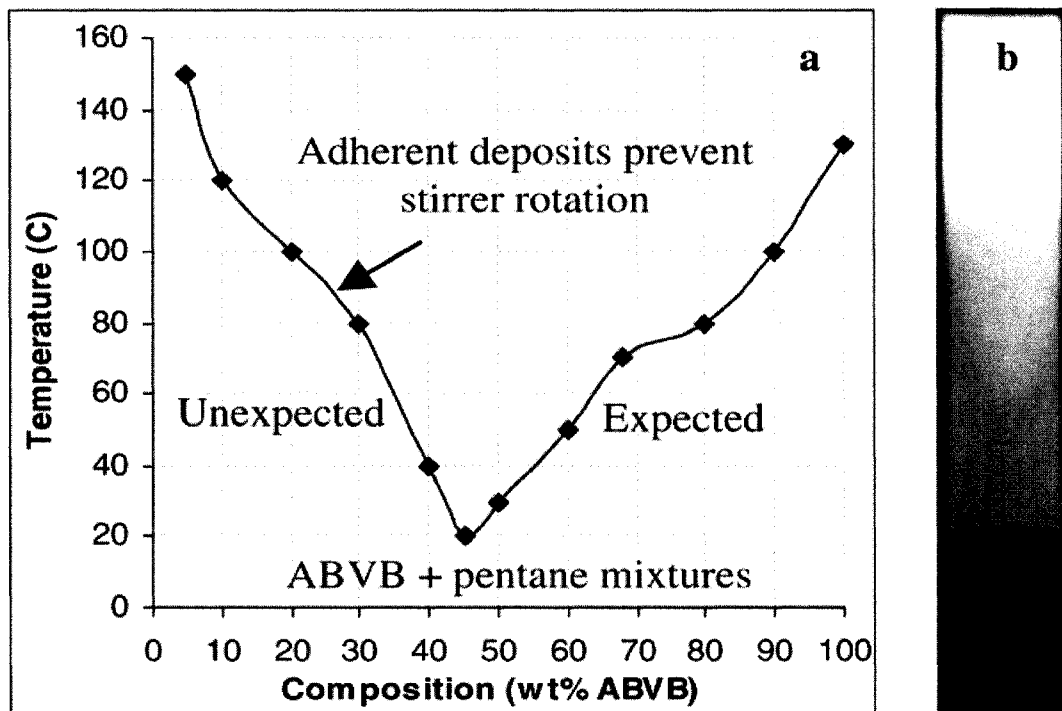


Figure 1.2: Temperature at which the stirrer sticks to the base plate

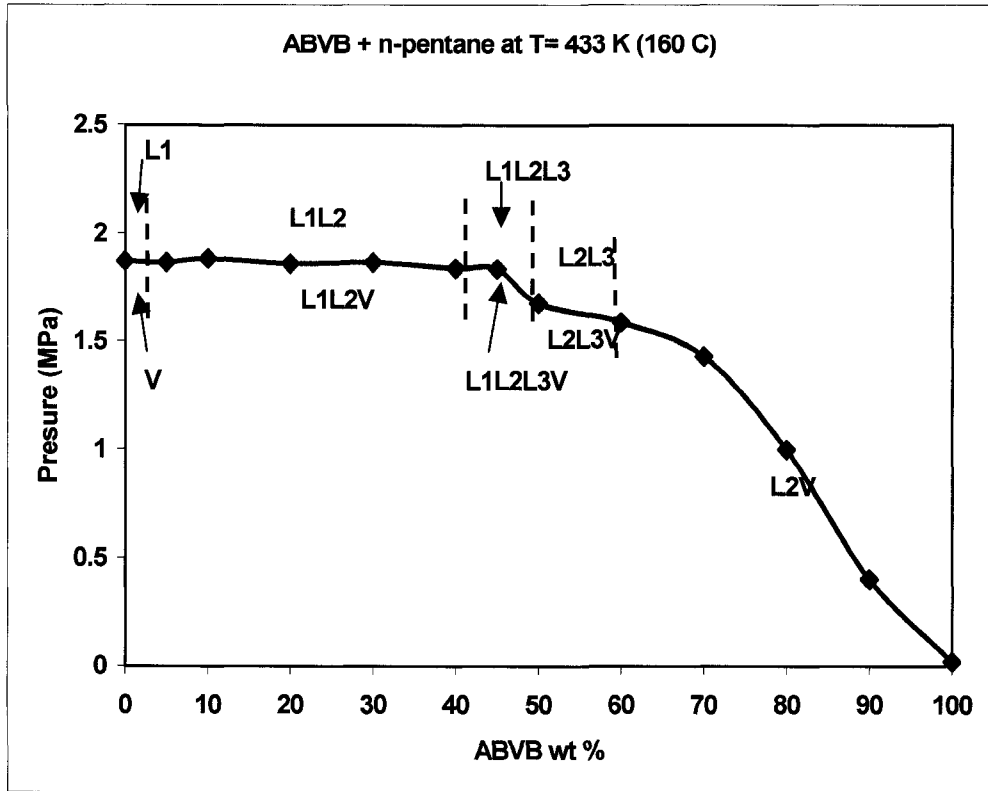


Figure 1.3: Phase behaviour of ABVB + pentane mixtures at 160 C

1.3 Objectives

In this exploratory experimental project, the details of the deposits formed from ABVB + pentane mixtures will be investigated. The specific research objectives are to:

1. prepare well defined acidic and basic surfaces;
2. perform benchmark deposition experiments with model compounds to validate the experimental approaches, and analytical methods;
3. evaluate the thickness and composition of deposits arising from ABVB + pentane

mixtures as a function of mixture composition, surface composition and exposure time variables.

1.4 Thesis outline

Following this brief introduction, a literature review related to this work is presented in Chapter 2 where asphaltene deposition and precipitation as well as naphthenic corrosion and deposition are discussed. These are the two most likely sources for the deposits observed in the prior work. Chapter 3 concerns experimental aspects of the work. Details related to the materials used, surface construction and surface impurities, control experiments, deposition experiment approach and procedure and error analysis are presented. Chapter 4 comprises the experimental results and discussion. Chapter 5 presents the conclusions and recommendations for future work.

Chapter 2 Literature Review

2.1 Bitumen Characterization

The characteristics of bitumen are quite different from those of conventional crude oils. They generally have a high specific gravity, a low hydrogen-to-carbon ratio, and contain large amounts of asphaltenes, heavy metals, heteroatom and inorganic fine solids²⁰. SARA analysis is the most common starting point for composition evaluation of hydrocarbons (ASTM D-2006, ASTM D-2007 and ASTM D-4124). During SARA analysis, samples are fractionated by selective precipitation (for asphaltenes) and/or chromatographic techniques as shown in Figure 2.1²¹. Generally, as the boiling temperature of heavy oil fraction increases, more resins and asphaltenes but less saturates are found. Inorganic fine solids, heavy metals and heteroatoms tend to concentrate in the heaviest fractions, such as resin and asphaltene^{16, 17, 22}. Elemental analysis simulated distillation and other more specialized analyses are also employed depending on the application. As the focus of this work is on surface deposition, where asphaltenes are expected to be present in deposits, SARA and elemental analysis of bitumen fractions²³ play a key role.

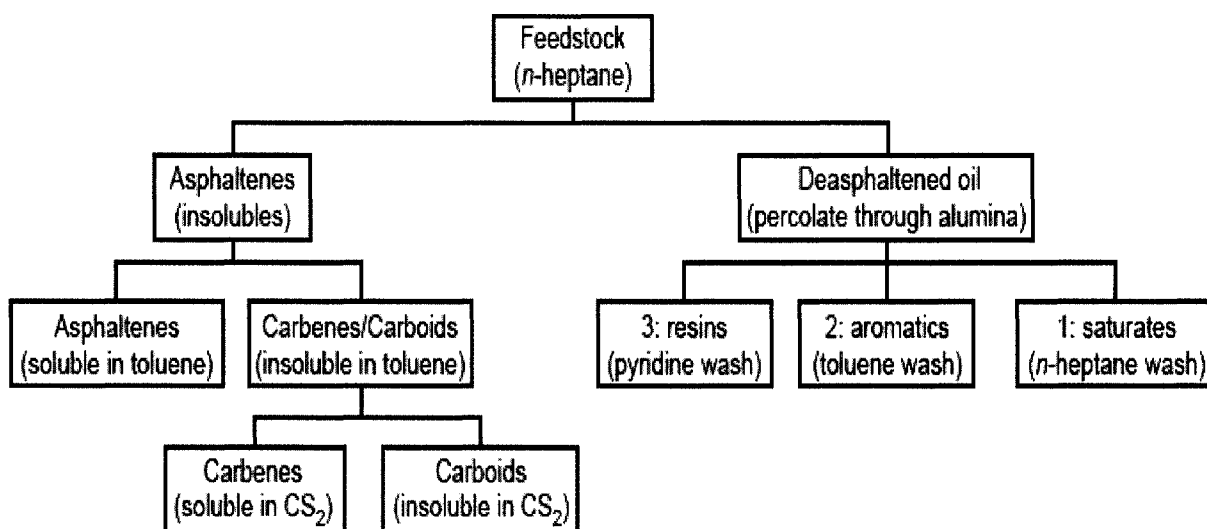


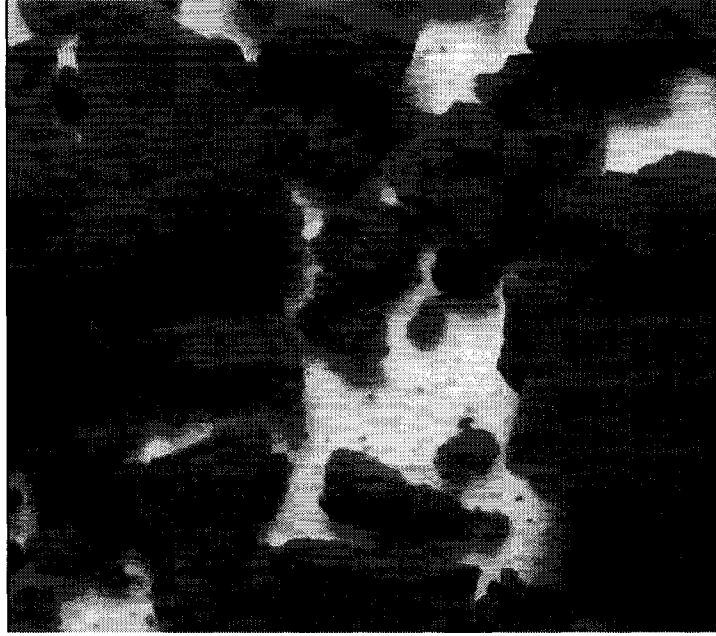
Figure 2.1: Simplified petroleum fractionation method

2.2 Asphaltene Precipitation

2.2.1 What are Asphaltenes?

Asphaltenes are defined operationally by the methods employed to isolate them and not by chemical structure. A common, if simplistic, definition of asphaltenes is that they are filterable from mixtures with *n*-pentane (or *n*-heptane) but not filterable from mixtures with benzene (or toluene)²⁴, using micron sized filters. The chemical composition of asphaltenes depends on many variables, including choice of alkane solvent, solvent volume, temperature, and time of mixing. For example, Figure 2.2 shows asphaltenes

separated from Mars-P crude oil using two different n-alkanes.²⁵ Both were formed in mixtures of 40 parts alkane to 1 part oil, and allowed to dry. Their appearance color and texture differ markedly.



(a) n-C₅ asphaltene



(b) n-C₇ asphaltene

Figure 2.2: Examples of the appearance (magnified about 15 times) of asphaltenes separated from Mars-P crude oil with an excess of (a) pentane (n-C₅) and (b) heptane (n-C₇)²⁵

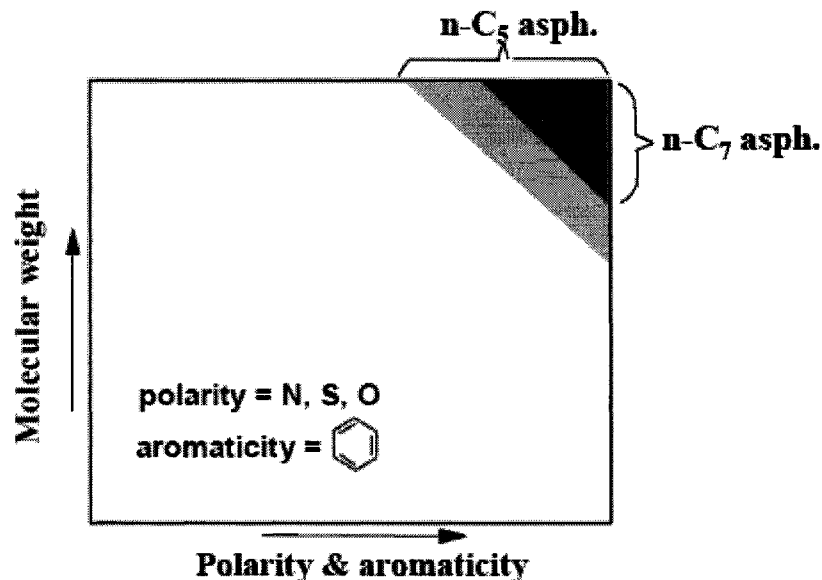


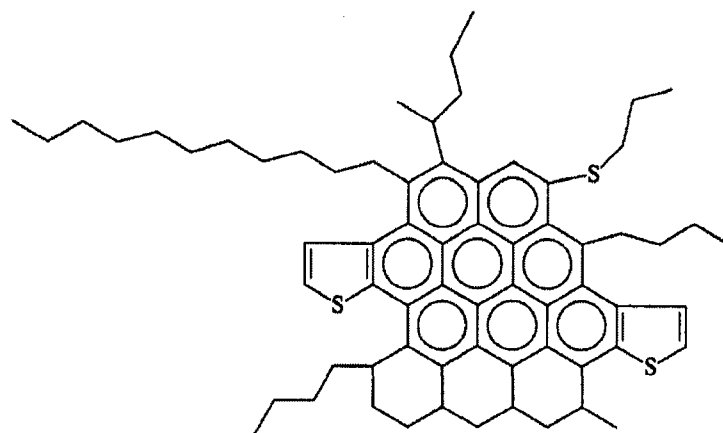
Figure 2.3: “Long diagram” shows that the asphaltenes include the crude oil material highest in molecular weight, polarity, and/or aromaticity molecular weight, polarity, and/or aromaticity²⁶

Although having a wide distribution in molar size and molecular type, asphaltenes are high in one or more of the following properties: apparent molecular weight, polarity, or aromaticity, as illustrated schematically in Fig.2.3²⁶, and high heavy metal and heteroatom contents, which results in a high coking tendency^{27, 28}.

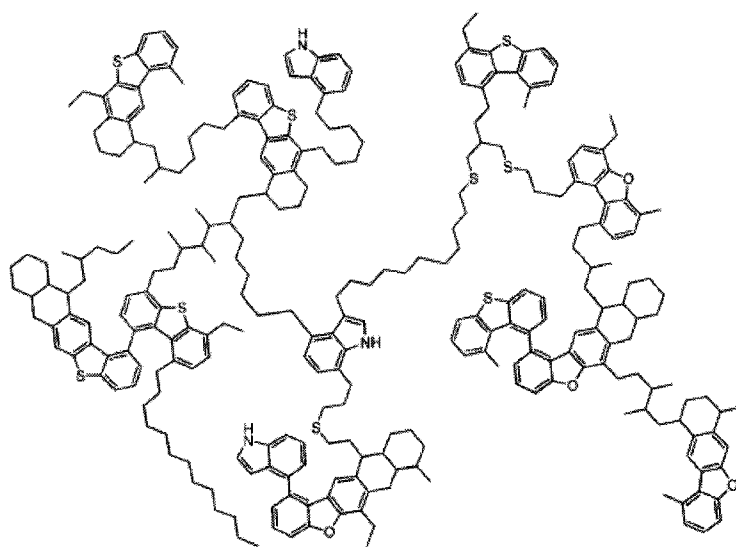
2.2.2 Molecular Structure of Asphaltenes

Asphaltenes comprise numerous species. The average molecular structure and molecular architecture continue to be debated. One frequently finds divergent structures for asphaltenes from the same parent hydrocarbon resource. For example, pericondensed and

archipelago molecular structures have both been proposed for Athabasca bitumen asphaltenes,²⁹ as shown in Figure 2.4. A consensus has yet to be reached on this topic but the field is an active one^{25, 26, 30-36}. The average molecule structures proposed appear to relate to the relative importance that researchers place on different analytical techniques. Irrespective of their global molecular structure, asphaltenes possess molecular fragments such as polynuclear aromatic rings and porphine groups that may facilitate aggregation and interaction with surfaces.



(a)



(b)

Figure 2.4: Average structure of Athabasca asphaltene molecules.
 a) pericondensed model³³; b) archipelago Model³⁶

2.2.3 Asphaltene Precipitation

2.2.3.1 Schematic of Asphaltene Aggregation

Supramolecular behavior and properties of asphaltenes are also debated. That asphaltenes form large structures even in bitumen is accepted and clear²³. A detailed evaluation of the divergent but prevalent views on this topic is beyond the scope of this work. Again the field is an active one and various types of nanoparticles, aggregates, and micelles have been proposed based on disparate physics^{28, 37-43}. The mechanism(s) of asphaltene aggregation and the nature of the resulting structures both remain open questions in the literature.

2.2.3.2 Reversibility of Asphaltene Precipitation

The reversibility of asphaltene precipitation has been a subject of investigation for some time. Leontaritis⁴⁴ and Mansoori⁴¹ treated asphaltene precipitation as an irreversible process. Andersen⁴⁵ demonstrated that asphaltenes partially redissolve with temperature variation. Ramos⁴⁶ verified that the asphaltene precipitation and redissolution processes are reversible when ultrasound was used for mixing. Kokal⁴⁷ observed reversibility of asphaltene precipitation with changes of pressure or composition. Buckley⁴⁸ presented experimental data that support complete reversibility of asphaltene precipitation. Hammami⁴⁹ found that asphaltene precipitation was partially reversible, with changes in pressure. They attributed apparent partial reversibility to slow dissolution kinetics. There is clear support for partial or complete reversibility of asphaltene precipitation. If these

precipitates deposit on local surfaces, asphaltenes or asphaltene rich deposits are a possible source for the reversibly sorbed sticky deposits that are the starting point for this research.

2.2.3.3 The Phase State of the Precipitated Phase

It is now widely acknowledged that precipitated asphaltenes are solids at room temperature. Chung⁵⁰ found the precipitate to be solid when a crude was mixed with n-pentane. Kokal⁴⁷ observed that the precipitated phase is in the form of dark solid particles when a crude is mixed with propane at room temperature and at elevated pressure. At high temperatures, both Kokal⁴⁷ and Hirschberg⁵¹ observed the precipitation of a black liquid. Storm²⁸ observed a transition temperature from solid to liquid at about 300 K. Zou¹⁹ also observed a transition temperature of precipitate asphaltene from solid to liquid when he was doing experiments regarding phase behaviour of ABVB + pentane mixture. He also found that the transition temperature varies with the ABVB mass fraction. It is clear that asphaltene precipitates can be treated as solids at least at room temperature, and as liquids at higher temperatures.

2.3 Naphthenic Acid Corrosion and Deposition

2.3.1 What is Naphthenic Acid?

Naphthenic acids, originally identified as carboxylic acids in crude oils with single or multiple saturated rings, is a term loosely used to include all acidic components in crude oils that may even contain aromatic functionality⁵². The presence of naphthenic acids in the crude oil is a significant concern to the oil sands industry because of their potential to cause corrosion^{53, 54}. There are 1-2 wt % naphthenic acids in Athabasca bitumen⁵⁵. Naphthenic acids may also form metal naphthenates in crude oil processing. From an operational point of view, deposition of metal naphthenates in processing facilities is one of the most challenging issues related to the production of acidic crude oils⁵⁶. Naphthenic acid corrosion, especially in the high temperature parts of the distillation units, is a major concern^{54, 57}. During production, naphthenic acids may also accumulate at interfaces and stabilize emulsions⁵⁸⁻⁶⁰, causing enhanced separation problems. Moreover, the characterization of naphthenic acids is also of interest to geochemical studies, and to refinery wastewater treatment related to environmental compliance. It is for these reasons that naphthenic acid and metal naphthenates were selected as model compounds in this study.

2.3.2 Characterization of Naphthenic Acid

Naphthenic acids are defined as carboxylic monoacids with the generic formula $R(CH_2)_nCOOH$ where R is a cyclopentane ring and n is typically greater than 12, as shown in Figure 2.5.

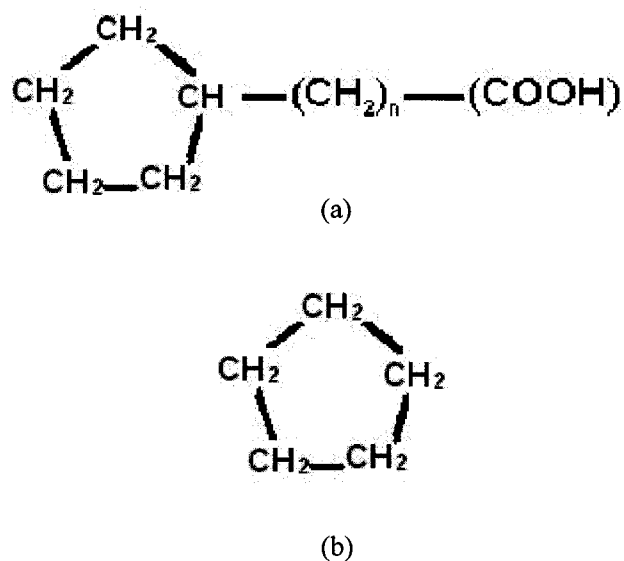
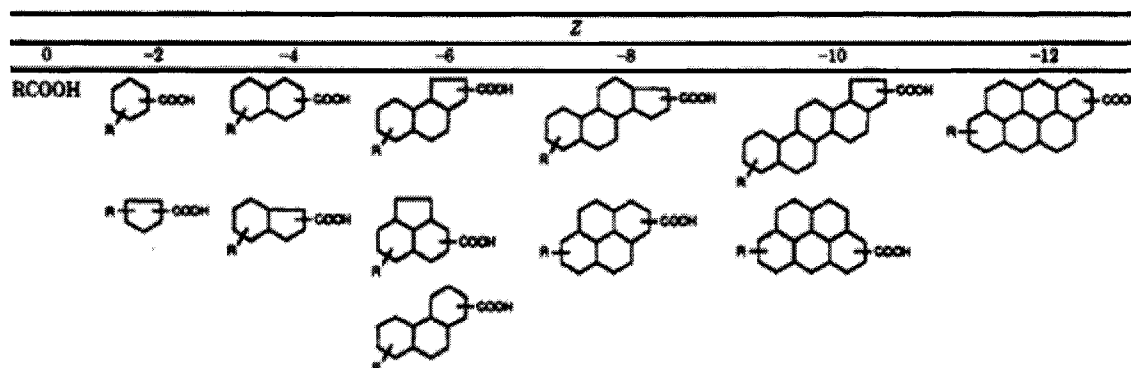


Figure 2.5: (a) General naphthenic acid; (b) Cyclopentane

However, the term “naphthenic acid” is used to describe all carboxylic acids present in crude oils, including aromatic and acyclic acids. This class of material is, like most petroleum fractions, a complex mixture.

Several analytical techniques have been utilized to qualitatively characterize naphthenic acids extracted from crude oils, including various mass spectrometry (MS) methods^{52, 61-64}, gas chromatography-mass spectrometry (GC-MS) methods^{65, 66}, and these methods in combination with Fourier transform infrared (FT-IR) and/or nuclear magnetic resonance (NMR) spectroscopy⁶⁷⁻⁶⁹. Fan⁶² developed an innovative mass spectrometric method employing negative ion fast atom bombardment mass spectrometry (FABMS) for analyzing naphthenic acids. FABMS is well-known for its ability to analyze polar,

Table 2.1: Major naphthenic acid types⁶¹



Isomers within a given z homologue can not be differentiated.

nonvolatile, and/or high molecular weight components and is now a well established technique. Naphthenic acid homologues can be represented by a general formula $C_nH_{2n+z}O_2$, where n indicates the carbon number and z specifies a homologous series. For example, z is equal to 0 for saturated aliphatic carboxylic acids. Table 2.1 lists the major types of naphthenic acids classified by their z numbers from 0 to -12. Acids that are highly aromatic, such as z = -14, -16, -18, etc., are not included. They are considered minor components of the naphthenic acids found in crude oils⁶⁷. Naphthenic acids in crude oils can be described mainly as C10–C50 compounds with 0–6 fused rings, most of which are saturated, where the carboxylic acid group is attached to a ring through a short side chain⁷⁰.

Naphthenic acids with similar molecular weight and total acid number (TAN) can have remarkably different molecular structures⁷¹. Their ability to stabilize emulsions increases with the complexity of mixtures. Turnbull⁷² has shown that the size and structure of

naphthenic acids also influences their corrosivity. Yepez⁷³ et al. monitored the amount of iron dissolved in oil through the formation of the iron naphthenate and found that the amount of dissolved iron so measured underestimates the corrosion rate at temperatures over the thermal decomposition of the iron naphthenate.

2.3.3 Metal Naphthenate Deposition

Although naphthenic acids are known for their corrosivity, the most serious issue related to naphthenic acids is probably deposition of metal naphthenates.⁷⁴⁻⁷⁶ The result of naphthenate deposition in an oil–water separator is shown in Figure 2.6⁷⁷.

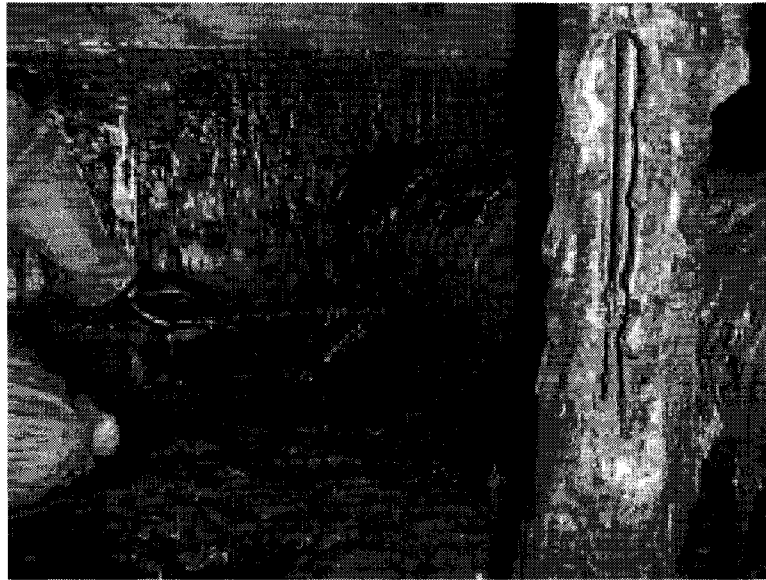


Figure 2.6: Naphthenate deposits in crude oil processing equipment⁷⁷

The problem arises from the release in pressure during fluid transportation from the reservoir to the topside leading to an increase in the pH of the co-produced water, causing a higher degree of dissociation of naphthenic acids at the oil-water (o/w) interface. As a consequence, they become reactive towards metal cations in the water phase. The product from this reaction, metal naphthenate, might then accumulate and start to agglomerate in the oil phase, normally in combination with inorganic materials like clay and scale, and further adhere to process unit surfaces⁷⁸. Deposition of naphthenate is a problem predominantly in topside facilities like o/w separators and may from an operational point of view lead to worst case scenarios in production irregularities accompanied by expensive production shutdowns. Metal naphthenate deposition is becoming a common problem in a number of fields where acidic crudes are being processed, including fields in West Africa^{74, 79} and on the Norwegian continental shelf⁷⁵.

In order to fight naphthenate deposition, chemical mixtures of various compositions are injected into the well stream. This includes surfactant mixtures consisting of ethoxylates and alcohol, which have been shown to reduce deposition significantly⁸⁰. Although the mechanism behind naphthenate inhibition using surfactants is not clarified in detail, it is likely due to a competitive process that takes place at the interface. Some alkoxyates are highly interfacially active and may have a much higher affinity towards the o/w interface than the naphthenic acids. Consequently, they may dilute the interface and bring about longer lateral distances between the dissociated acid monomers⁵⁶. Hence, the naphthenic

acids have to restructure in the interfacial layer in order to complete the reaction, which in turn slows down the reaction rate⁸¹. Metal naphthenate deposition is associated with oil water mixtures. It is unclear if deposition from organic media on acidic, neutral and basic surfaces is significant.

2.4 Surfaces

A surface is defined as the outer boundary of an artifact or a material layer constituting or resembling such a boundary⁸². In this project, surfaces are categorized into acidic, basic and neutral depending on the properties of their outer layers. Chemical compounds, when dissolved in water, give a solution with a hydrogen ion activity differing from that of pure water, i.e. a pH less than 7.0 indicates an acid; a pH greater than 7.0 indicates a base; with a compound yielding a pH of 7.0 is neutral. Surface acidity and basicity is defined analogously most commonly as Lewis acids/Lewis bases.

According to the definition developed by Gilbert Lewis⁸³, an acid is an electron-pair acceptor and a base is an electron-pair donor. Lewis acids and bases include substances with no transferable protons, and thus this definition has a wider application than the Bronsted-lowry definition. The Lewis definition can also be related to molecular orbital theory. In general, an acid can receive an electron pair in its lowest unoccupied orbital

(LUMO) from the highest occupied orbital (HOMO) of a base. That is, the HOMO from the base and the LUMO from the acid combine to a bonding molecular orbital.

On this basis, iron sulfide and silica surfaces are acidic since they can accept electron-pairs. Iron oxide is a basic surface since it can donate electron-pairs when placed in water. Nickel is a neutral surface since it neither accepts nor donates electron-pairs.

2.5 Surface Sorption

2.5.1 Definitions

Sorption refers to either absorption or adsorption⁸⁴. Examples include gases or liquids being incorporated into a material of a different state. Adsorption refers to adhesion to molecules at the interface and can arise from physical or chemical processes - physisorption or chemisorption⁸⁵. Physisorption is a type of adsorption in which the adsorbate adheres to the surface through Van der Waals interactions. It is characterized by low temperature, low enthalpy and low activation energy. Chemisorption is a type of adsorption whereby a molecule adheres to a surface through chemical bonds. As expected, it is characterized by high temperature, high enthalpy and high activation energy.

Both asphaltene adsorption and absorption have been observed by different researchers⁸⁶⁻

⁹⁰. However, due to the complexity of asphaltene structures, the studies of their adsorption and absorption behaviours remain limited and controversial.

2.5.2 Organic Molecule Sorption on to Metal Surfaces

Numerous experimental and theoretical studies have been reported investigating the adsorption and reaction of organonitrogen compounds, specifically pyridine and pyrrole, on different metal surfaces⁹¹⁻⁹⁶. Such functionalities are also expected to be present in asphaltenes. Abdallah and Nelson⁹⁵ studied the adsorption of pyridine (C₅H₅N) on clean and carbon/nitrogen-modified Mo(110) surfaces using temperature-programmed desorption (TPD) and density-functional theory (DFT) calculations. TPD analysis showed that pyridine adsorbs and decomposes on Mo(110) and C/N–Mo(110) at temperatures less than 530 K. Molecular pyridine desorption on clean Mo(110) occurs at temperatures of 375 ± 5 K ($E_{\text{ads}} = 23.5 \pm 0.3$ kcal/mol) and 530 ± 5 K ($E_{\text{ads}} = 33.6 \pm 0.3$ kcal/mol). At higher exposures, a multilayer physisorption peak was also observed at 260 K ($E_{\text{ads}} = 10.4 \pm 0.3$ kcal/mol). Different bonding configurations have been suggested and summarized in Figure 2.7⁹³. The DFT calculations suggest that pyridine initially adsorbs as η^6 -Py-0° coordination followed by η^1 (N)-Py-90° adsorption on clean Mo(110), and surface heating is suggested to result in the transformation of a portion of η^6 -Py-0° pyridine to surface α -pyridyl species (μ_2 , η^2 (N,C2)-Pyridyl, η^2 (N,C2)-Pyridyl) that further decompose to surface carbon and nitrogen and desorbing dihydrogen on clean Mo(110).

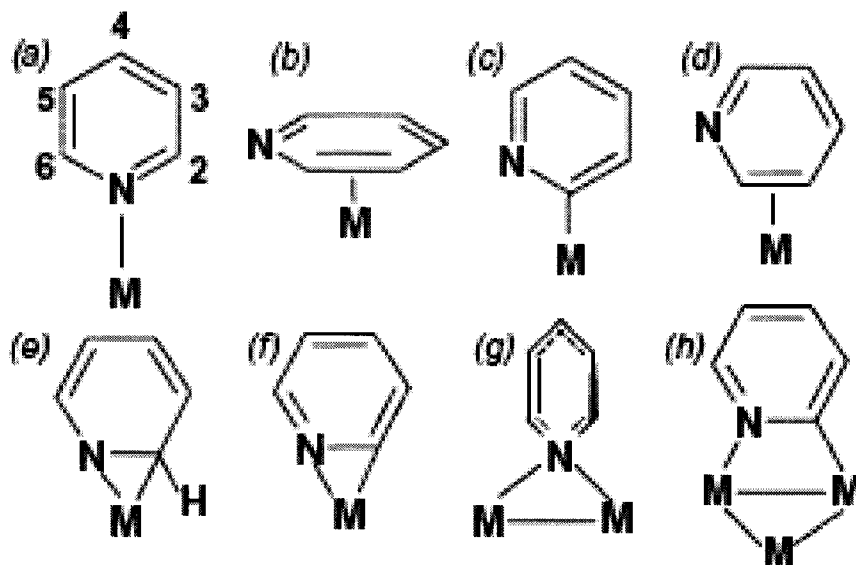


Figure 2.7: Summary of pyridine bonding modes: (a) $\eta^1(\text{N})\text{-Py-}90^\circ$; (b) $\eta^6\text{-Py-}0^\circ$; (c) $\eta^1(\text{C}2)\text{-Py-}90^\circ$; (d) $\eta^2(\text{C}2,\text{C}3)\text{-Py-}90^\circ$; (e) $\eta^2(\text{N},\text{C}2)\text{-Py-}90^\circ$; (f) $\eta^2(\text{N},\text{C}2)\text{-pyridyl}$; (g) $\mu_2, \eta^1(\text{N})\text{-Py-}90^\circ$; (h) $\mu_2, \eta^2(\text{N},\text{C}2)\text{-Py-}90^\circ$.

In another study, Abdallah and Nelson⁹⁶ also investigated the possible adsorption configurations of pyrrole on a Mo(110) surface based on the DFT calculations. The authors suggest that pyrrole adsorbs in a parallel mode with respect to the Mo(110) surface through its π -orbital as $\mu_3, \eta^5\text{-Pyr-}0^\circ$ or $\mu_3, \eta^4(\text{N},\text{C}2,\text{C}4,\text{C}5)\text{-Pyr-}0^\circ$ with an adsorption energy of -28.7 to -31.5 kcal/mol. As the surface exposure increases, lateral interactions between pyrrole molecules during adsorption are suggested to cause competitive adsorption resulting in the coexistence of slightly tilted pyrrole molecules bonding to the surface along with parallel adsorption configurations. This slightly tilted

configuration can be assigned to a $\mu_3, \eta^4(N,C2,C3,C4)$ -Pyr-5° bonding mode with an adsorption energy of -29.9 kcal/mol. Both adsorption geometries bond to three surface Mo atoms, and Mo(110) did not promote hydrogen abstraction.

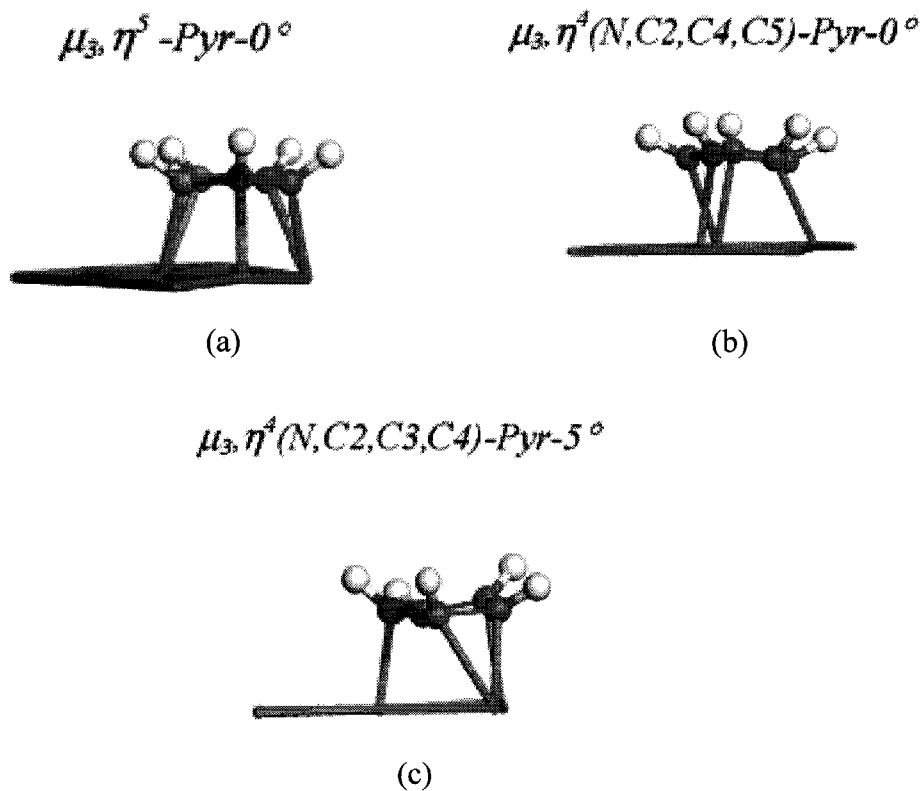


Figure 2.8: Adsorption configurations of pyrrole on Mo(110): (a) μ_3, η^5 -Pyr-0°; (b) $\mu_3, \eta^4(N,C2,C4,C5)$ -Pyr-0°; (c) $\mu_3, \eta^4(N,C2,C3,C4)$ -Pyr-5°.

2.6 Literature Review Summary

From the forgoing discussion, it is clear that the sticky and adherent deposits observed in

the background study for the current work may arise from asphaltene or asphaltene rich deposits because asphaltene precipitation is at least partially reversible and asphaltenes undergo a phase transition to a liquid in a relevant temperature interval. It is readily envisaged that a sticky deposit could form. Naphthenic acid and metal naphthenate chemistry is complex, but it would appear that these materials may also be a possible source of deposits. All of these materials are certainly present in bitumen. Control experiments with model compounds, comprising representative molecular fragments from asphaltene molecules might also prove revelatory. Definition of surfaces used in this project is also discussed. Sorption configuration of organic molecular on metal surface is covered as well.

Chapter 3 Experimental

3.1 Introduction

This chapter describes the materials used, surface construction and surface contamination issues, control experiments, development of deposition experimental approach and procedure and error analysis. Experimental materials are summarized and tabulated in section 3.2. Surface construction by sputtering is briefly explained in section 3.3. Control experiments are discussed in section 3.4. Surface impurity and analysis is presented in section 3.5. All the experiments performed and detailed experimental procedures are described in section 3.6. The XPS technique and properties of deposits measured is elaborated in section 3.7. Error analysis is discussed in section 3.8.

3.2 Materials

In this work, Athabasca Bitumen Vacuum Bottom, a 525 °C+ boiling fraction of Athabasca Bitumen, was previously supplied by CANMET. A detailed composition analysis and physical properties of ABVB is listed in Table 3.1⁴. Other solvents and chemicals used, their grade, purity and suppliers are summarized in Table 3.2. The physical and chemical properties of pentane solutions are also specified in Table 3.3.

Silicon Valley Microelectronics provided the silicon wafers (100 mm in diameter; 525 μm in thickness) that were pre-polished on one face and etched on the other face were provided . A single piece of silicon wafer is shown in Figure 3.1. Sputtering targets used in this work were obtained from Kurt J. Lesker, and are listed in Table 3.4.

Table 3. 1: Composition of ABVB

Elemental analysis (wt. %)	
Carbon	81.66
Hydrogen	9.54
Nitrogen	0.65
Sulfur	6.87
SARA analysis (wt. %)	
Saturates	6.80
Aromatics	41.99
Resins	19.04
Asphaltenes	32.18
Metal analysis (mg/kg)	
Tin	0.7
Lead	1
Copper	1
Aluminum	734
Silicon	898
Iron	322
Chromium	3
Silver	<0.1
Zinc	5
Magnesium	44
Nickel	137
Barium	4
Sodium	48
Calcium	65
Vanadium	344
Phosphorus	8
Molybdenum	17
Boron	3
Manganese	11
Titanium	70

Table 3.2: Chemicals used, their purities and suppliers

Chemicals	Grade Purity	Suppliers
Hydrogen	Research, 99.999 %	Praxair
Nitrogen	Research, 99.998 %	Praxair
Carbon Disulfide	Research, 99.8 + %	Aldrich
Pyrene	Research, 98%	Lancaster
Naphthenic Acid	Technical, 90%	Aldrich
Zinc Naphthenate	Technical, 46%	Aldrich
Pentane	Research, 99%	Fisher Scientific
Tetrahydrofuran	Research, 99.9 + %	Aldrich
Nickel TPP	Research, 99.9%	Aldrich
Zinc TPP	Research, 99.9%	Aldrich

Table 3.3: Physical and chemical properties of pentane

Chemical Formation	C ₅ H ₁₂
Molecular Weight	72.15g/mol
Appearance	Colorless liquid
CAS-Number	[109-66-0]
Density and Phase	0.626g/cm ³ (L)
	0.000378g/cm ³ (V, T=257K)
Melting Point	-129.8 °C (143 K)
Boiling Point	36.1 °C (308 K)

Table 3.4: Sputtering targets

	Iron Oxide	Nickel
Chemical Formation	Fe ₂ O ₃	Ni
Diameter	2.0"	2.0"
Thickness	0.125"	0.125"
Purity	99.9%	99.9%

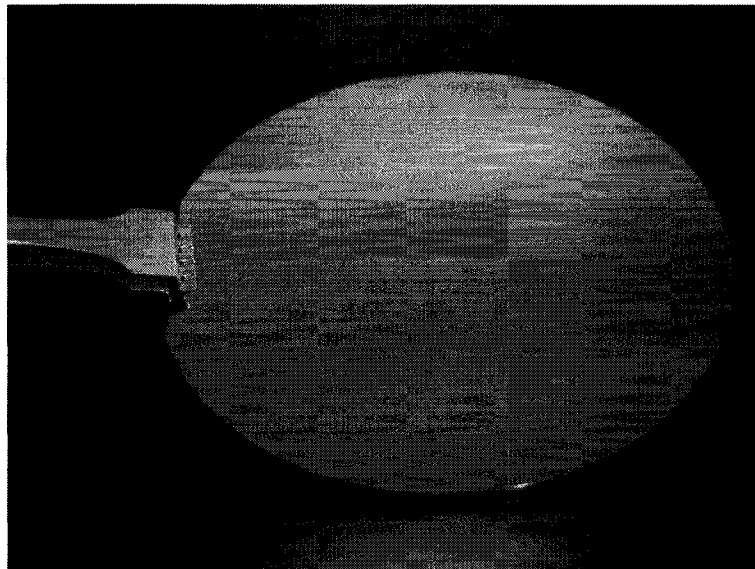


Figure 3.1: Silicon wafer

3.3 Surface Construction

3.3.1 Removal of the Surface Oxidation Layer from Silicon Wafers

Under exposure to oxygen, a silicon surface will naturally oxidize to form a thin silicon dioxide (SiO₂) layer⁹⁷. Oxidation takes place in two different ways due to oxygen or water vapor, respectively. One is called “dry oxidation”, equation 3.1. The other one is called “wet oxidation”, equation 3.2.



Because of the stoichiometric relationships in the above two reactions and the difference between the densities of Si and SiO₂, about 46% of the silicon surface is consumed as illustrated in Figure 3.2.

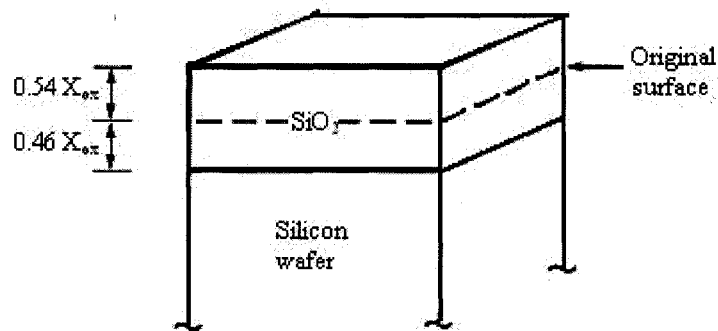


Figure 3.2: Oxidation of silicon wafer surface

The first step in surface construction is the removal of the oxidation layer as well as any other organic contaminations on the wafers before sputtering is carried out. This is conducted at the University of Alberta NanoFab by using piranha solution. Piranha solution is a mixture of sulfuric acid (H_2SO_4) and hydrogen peroxide (H_2O_2). It is frequently used in the microelectronics industry to clean organic residues from substrates. Many different mixture ratios are commonly used, and all are called piranha solution. A typical ratio is 3:1 with concentrated sulfuric acid to 30% hydrogen peroxide solution. The cleaning work is performed according to the following steps:

1. Place substrates to be cleaned in a Teflon carrier.
2. Label the beaker for piranha, i.e., name of solution, user name and date.
3. Determine the volume needed to completely immerse the substrates.
4. Calculate the amounts of sulfuric acid and hydrogen peroxide required for the

determined volume. For example, to prepare 800 ml piranha, 600 ml sulfuric acid and 200 ml hydrogen peroxide are needed, respectively.

5. Select two beakers and mark the volume of each chemical that needed on the outside of the beakers
6. Put on all the safety gear and get the chemicals from the cabinets
7. Slowly pour the calculated amount of sulfuric acid into selected beaker. Pour this amount to a large beaker labeled piranha. Place the empty beaker into the dump rinser.
8. Slowly pour the calculated amount of hydrogen peroxide to the other selected beaker. Pour this amount into large beaker labeled piranha, which already contains sulfuric acid. Place the empty beaker into the dump rinser beside first beaker, and start rinsing cycle.
9. Carefully place the Teflon carrier with substrates into the piranha. There may be vigorous reaction with gas release and liquid entrainment.
10. Start timing for 15 min.
11. Wash the chemical bottle on the outside and dry using wipes. Place the bottles back into the storage cabinets.
12. When the time is up, slowly remove the carrier from the solution allowing excess to drip back into the beaker.
13. Transfer the substrates cautiously into the dump rinser and start rinsing for full 5 cycles.

14. Dry the substrates by nitrogen gas.

Piranha solution can be explosive. Mixing the solution is exothermic. The resultant heat can bring solution temperatures up to 120 °C. When handling piranha solution, one must be sufficiently equipped and protected⁹⁸.

- The solution should be prepared and kept at all times inside a fume hood.
- The user must be wearing safe lab attire while working with piranha solution
 - A full face shield
 - Rubber gloves
 - Lab coat
 - Acid apron
 - Long pants
 - Closed-toe shoes
- Always use glass containers when dealing with solution. Piranha solution will melt and react with plastics.

3.3.2 Iron Oxide, Nickel Surface Formation (Sputtering)

Surface construction was conducted on cleaned surface using sputtering deposition. Sputtering deposition is a physical vapor deposition (PVD) method of depositing thin films by sputtering source material onto a substrate^{99,100}. Sputtered atoms ejected into the gas phase are not in their thermodynamic equilibrium state, and tend to deposit on all surfaces in the vacuum chamber. A substrate (such as a wafer) placed in the chamber is coated with a thin film. Sputtering usually uses argon plasma. A schematic diagram of sputtering process is shown in Figure 3.3.

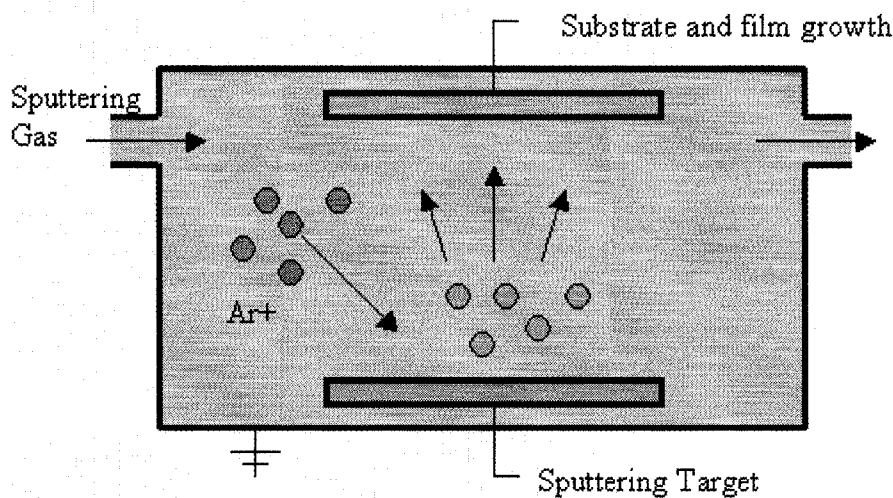


Figure 3.3: Schematic diagram of sputtering process

In this work, a sputtering system (ATC ORION 5 UHV, AJA International, Inc.) was used for deposition. A picture of the sputtering system is shown in Figure 3.4. Since the ultimate goal of the project is to investigate the influence of surface properties on

asphaltene deposition from organic material from hydrocarbon + pentane mixtures, sputtering targets with different surface acidity/ basicity were chosen. Iron oxide (basic) and nickel (neutral) were selected as thin film materials. The silica itself is acidic. Iron sulfide surfaces were formed by sulfidizing iron oxide surfaces. Substrates for deposition experiments were taken from one of three wafers: a wafer with a nickel film with thickness of 100 nm, and from one of two wafers with films of iron oxide with thickness of 40 nm and 137 nm. In the case of nickel, a direct current (DC) gun was chosen for sputtering; while in the case of iron oxide, a radio frequency (RF) gun is used for sputtering as an insulating target can not be sputtered by a DC gun. Sputtering parameters are provided in Table 3.5.

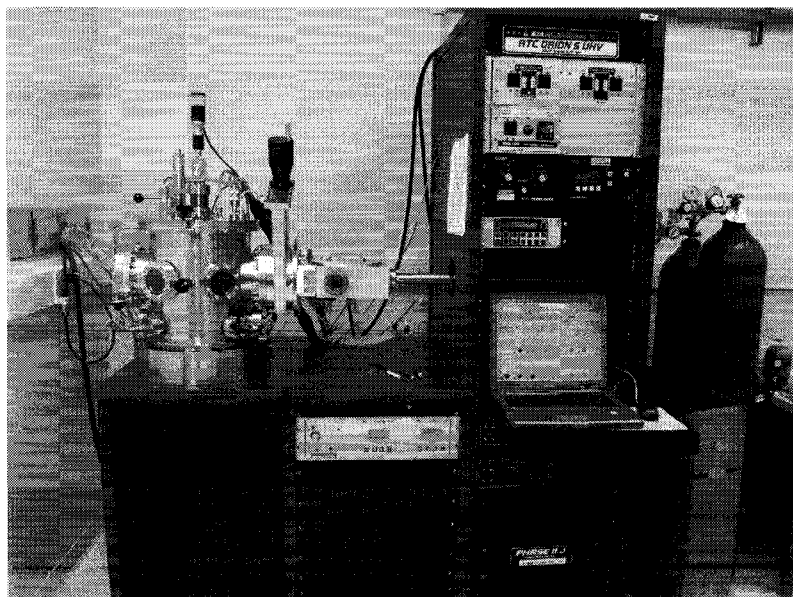


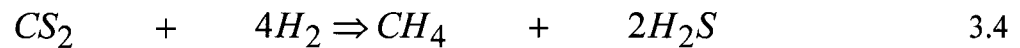
Figure 3.4: ATC ORION 5 UHV Sputtering system

Table 3.5: Sputtering parameters

Thin Film	Ni	Iron Oxide
Sputtering techniques	DC Sputtering	RF Sputtering
Argon Pressure	4 mTorr	4 mTorr
Argon Flow Rate	10 SCCM	10 SCCM
Sputter Power	150 watt	49 watt
Shutter Delay	120 s	3300 s

3.3.3 Iron Sulfide Surface Formation (Sulfidation of Iron Sulfide Surface)

The iron sulfide surface was obtained by sulfidation of iron oxide surface. The process is governed by the following equations.



Based on a 1 cm x 2 cm iron oxide film with thickness of 137 nm, we have

$$A = 2 \text{ cm}^2 \quad t = 137 \text{ nm} = 1.37 \times 10^{-5} \text{ cm} \quad V = 2.74 \times 10^{-5} \text{ cm}^3$$

$$\rho = 5.24 \text{ g/cm}^3 \quad m = V \times \rho = 1.44 \times 10^{-4} \text{ g} \quad M = 159.69 \text{ g/mol}$$

$$\text{Molar} = \frac{m}{M} = 9.01 \times 10^{-7} \text{ mol}$$

The minimum amount of CS₂ and H₂ needed are 0.054 μL and 0.743 Pa, respectively. During surfidization, the amount of CS₂ and H₂ used was 15 μL and 101325 Pa. This ensures that the surface is completely sulfidized. During sulfidation, a batch reactor with a volume of 15 L was employed to contain the iron oxide film, CS₂ and H₂. The reactor was then put into a sand bath for 2 hours and 30 minutes at a temperature of 250 C.

3.4 Surface Compositions

The initial surface composition is of critical importance in this work. Surface composition and surface contamination are key issues. For example, Table 3.6 indicates the composition of the iron oxide surface (40 nm thickness) based on XPS analysis.

Table 3.6: Iron oxide surface characterization

	Mass %
Fe	57.41 +/- 3.38
O	27.53 +/- 2.05
N	0.23 +/- 0.12
C	11.79 +/- 1.36
S	0.71 +/- 0.64

There is nitrogen, carbon and sulfide contamination on the surface. Oxygen contamination from constituents in the air, i.e. O₂, CO₂ and H₂O, is also anticipated. All

of the prepared surfaces are contaminated to some degree and this issue is addressed in detail in Chapter 4.

3.5 Control Experiments

To better understand the organic material deposition material, control experiments were performed with model compounds. Both negative control experiments and positive control experiments were performed with acidic (silica) and basic (iron oxide) surfaces.

3.5.1 Negative Controls

Pentane is not expected to sorb significantly on any of the surfaces. For this case, a wafer substrate was exposed to liquid pentane in a batch reactor and heated to 125 C for 3 hours and 30 minutes. The substrate was then immersed in pentane solution at room temperature for 30 minutes before being subjected to XPS analysis. The same experiment was performed for pentane + pyrene mixture with a pyrene mass fraction of 2.52% (solubility limit for pyrene in pentane at 125 C).

3.5.2 Positive Controls

Naphthenic acid and metal naphthenate, which are both contained in bitumen, are expected to deposit as noted in Chapter 2.3, as are porphine compounds. Experiments

were performed with naphthenic acid alone and with naphthenic acid + pentane, and zinc naphthenate + pentane mixtures as well as with two different porphines tetraphenylporphine zinc (zinc TPP) and tetraphenylporphine nickel (nickel TPP) + pentane mixtures. For example, a wafer substrate is exposed to naphthenate + pentane solution with a naphthenate mass fraction of 0.15. The mixture is again heated in a batch reactor to 125 C for 3 hours and 30 minutes. Then it is exposed to pentane solution at room temperature for another 30 minutes prior to XPS analysis.

3.6 Bitumen Deposition Experiments

3.6.1 Experimental Surfaces

The primary goal of this project is to explore how the surface properties influence the deposition of heavy oil constituents. Consequently, experiments have to be performed on acidic, basic and neutral films. In this work, iron oxide film is chosen as a basic surface; nickel film is selected as a neutral surface; iron sulfide and silica are acidic surfaces. An idealized model of sample substrate without surface contamination is given in Figure 3.5.

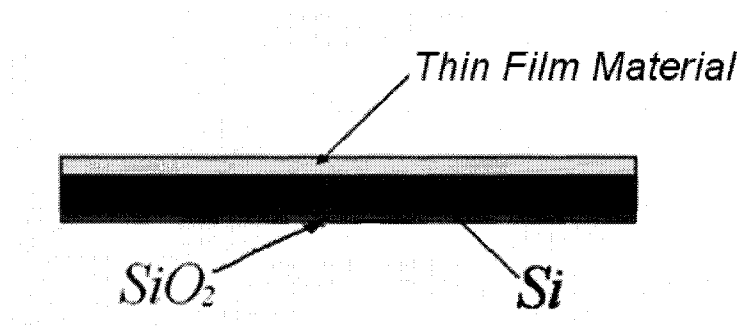


Figure 3.5: An idealized model of the deposition substrate

3.6.2 Experimental Approach and Procedure

The development of an appropriate experimental procedure for organic material deposition on prepared surfaces proved challenging. The final experimental procedure consists of six major steps:

- Prepare ABVB + Pentane mixtures at specific ABVB mass fractions;
- Add one wafer substrate and about 5 grams of individual mixtures to a 15 ml batch reactor;
- Heat the reactor to a temperature above the deposition temperature for a time period T_1 and then quickly cool down by immersion of the batch reactor in water;
- Immerse the wafer in pentane at room temperature for a time period T_2 ;
- Wash the wafer with pentane to remove bulk fluid then dry the wafer;
- Subject the wafer to XPS.

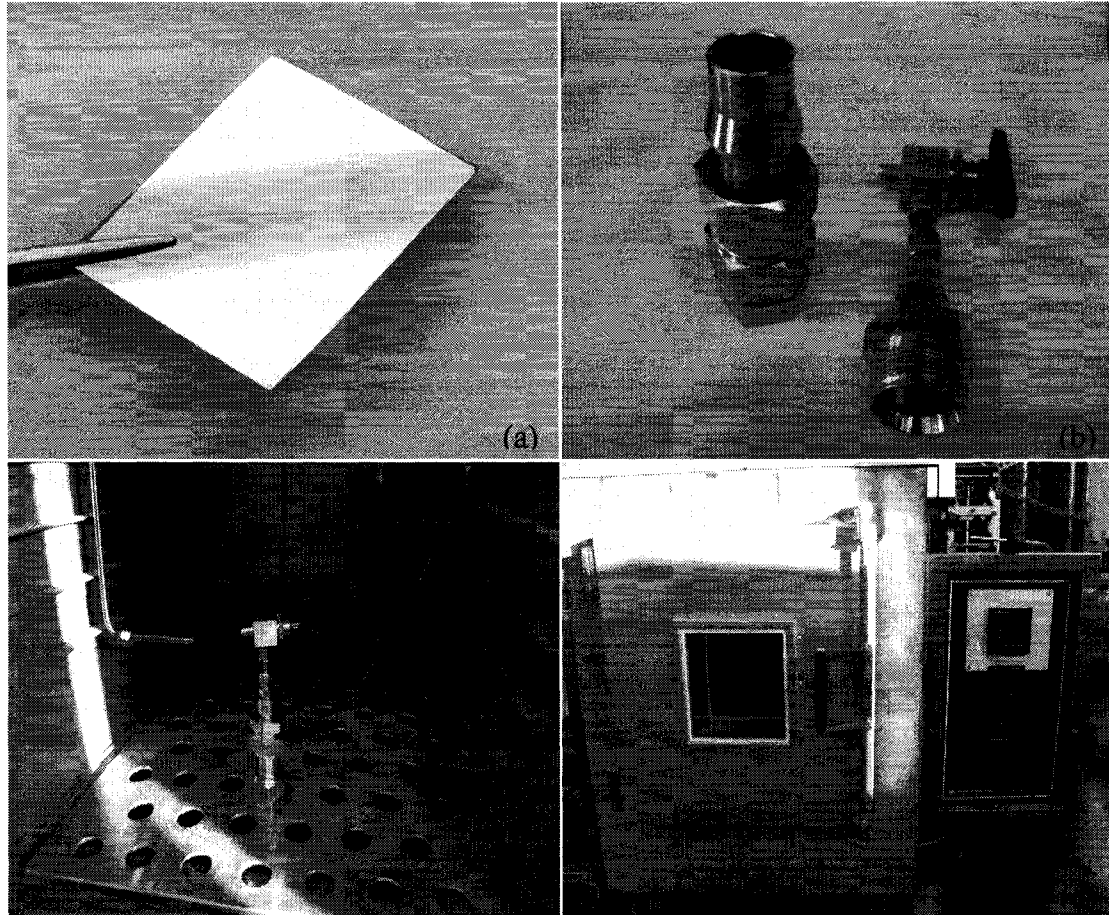


Figure 3.6: Experimental setup (a) wafer sample; (b) batch reactor; (c) reactor in oven detail; (d) Oven

Besides the differences of film composition and thickness, there are three variables in this procedure, i.e. ABVB mass fraction, t_1 and t_2 . ABVB mass fraction is the factor to evaluate if the deposit varies with ABVB content in the mixture or not. t_1 is a measure of how long the deposition takes place and whether the deposit differs with deposition time. The reason to immerse substrate into pentane for a time period of t_2 after deposition is to ensure that the bulk fluid from deposit is removed. Washing the organic deposit at room temperature, once the substrate is removed from the reactor, is a key step as illustrated in

Figure 3.7.

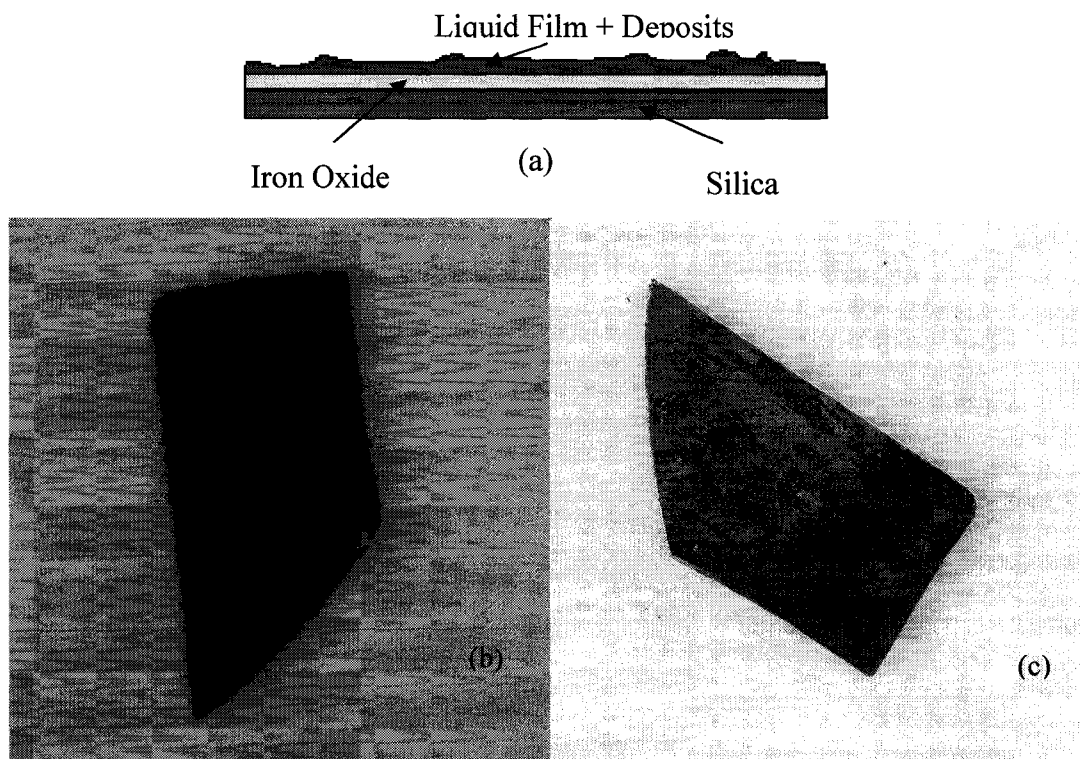


Figure 3.7: (a) Deposition schematic; (b) Image of liquid film + deposit; (c) Image of surface deposit following a pentane wash

3.6.3 Experimental Matrix

Once the experimental procedure was determined, the next step was to establish an experimental matrix. There are many parameters involved in the experimental procedure as discussed in previous section. It is crucial to investigate the impact of each parameter on the ABVB deposition. Parameters include thickness of films, ABVB wt% of mixture,

time in pentane above phase boundary (t_1) and time in pentane below phase boundary (t_2). The whole experimental matrix is completed for the iron oxide surface while the other three surfaces are only evaluated at certain levels. The experimental matrix for evaluation of mixtures of ABVB and pentane on iron oxide, nickel and silica surfaces with fixed ABVB mass fraction is shown in Table 3.7.

Table 3.7: Experimental matrix for evaluation of mixtures of ABVB and pentane on iron oxide, nickel and silica surfaces with fixed ABVB mass fraction

ABVB wt%=15 %	Iron Oxide Surface		Nickel and Silica Surfaces
	40 nm	137 nm	
$t_2=30\text{min}$			$t_1=1\text{hr}$
			$t_1=1\text{hr}30\text{min}$
	$t_1=2\text{hr}$	$t_1=2\text{hr}$	$t_1=2\text{hr}$
	$t_1=2\text{hr}30\text{min}$	$t_1=2\text{hr}30\text{min}$	$t_1=2\text{hr}30\text{min}$
	$t_1=3\text{hr}$	$t_1=3\text{hr}$	$t_1=3\text{hr}$
	$t_1=3\text{hr}30\text{min}$	$t_1=3\text{hr}30\text{min}$	$t_1=3\text{hr}30\text{min}$
	$t_1=4\text{hr}$	$t_1=4\text{hr}$	$t_1=4\text{hr}$
	$t_1=4\text{hr}30\text{min}$	$t_1=4\text{hr}30\text{min}$	$t_1=4\text{hr}30\text{min}$
		$t_1=5\text{hr}$	$t_1=5\text{hr}$
$t_1=3\text{hr}30\text{min}$	$t_2=0\text{min}$	$t_2=0\text{min}$	
	$t_2=30\text{min}$	$t_2=30\text{min}$	
	$t_2=1\text{hr}$	$t_2=1\text{hr}$	
	$t_2=1\text{hr}30\text{min}$	$t_2=1\text{hr}30\text{min}$	
	$t_2=2\text{hr}$	$t_2=2\text{hr}$	
	$t_2=2\text{hr}30\text{min}$	$t_2=2\text{hr}30\text{min}$	

* t_1 : The time that substrate is exposed to mixtures above phase boundary.

* t_2 : The time that substrate is exposed to pentane at room temperature.

Table 3.8: Experimental matrix for evaluation of mixtures of ABVB and pentane on iron oxide, nickel and silica surfaces at different ABVB composition

ABVB wt Fraction	Temperature
$X_1=0.00$	25 C (R.T.)
$X_1=0.05$	170 C
$X_1=0.15$	125 C
$X_1=0.30$	100 C
$X_1=0.45$	60 C
$X_1=0.60$	80 C
$X_1=0.80$	100 C
$X_1=1.00$	140 C
$t_1=3\text{hr}30\text{min}$, $t_2=30\text{min}$, Thickness(Iron Oxide)=137 nm, Thickness(Nickel)=100 nm	

Due to the limited quantity of iron sulfide surfaces obtained, the deposition experiments with the iron sulfide surface is only performed at one condition with a t_1 of 3 hours and 30 minutes, a t_2 of 30 minutes and a mass fraction of ABVB 15 wt%.

3.7 Deposit Property Measurement

3.7.1 X-ray Photoelectron Spectroscopy (XPS)

X-ray Photoelectron Spectroscopy (XPS) is an analysis technique used to obtain chemical information about the surfaces of solid materials¹⁰¹. It has a variety of applications and is able to provide information as follows:

- Elemental composition of the surface (1–10 nm usually)
- Elements that contaminate a surface
- Chemical or electronic state of each element on a surface
- Uniformity of elemental composition across the top of a surface
- The thickness of one or more thin layers (1–8 nm) of different materials within the top 10 nm of the surface

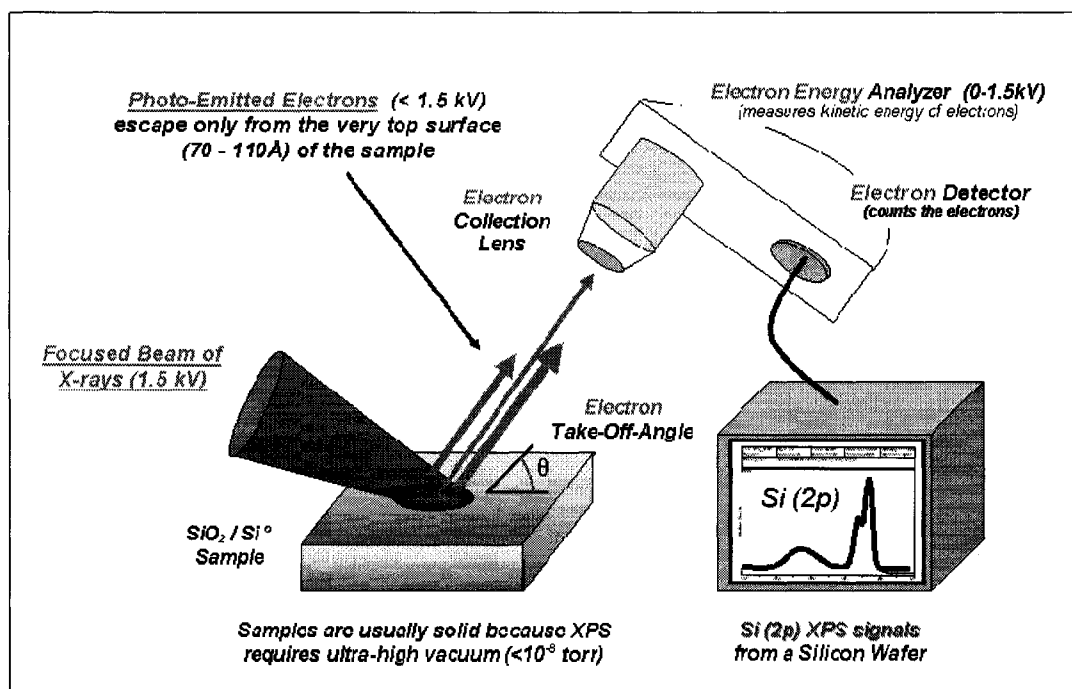


Figure 3.8: Schematic diagram of X-ray photoelectron spectroscopy¹⁰¹

Figure 3.8 shows how XPS works¹⁰¹. High-energized X-ray is used to bombard the surface of target materials and electrons with characteristic of materials are ejected and absorbed by an electron energy analyzer. A typical XPS spectrum could then be plotted based on the information like binding energy, numbers of electrons detected.

XPS is used in this work to obtain deposit thickness, deposit composition and the chemical state of each element. The XPS measurements were performed on AXIS 165 spectrometer (Kratos Analytical) at the ACSES. The base pressure in the analytical chamber was lower than 4×10^{-8} Pa and the working pressure was better than 3×10^{-7} Pa. The resolution function of the instrument for Al-mono source, hybrid lens mode has been determined to be 0.4 eV on the basis of the Co Fermi edge, 0.55 eV for Ag 3d and

0.70 eV for Au 4f peaks. Monochromated Al K α x-rays ($h\nu = 1486.6$ eV) were used at power of 210 W. Fixed analyzer transmission (FAT) mode was applied. The analysis spot was 700 x 400 μm . Charge neutralization was required during the measurements. All survey scans spanned from 1100 to 0 eV binding energy and were collected with analyzer pass energy (PE) of 160 eV with a step of 0.3 eV. For the high-resolution spectra the pass-energy was 20 eV with a step of 0.1 - 0.15 eV.

3.7.2 Thickness of Deposit

3.7.2.1 Inelastic Mean Free Path (IMFP) of Electrons

The IMFP is a measure of the average distance traveled by an electron through a solid before it is inelastically scattered. It is actually defined by the following equation which gives the probability of the electron traveling a distance, d , through the solid without undergoing scattering:

$$P(d) = \exp(-d/\lambda) \quad 3.5$$

where λ is the IMFP for the electrons of energy E .

It is dependent on the following two factors:

- The initial kinetic energy of the electron.
- The nature of the solid. (However, most elements show very similar IMFP versus energy relationships).

The following graph illustrates the functional group of $P(d)$.

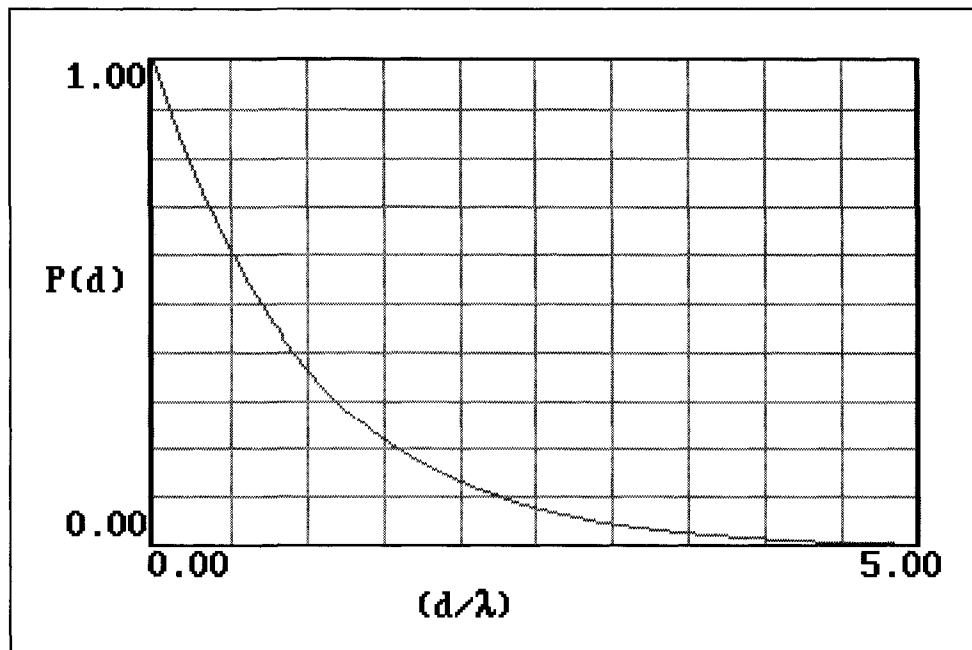


Figure 3.9: Diagram of $P(d)$ function

It is clear that the probability of escape decays very rapidly and is essentially zero for a distance $d/\lambda > 5$. Assume that 100 electrons are collected by detector. The majority of electrons detected come from within one IMPF distance of the surface. Virtually all (>95%) of the electrons detected come from within three IMFPs distance of the surface. This means that any experimental technique such as XPS, which involves the generation and detection of electrons of such energies, will be surface sensitive.

3.7.2.2 Calculation of Deposit Thickness

The knowledge of IMFP can be used to calculate the thickness of surface films. Suppose that a substrate material B is covered by a thin film of a different material A, as illustrated in Figure 3.10. The XPS signal from the underlying substrate will be attenuated (i.e. reduced in intensity) due to inelastic scattering of some of the photoelectrons as they traverse through the layer of material A.

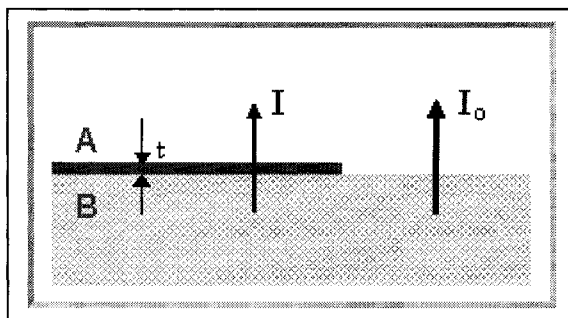


Figure 3.10: Model of film thickness calculation

The probability of such a scattering event for any single photoelectron passing through this layer is simply given by:

$$P = \exp(-t/\lambda) \quad 3.6$$

where t is the thickness of the layer of material A.

It follows that the overall intensity of a XPS signal arising from B is reduced by this same factor, i.e. if the intensity of this signal in the absence of any covering layer is I_0 , then the

intensity I in the presence of the over layer is given by :

$$I = I_0 \exp (- t / \lambda) \quad 3.7$$

$$t = \lambda \log (I_0 / I) \quad 3.8$$

It also follows that it is possible to estimate the thickness of a deposited layer by using the above equation, provided the reduction in the substrate signal is known.

For example, suppose XPS analysis is used to detect the iron oxide surface thickness before an experiment. The intensity of the iron element obtained is called I_0 . XPS is also used to detect the deposit on top of the iron oxide surface after an experiment. The thickness of deposit is so thin that part of the iron electrons from the underlying layer could also be detected. The intensity obtained is called I . Suppose the X-ray utilized is monochromatic Al K α with a kinetic energy of 1486.6 eV. The binding energy of Fe 2p electron is 710.0 eV. So the escaped Fe electron will have a kinetic energy of 776.6 eV. According to Ebel¹⁰² et al. (1990), the λ for Fe electron with a kinetic energy of 776.6 eV is 0.81 nm. Equation 3.8 could then be applied to calculate the thickness of deposit.

3.7.3 Composition of Deposit

3.7.3.1 Elemental Analysis

XPS is able to detect all elements except hydrogen in terms of elemental analysis. It provides composition for elements like, carbon, oxygen, nitrogen and sulfides, which are

the major components of ABVB. It could also tell the composition of other elements that are either from the substrate, i.e. iron and nickel, or from the model compounds, i.e. Zn.

3.7.3.2 Atom bonding

Chemical bonding between different atoms can be obtained from high-resolution spectroscopy. This will give more detailed information related to sputtered deposits and ABVB deposits as well as the surface impurities.

3.7.3.3. C/S ratio

Surfaces are contaminated with a number of elements, i.e. O, N, C and S. Among these elements, sulfur contamination is least. As carbon comprises 80 wt % of organic deposits, the carbon to sulfur is the most stable indicator of the nature of the sorbed species. Table 3.9 shows the composition of ABVB, ABVB asphaltene and ABVB asphaltene free oil. Table 3.10 shows the mass ratio of each element to sulfur element for ABVB, ABVB asphaltene and ABVB asphaltene free oil. The carbon to sulfur ratios in these materials differs significantly but miss attribution of an organic deposit is possible because, surface contamination tends to increase the value of the ratio. Organic contamination can take two forms. It can be present on the inorganic substrate, and remain present throughout experiments, and or it can adhere to top of the organic deposit post experiment.

Table 3.9: Elemental composition of ABVB

Normalized to 100%	O wt%	N wt%	C wt%	S wt%
ABVB	1.5	0.7	90.2	7.6
ABVB asphaltene	1.8	1.1	88.3	8.8
ABVB asphaltene free oil	1.4	0.5	91.1	7.0

Table 3.10: Elemental composition of ABVB relative to sulfur

Mass "i" % / S %	O	N	C	S
ABVB	0.2	0.1	11.9	1.0
ABVB asphaltene	0.2	0.1	10.0	1.0
ABVB asphaltene free oil	0.2	0.1	13.0	1.0

Washing iron oxide substrates at room temperature, or heating the substrate in pentane has an effect on surface contamination as shown in Table 3.11. It is not clear if the contamination noted post blank experiments is adherent throughout or if it is reintroduced during the subsequent analysis step. At this time we assume that it is adherent and process the deposition data accordingly.

Table 3.11: Surface composition of iron oxide film (137 nm)

Weight %	As prepared	Pentane washed	100 ppm Ni porphine in pentane t1= 3hrs 30 minutes, t2 = 30 min
Fe	55.66	55.58	57.48
O	25.57	25.57	24.93
N	0.07	0.08	0.23
C	18.70	18.42	17.36
S	0.00	0.35	0.00

We assume that there are two contamination layers as depicted in Figure 3.11. To obtain the composition of organic deposits, it is imperative to correct for both surface contamination 1 and surface contamination 2.

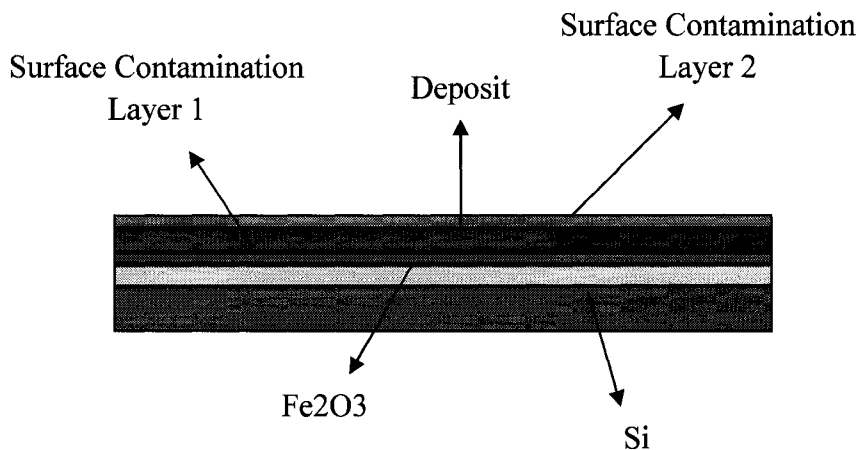


Figure 3.11: Contamination model

The impact of this correction is significant relative to the difference between the carbon

to sulfur ratios of bitumen related constituents. For example, Table 3.12 gives the raw composition data for deposits on an iron oxide surface with 137 nm thickness, where $t_1 = 3.5$ hr, $t_2 = 0.5$ hr, ABVB composition = 15 wt %. The thickness of a deposit is obtained from equation 3.8. Then, equation 3.7 is employed to determine the carbon signal detected by X-ray that is actually from the contamination layer 1. The escape depth of carbon at a kinetic energy of ~ 1200 eV is 1.58 nm. Table 3.13 shows the data corrected for contamination layer 1. C^* represents the correction for layer 1. Then C^* is deducted from raw data of carbon. C_1 stands for the carbon corrected for contamination layer 1. The C/S ratio calculated from the raw data is 12.94 ± 0.62 . Correcting for contamination layer 1 yields a C/S ratio of 11.98 ± 0.39 .

Table 3.12: Raw composition data on the iron oxide surface

Weight %	1	2	3	4
Fe	2.94	11.13	1.48	2.29
O	5.91	13.72	5.75	7.75
N	0.99	0.08	0.83	0.99
C	83.89	69.91	85.03	82.39
S	6.27	5.16	6.91	6.58

Table 3.13: Data corrected for contamination layer 1

	1	2	3	4
Fe wt%	2.94	11.13	1.48	2.29
Thickness (nm)	1.03	0.56	1.27	1.12
C^* (Layer 1) wt%	5.14	9.16	3.81	4.61
C_1 wt%	78.75	60.75	81.22	77.78
C_1/S	12.56	11.77	11.75	11.82

The carbon to sulfur ratio is reduced by almost 1, which equals the difference between the asphaltene free oil and the feed ABVB, and is one-third the difference between asphaltene free oil and asphaltenes. The same mathematics is applied to all the data on iron oxide, nickel and silica surfaces. Correction for contamination layer 2 is more challenging. For example, no correction for hydrocarbon adsorption from air can be made. However, there is little oxygen that is not accounted for, as part of the iron oxide and the sorption of CO and CO₂, both key contaminants on the substrates, are therefore not significant for layer 2. Contamination from layer 2 is therefore not important with respect to the evaluation of C/S ratios. Contamination and contamination variability remain the most significant source of uncertainty in the experimental program. It is for this reason that we have chosen to reproduce experiments and analysis multiple times.

3.8 Error Analysis

3.8.1 Errors from Sample Preparation

Two weighing instruments are used in this work. The analytic balance (Mettler Toledo AG285 Dual Range Balance) is used to obtain the weight of ABVB and model compounds which are normally to the order of magnitude of 100 mg. This balance has a fine range of 85 g with readability 0.01 mg and coarse range of 210 g with readability of

0.1 mg. Hence, the fine range mode is chosen while measuring the weight of bitumen and chemical samples. The error induced is to the order of magnitude of 0.01 mg, which is not significant compared to the sample being weighed. The other balance (Sartorius L 2200 P) is used to measure the weight of solution and the reactor as a whole. The capacity of this balance is 2220 g with readability of 0.01 g. Given the fact that the weight of the solution used is normally larger than 3.0 g and the weight of the reactor is normally larger than 300 g, the error induced here is less than 1%.

3.8.2 Errors from Analysis

Errors could also be induced during XPS analysis procedure. The detection limitation of XPS instrument used in this work is 0.1 atom %. The quantitative accuracy is dependent on many factors:

- **Satellite Error.** The monochromatic X-ray used to bombard the material surface could be a narrow beam of X-ray with different values of energy.
- **Statistical Error (or white noise).** Electron energy analyzer will detect the electrons being emitted to vacuum chamber and then a typical XPS spectrum could be plotted based on information like energy of electrons and number electrons detected. However, the analyzer could make mistakes while counting the number of electron being absorbed by the analyzer.
- **Background Error.** When processing the spectroscopy, different backgrounds will

give different areas and hence end up with different weight percentage of each element.

There are other factors may affect the accuracy of XPS results, i.e. relative sensitivity factor of each element, correction for electron transmission function, etc.. To be on the safe side, the error of element composition from XPS analysis is considered to be below 10%.

Chapter 4 Results and Discussion

4.1 Introduction

This chapter is divided into three sections. Section 4.2 concerns substrate composition and contamination issues. Chapter 4.3 concerns deposition experimental results with model compounds. Chapter 4.4 concerns results from deposition of Athabasca bitumen vacuum residue. The thickness and composition of deposits is elaborated in depth.

4.2 Surface Composition and Contamination

4.2.1 Contaminated Surface Compositions

As mentioned in Chapter 3.4, surface contamination is an issue in this field. Table 4.1 shows the raw data for the composition of iron oxide, iron sulfide, nickel and silica surfaces.

Table 4.1: Composition of iron oxide, iron sulfide, nickel and silica surfaces (raw data)

	Iron Oxide	Iron Sulfide	Nickel	Silica
Fe	57.41 +/- 3.38	40.16 +/- 7.82	0	0
Ni	0	0	69.24 +/- 1.18	0
Si	0	0	0	64.13 +/- 0.64
O	27.53 +/- 2.05	17.17 +/- 2.11	17.89 +/- 0.32	25.72 +/- 0.55
N	0.23 +/- 0.12	0.38 +/- 0.27	0.06 +/- 0.06	0.42 +/- 0.18
C	11.79 +/- 1.36	24.84 +/- 6.38	12.60 +/- 0.96	9.52 +/- 0.46
S	0.71 +/- 0.64	17.00 +/- 1.34	0.04 +/- 0.11	0.21 +/- 0.51

4.2.2 Composition and Contamination of the Iron Oxide Surface

Figures 4.1 and 4.2 show the high resolution spectroscopy for elemental oxygen and carbon respectively on the iron oxide surface. The oxygen peak can be divided into two sub peaks. The one with binding energy 530.1 eV can be assigned to O-Fe bonding (65.4% of the total oxygen). The sub peak with a higher binding energy of 531.6 eV corresponds to O-C, O-H and O-O bonding, and is mainly due to contamination.

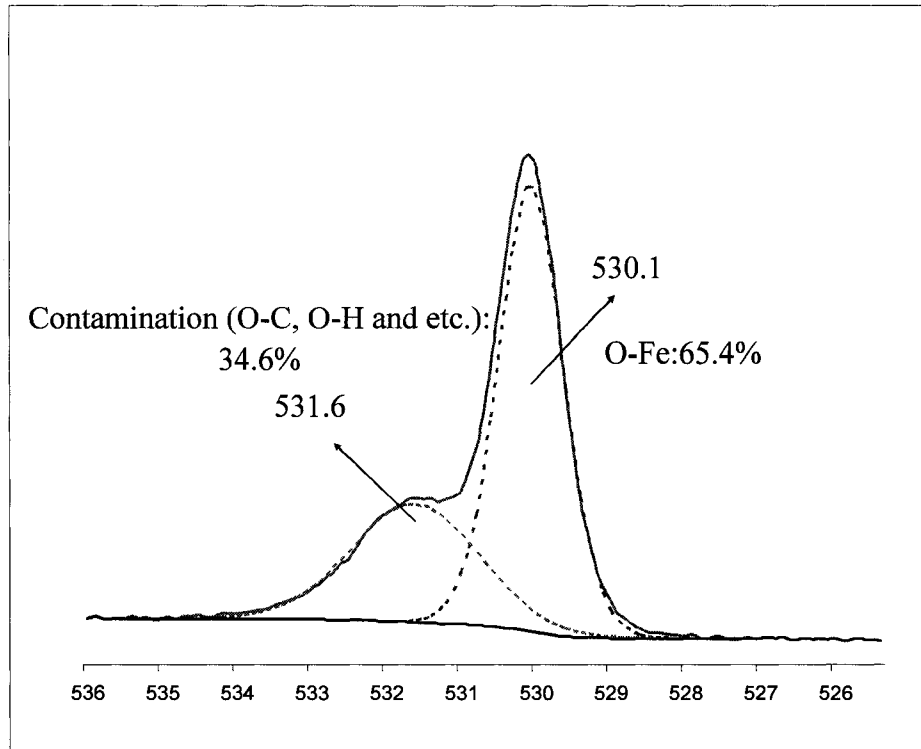


Figure 4.1: The O 1s high-resolution XPS spectrum for the iron oxide surface

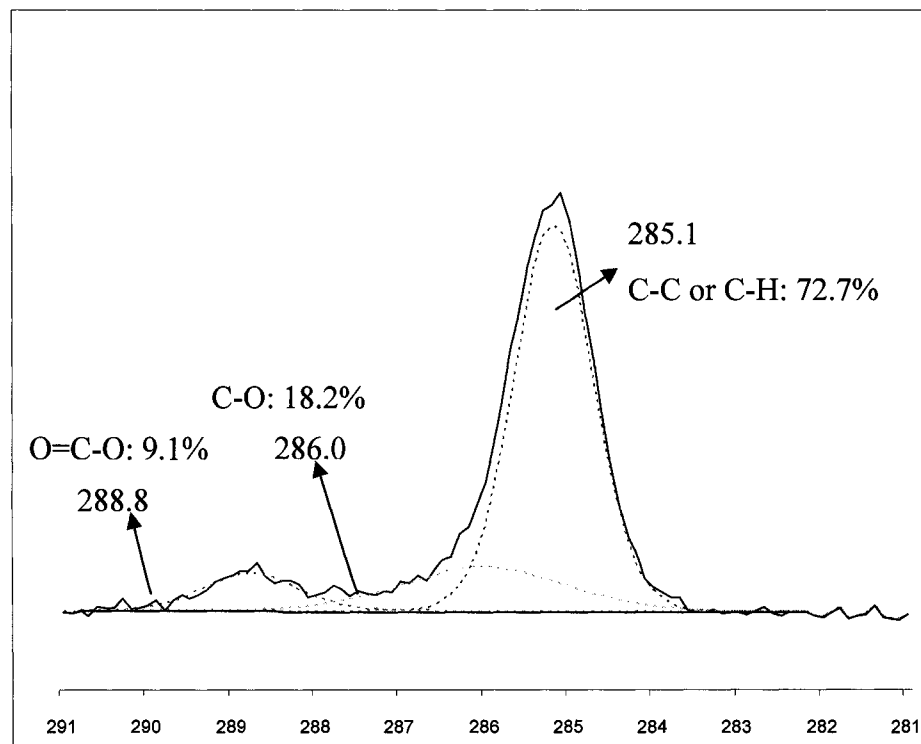


Figure 4.2: The C 1s high-resolution XPS spectrum for the iron oxide surface

The carbon peak comprises three sub-peaks. The major one with a binding energy of 285.1 eV is assigned to C-C and C-H bonding and constitutes about 72.7% of the total carbon. The sub-peak at a higher binding energy of 286.0 eV (18.2%) can be assigned to C-O bonding and the sub-peak at a binding energy of 288.8 eV (9.1%) corresponds to carbon atoms that have one ketonic oxygen atom and one non-ketonic oxygen atom. The majority of carbon contamination comes in the form of C-C and C-H and the rest of the carbon contamination exists in different forms of carbon oxygen bonding.

Clearly, contamination needs to be factored out to attain a better understanding of the underlying surface composition. As indicated in Figure 4.2, about 3.22 wt% of C is associated with carbon oxygen bonding. From this, 4.83 wt% of O is linked to carbon oxygen bonding, either O-C as O=C-O. From Figure 4.1, 18 wt% O is present in O-Fe bonding while 9.53 wt% O is linked to contamination. As 4.83 wt% O is linked with C, 4.70 wt% (9.53 wt% - 4.83 wt%) of O can be assigned to O-O or O-H bonding. Thus oxygen and water are present on the surface as well. As a result, the atomic ratio of O to Fe of the underlying surface is 0.91 +/- 0.05, indicating a surface comprising FeO_{0.91} rather than Fe₂O₃. In either event, the surface remains basic.

4.2.3 Composition and Contamination of the Iron Sulfide Surface

From Table 4.1, it is also noted that the iron sulfide surface is contaminated with elements like carbon and nitrogen. The high-resolution spectra of carbon and oxygen elements are

shown in Figure 4.3 and Figure 4.4.

In Figure 4.3, the O 1s peak is fitted into three sub-peaks. The one with the lowest binding energy of 529.8 eV (35.8%) corresponds to O-Fe bonding. Thus, the iron sulfide film is so thin that the iron oxide beneath it is also detected. The other two sub-peaks with higher binding energy of 531.6 eV (52%) and 533.1 eV (12.1%) mainly correspond to O-C, O-H and O-O bonding. Figure 4.4 shows the C 1S high-resolution spectrum which is quite similar to the one on the iron oxide surface. The major carbon contamination is from the sub-peak with a binding energy of 284.7 eV (70.0%). The rest (30%) of the carbon present has high binding energies of 285.8 eV (20.5%) and 288.4 eV (9.5%), respectively. They can be assigned to C-O, O=C-O, etc..

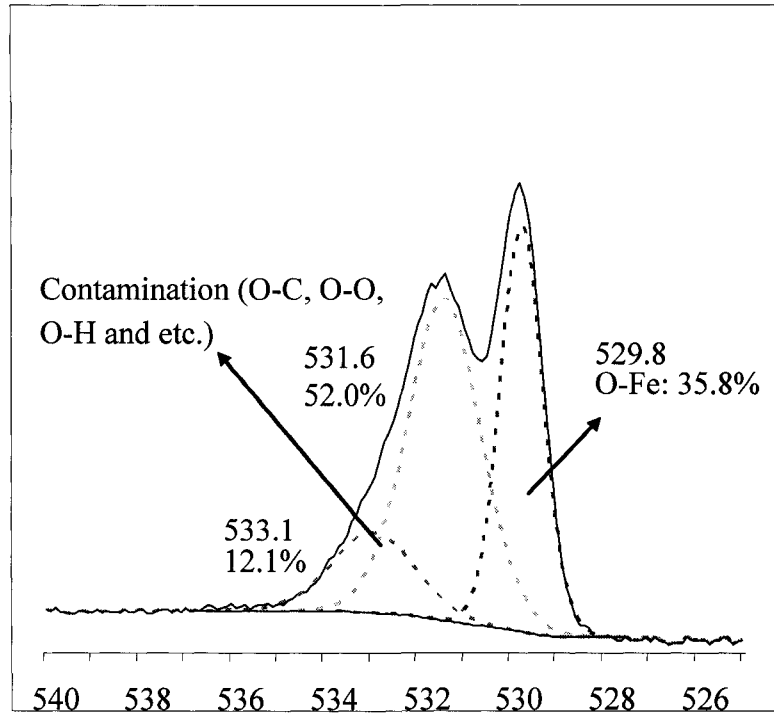


Figure 4.3: The O 1S high-resolution spectrum for the iron sulfide surface

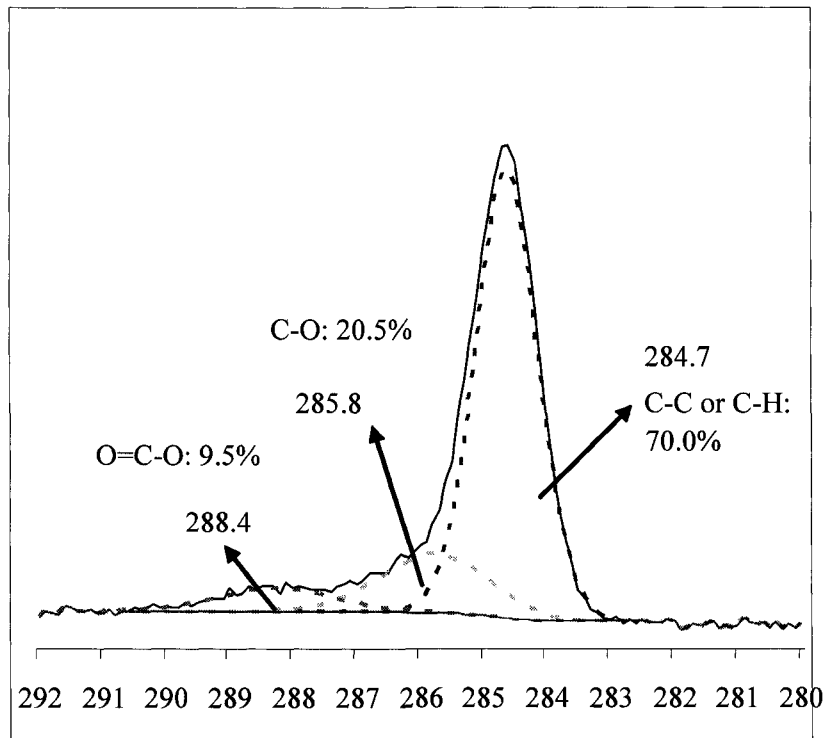


Figure 4.4: The C 1S high-resolution spectrum for the iron sulfide surface

The same mathematics used for the contamination on the iron oxide surface is applied here. Figure 4.4 indicates that 7.45 wt% carbon is associated with 9.81 wt% oxygen. Figure 4.3 illustrates that 6.15 wt% oxygen is from O-Fe bonding and 11.02 wt% oxygen is regarded as contamination. Consequently, there is about 1.21 wt% of oxygen corresponds to O-O and O-H bonding, which implies O₂ and H₂O. It is also noted that 18.63 wt% of iron is from Fe-S bonding. As a result, the atomic ratio of S to Fe of the surface is 1.60 +/- 0.30, indicating a surface comprising FeS_{1.60}, which is acidic.

4.2.4 Composition and Contamination of the Nickel Surface

It is illustrated that the nickel surface is apparently contaminated with O, N, C and S elements. The high resolution XPS spectra of oxygen and carbon elements are shown in Figure 4.5 and 4.6. In Figure 4.5, the O 1s peak is fitted into three sub-peaks. The one with lowest binding energy of 529.6 eV correspond to O-Ni bond. The amount of oxygen in this category is about 31.4% of the total oxygen on the surface. The other two sub-peaks with higher binding energy of 531.3 eV and 532.0 eV correspond to O-C, O-H and other forms of oxygen bonding. As indicated in Figure 4.6, the majority carbon contamination exists in the form of C-C and C-H. At the same time, there is also some carbon at higher binding energy that presents in the form of C-O, O-C=O, etc..

Figure 4.6 also shows that the amount of carbon associated with oxygen constitutes 3.98 wt%. Thus it can be calculated that 5.67 wt % of oxygen is involved in oxygen carbon

bonding. From Figure 4.5, it can be seen that 5.62 wt % oxygen is linked to O-Ni bonding. So, there is about 6.60 wt % oxygen as water or oxygen. Moreover, the atomic ratio of oxygen to nickel is 0.3. If nickel is oxidized to NiO, only 30% area of nickel surface is oxidized and the balance is metallic. However, the nickel surface can still be considered as a neutral one.

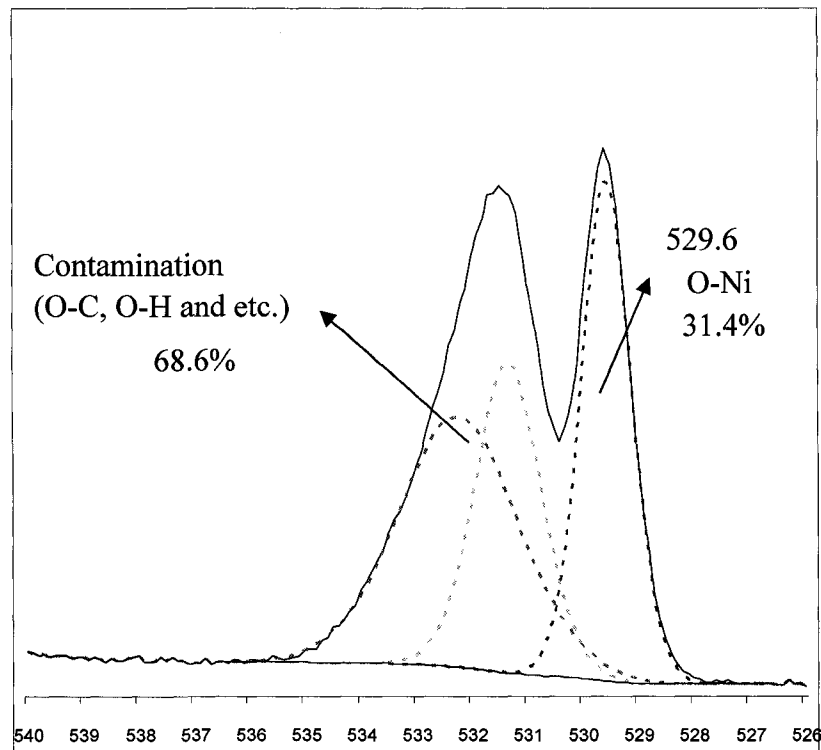


Figure 4.5: The O 1s high-resolution XPS spectrum for the nickel surface

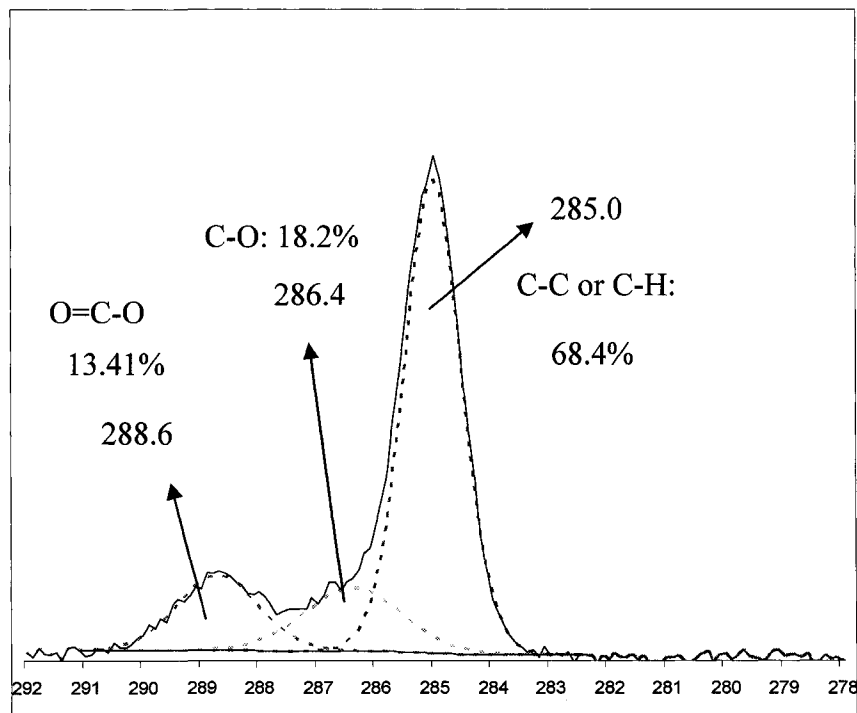


Figure 4.6: The C 1s high-resolution XPS spectrum for the nickel surface

4.2.5 Composition and Contamination of the Silicon Surface

As expected, surface contamination on silicon surface is clear as well. The high resolution spectra from XPS of oxygen and carbon are shown in Figure 4.7 and Figure 4.8 respectively. Unexpectedly, the oxygen spectrum on silicon surfaces is quite different from that on iron oxide and nickel surfaces. There is only a single oxygen peak with binding energy of 525.5 eV which coincides with the binding energy of O-Si. As discussed in Chapter 3, silicon surfaces are naturally oxidized into silicon dioxide or silica surface. However, it is possible that oxygen bonded with other elements has the same binding energy. The carbon spectroscopy from silicon surface is similar to that from other surfaces. The majority of the carbon contamination is from C-C and C-H bonding. C-O and O-C=O are also detected at higher binding energies.

Again, it is illustrated by Figure 4.8 that 2.41 wt % carbon is with oxygen, and on the other hand, 2.71 wt % oxygen is with carbon. The rest 23.01 wt % oxygen is with silicon. Consequently, the atomic ratio of oxygen to silicon is 0.72 which is much lower than the ratio from SiO₂. However, this merely reflects the thinness of the natural oxide layer. The analysis depth exceeds the thickness of the layer. The surface is acidic.

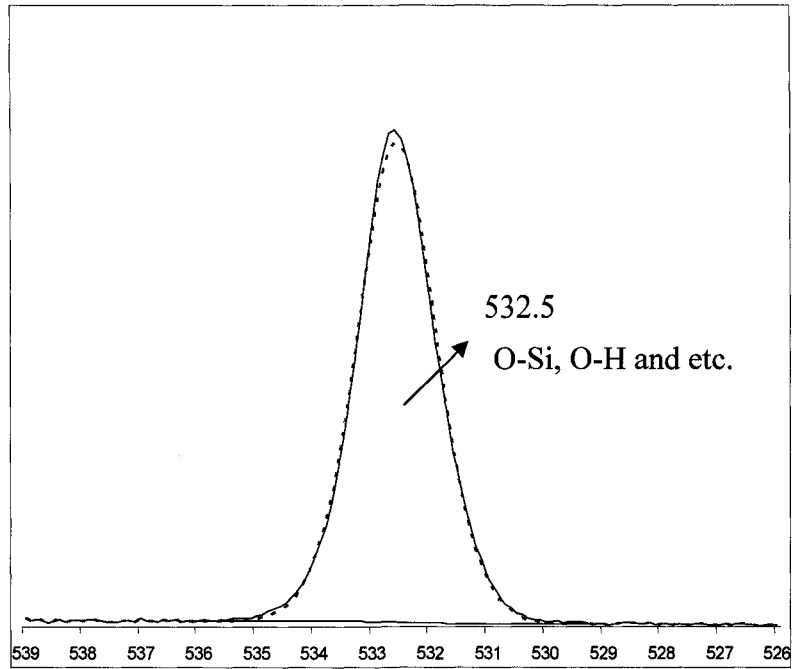


Figure 4.7: The O 1s high-resolution XPS spectrum for the silicon surface

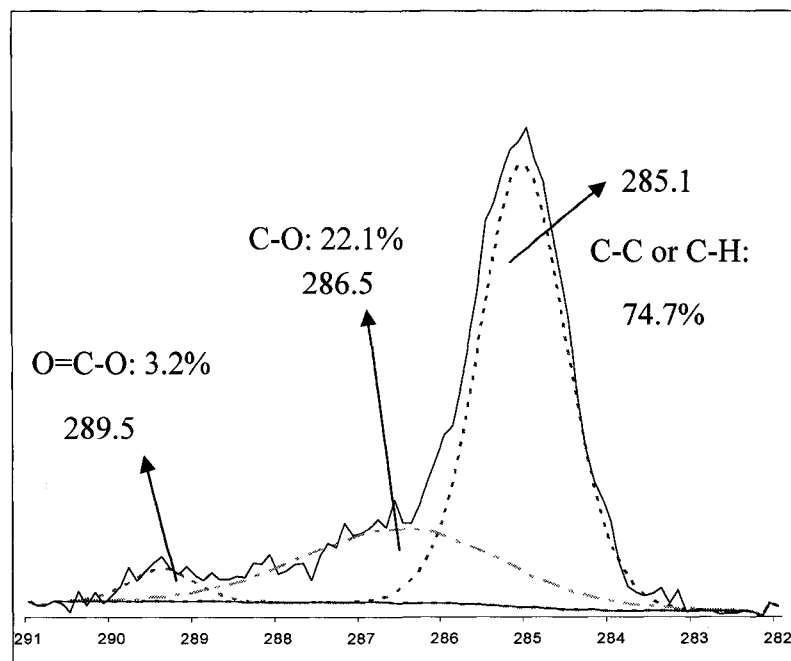


Figure 4.8: The C 1s high-resolution XPS spectrum for the silicon surface

4.2.6 Substrate Composition Summary

As discussed above, surface contamination is unavoidable. XPS analysis permits the evaluation of surfaces on a contaminant free basis. These are shown pictorially in Figure 4.9. Their form and composition differ from expectation at the outset but meet the requirements established, namely a selection of acidic (SiO_2 , $\text{FeS}_{1.6}$), neutral (mixed Ni and NiO) and basic ($\text{FeO}_{0.9}$) surfaces.

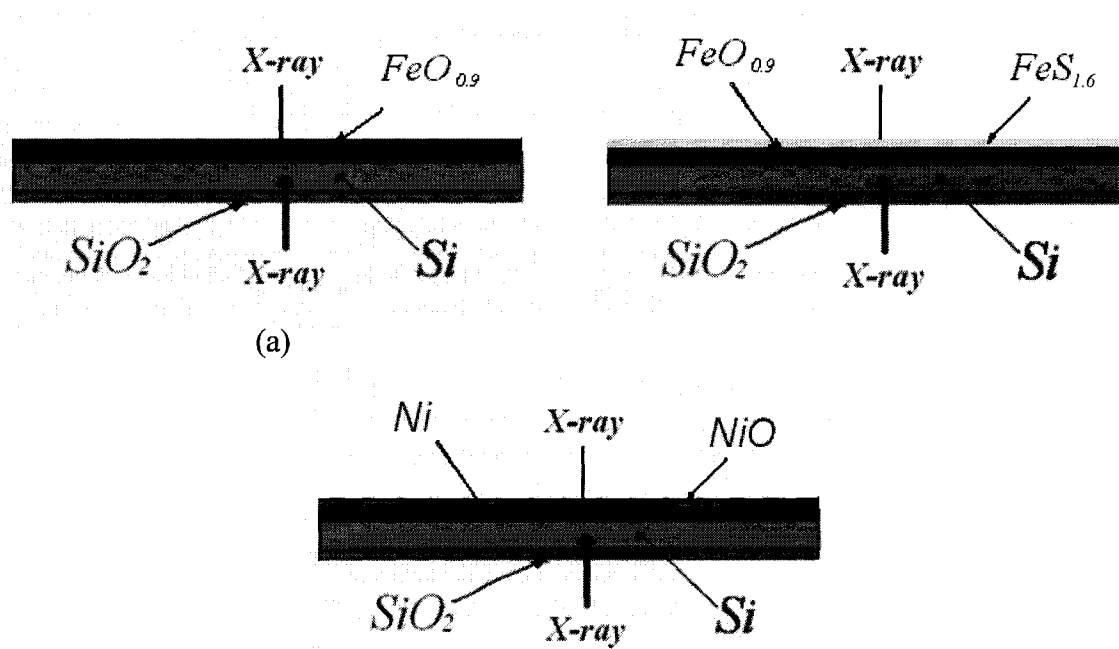


Figure 4.9: Surfaces used in the organic deposition experiments

4.3 Deposition of Model Compounds

4.3.1 Negative Controls

Negative control experiments have been performed with pentane and pentane + pyrene mixtures. The XPS analysis results for pentane, with $t_1 = 3.5$ hours and $t_2 = 30$ minutes, are shown in Table 4.2. As expected, pentane does not sorb on either iron oxide or silica surfaces. The surface compositions are the same as the substrate, Table 4.1, within experimental error.

Table 4.2: Surface composition on iron oxide and silica surfaces for pentane

	Iron Oxide	Silica
Fe	55.58	0.00
Si	0.00	66.73
O	25.57	25.44
N	0.08	0.10
C	18.42	7.72
S	0.35	0.00

XPS results for pentane + pyrene, with $t_1 = 3.5$ hours, $t_2 = 30$ minutes and a pyrene mass fraction of 2.52% on iron oxide and silica surfaces are shown in Table 4.3. Again, the surface composition on iron oxide surface is the same as the substrate, as shown in Table 4.1, within experimental error. However, deposition on the silica surface is observed. From equation 3.8, the thickness of deposit on the silica surface is 0.19 ± 0.05 nm. The

deposit thickness is about the same order of magnitude as the length of a carbon-carbon bond (~0.15 nm). It is likely due to partial coverage on the silica surface. From equation 3.7, surface compositions corrected for substrate and contamination layer 1 are shown in Table 4.3 as well. Deposits are only composed of carbon within experimental error.

Table 4.3: Surface composition on iron oxide and silica surfaces for pentane + pyrene

	Iron Oxide	Silica	Substrate and contamination layer 1 free on Silica
Fe	56.03 +/- 1.92	0.00	0.00
Si	0.00	53.32 +/- 2.64	0.00
O	24.90 +/- 0.46	24.66 +/- 2.48	1.35 +/- 2.37
N	0.23 +/- 0.09	0.77 +/- 0.18	0.37 +/- 0.18
C	18.12 +/- 1.58	20.34 +/- 3.60	11.9 +/- 3.82
S	0.74 +/- 0.73	0.92 +/- 0.86	

The negative control results indicate that this technique can distinguish the occurrence of deposition and can detect the partial coverage of deposits on acidic and basic surfaces.

4.3.2 Positive Controls

Positive control experiments have been performed with several model compounds including naphthenic acid, zinc naphthenate, zinc TPP and nickel TPP. Table 4.4 shows the XPS results for naphthenic acid deposition on both iron oxide and silica surface with $t_1 = 3.5$ hours and $t_2 = 30$ minutes. From the compositions of iron and silica on the

exposed surfaces, naphthenic acid is deposited on both iron oxide and silica surfaces. Surface composition corrected for substrate and contamination layer 1 is also shown in Table 4.4. Corrected deposits are mainly composed of carbon and oxygen elements, which are the major elements of naphthenic acid. Again, from equation 3.8, the thickness of deposit on the iron oxide surface is 0.05 +/- 0.01 nm and that on the silica surface is 0.18 +/- 0.07 nm. Partial coverage is realized in both cases. Clearly it is difficult to realize quantitative composition measurements on films that are only 0.05 nm thick but at 0.2 nm the composition of the contaminant free deposit approaches that of the depositing compound.

Table 4.4: Surface composition on iron oxide and silica surfaces for naphthenic acid

	Iron Oxide	Substrate and contamination layer 1 free on Iron Oxide	Silica	Substrate and contamination layer 1 free on Silica	Naphthenic Acid (Normalized to H free)
Fe	49.79 +/- 1.99	0.00	0.00	0.00	0.00
Si	0.00	0.00	54.02 +/- 3.59	0.00	0.00
O	31.86 +/- 0.37	5.04 +/- 0.32	26.64 +/- 1.03	3.18 +/- 1.57	17.62
N	0.33 +/- 0.14	0.1 +/- 0.14	0.35 +/- 0.47	-0.05 +/- 0.47	0.03
C	14.59 +/- 1.09	3.17 +/- 1.19	17.01 +/- 3.11	8.5 +/- 3.45	82.35
S	3.42 +/- 1.05		1.98 +/- 2.44		0.00

The XPS results for naphthenic acid (15 wt %) + pentane are presented in Table 4.5. Surface composition corrected for substrate and contamination layer 1 on silica is also

shown. Nothing is deposited on the iron oxide surface within experimental error while the deposit thickness on the silica surface is unchanged at 0.17 ± 0.07 nm. Again, the corrected deposit comprises carbon and oxygen where the ratio of carbon to oxygen is equal to that of naphthenic acid within experimental error.

Table 4.5: Surface composition on iron oxide and silica surfaces for naphthenic acid (15 wt %) + pentane

	Iron Oxide	Silica	Substrate and contamination layer 1 free on Silica	Naphthenic Acid (Normalized to H free)
Fe	54.68 +/- 0.41	0.00	0.00	0.00
Si	0.00	54.37 +/- 3.49	0.00	0.00
O	29.23 +/- 0.31	26.82 +/- 0.81	3.27 +/- 0.46	17.62
N	0.21 +/- 0.11	0.49 +/- 0.07	0.09 +/- 0.07	0.03
C	13.98 +/- 1.55	16.86 +/- 2.42	8.31 +/- 2.74	82.35
S	1.92 +/- 0.78	1.47 +/- 2.17		0.00

The surface composition of deposits for zinc naphthenate (15 wt %) + pentane is given in Table 4.6. Deposition took place on both the iron oxide and silica surfaces. The thickness of the deposit on the iron oxide surface is 0.09 ± 0.02 nm and that on the silica surface is 1.02 ± 0.15 nm. The thickness of a benzene molecule is ~ 0.37 nm and its length is ~ 0.7 nm. The deposit thickness on silica is about the same as the length of a benzene molecule. Corrected deposits composition on iron oxide is mainly zinc and carbon, while

corrected deposits composition on silica is mainly zinc, oxygen and carbon. On the iron oxide surface, there is too little oxygen and carbon relative to zinc, unless the naphthenate is decomposed on the surface. On the silica surface, the ratio of zinc to oxygen is correct but there is too little carbon for zinc naphthenate to be the sorbing species. The deposit thickness is sufficient to obtain an accurate composition measurement. This matter merits further investigation.

Table 4.6: Surface composition on iron oxide and silica surfaces for zinc naphthenate (15 wt %) + pentane

	Iron Oxide	Substrate and contamination layer 1 free on Iron Oxide	Silica	Substrate and contamination layer 1 free on Silica	Zinc Naphthenate (Normalized to H free)
Zn	5.88 +/- 0.74	5.88 +/- 0.74	8.57 +/- 0.97	8.57 +/- 0.97	9.33
Fe	43.93 +/- 2.64	0.00	0.00	0.00	0.00
Si	0.00	0.00	24.04 +/- 3.43	0.00	0.00
O	25.65 +/- 0.50	-0.57 +/- 0.26	24.69 +/- 1.08	9.48 +/- 1.82	10.52
N	0.07 +/- 0.08	-0.15 +/- 0.09	0.39 +/- 0.15	0.07 +/- 0.15	0.02
C	23.00 +/- 3.89	11.89 +/- 4.03	39.89 +/- 4.01	34.87 +/- 4.46	80.13
S	1.48 +/- 0.77		2.43 +/- 1.70		0.00

Deposit composition for zinc TPP (15 wt %) + pentane and nickel TPP (15 wt %) + pentane systems are shown in Tables 4.7 and 4.8, respectively. The deposit thickness for zinc TPP + pentane is 0.05 +/- 0.01 nm on the iron oxide surface and 0.34 +/- 0.08 nm on the silica surface. The corrected deposit composition on the thicker silica surface,

composed of zinc, nitrogen and carbon approximates the composition of zinc TPP. For the thinner deposit on the iron oxide surface, the approximation is poorer as expected. The deposit thickness for nickel TPP + pentane is 0 nm on the iron oxide surface and 0.12 +/- 0.02 nm on the silica surface. Again, the corrected deposit composition on the silica surface, composed of nickel, nitrogen and carbon approximates the composition of nickel TPP.

Table 4.7: Surface composition on iron oxide and silica surfaces for zinc TPP (15 wt %) + pentane

	Iron Oxide	Substrate and contamination layer 1 free on Iron Oxide	Silica	Substrate and contamination layer 1 free on Silica	Zinc TPP (Normalized to H free)
Zn	3.00 +/- 0.86	3.00 +/- 0.86	3.52 +/- 0.10	3.52 +/- 0.10	10.07
Fe	49.12 +/- 1.38	0.00	0.00	0.00	0.00
Si	0.00	0.00	46.35 +/- 3.68	0.00	0.00
O	24.01 +/- 0.15	-2.75 +/- 0.01	18.52 +/- 0.79	-3.10 +/- 0.09	0.00
N	0.97 +/- 0.11	0.74 +/- 0.08	2.04 +/- 0.11	1.65 +/- 0.08	8.63
C	21.97 +/- 1.61	10.58 +/- 1.19	28.10 +/- 5.37	20.40 +/- 4.08	81.31
S	0.96 +/- 1.05		1.48 +/- 0.91		0.00

Table 4.8: Surface composition on iron oxide and silica surfaces for nickel TPP
(15 wt %) + pentane

	Iron Oxide	Silica	Substrate and contamination layer 1 free on Silica	Ni TPP (normalized on a H free basis)
Ni	0.00	0.22 +/- 0.01	0.22 +/- 0.01	9.18
Fe	57.84 +/- 0.51	0.00	0.00	0.00
Si	0.00	57.34 +/- 0.94	0.00	0.00
O	24.91 +/- 0.03	23.82 +/- 0.32	-0.41 +/- 0.08	0.00
N	0.17 +/- 0.08	0.72 +/- 0.33	0.31 +/- 0.23	8.72
C	16.28 +/- 1.53	16.19 +/- 0.99	7.34 +/- 0.77	82.17
S	0.81 +/- 1.14	1.74 +/- 0.05		0.00

The positive control experiments illustrate the sensitivity of the analysis, i.e. partial coverage and monolayer coverage are detectable on both acidic and basic surfaces as summarized in Table 4.9. The model compounds all sorb more strongly to the acidic silica surface. Further, deposit compositions corrected for contamination layer 1, appear to reflect the composition of the depositing species, within experimental error for deposits at least 0.1 nm thick. Further investigation is needed to evaluate the depositing species for the zinc naphthenate + pentane case.

Table 4.9: Deposit thickness for model compounds

	Iron Oxide	Silica
Pentane	not material	not material
Pyrene + Pentane	not material	0.19 +/- 0.05 nm
Naphthenic Acid	0.05 +/- 0.01 nm	0.18 +/- 0.07 nm
Naphthenic Acid + Pentane	not material	0.17 +/- 0.07 nm
Zinc Naphthenate + Pentane	0.09 +/- 0.02 nm	1.02 +/- 0.15 nm
Zinc TPP + Pentane	0.05 +/- 0.01 nm	0.34 +/- 0.08 nm
Nickel TPP + Pentane	not material	0.12 +/- 0.02 nm

4.4 Deposition of Athabasca Bitumen Constituents

The control experiments show that deposition differences are expected on acidic and basic surfaces. As indicated in Chapter 3, the whole experimental matrix was performed with the iron oxide surface as the principal surface. Nickel/nickel oxide, iron sulfide and silica surfaces are evaluated for a limited number of cases.

4.4.1 Thickness of Deposits on Basic Surfaces

4.4.1.1 Thickness of Deposits vs. Time Variables

Two temperature variables are introduced in Chapter 3. t_1 represents the time that a substrate is exposed to mixtures above the deposition boundary. t_2 represents the time that a substrate is exposed to pentane at room temperature. The IMFP (λ) of iron element with a kinetic energy of 776.6 eV is 0.81 nm.

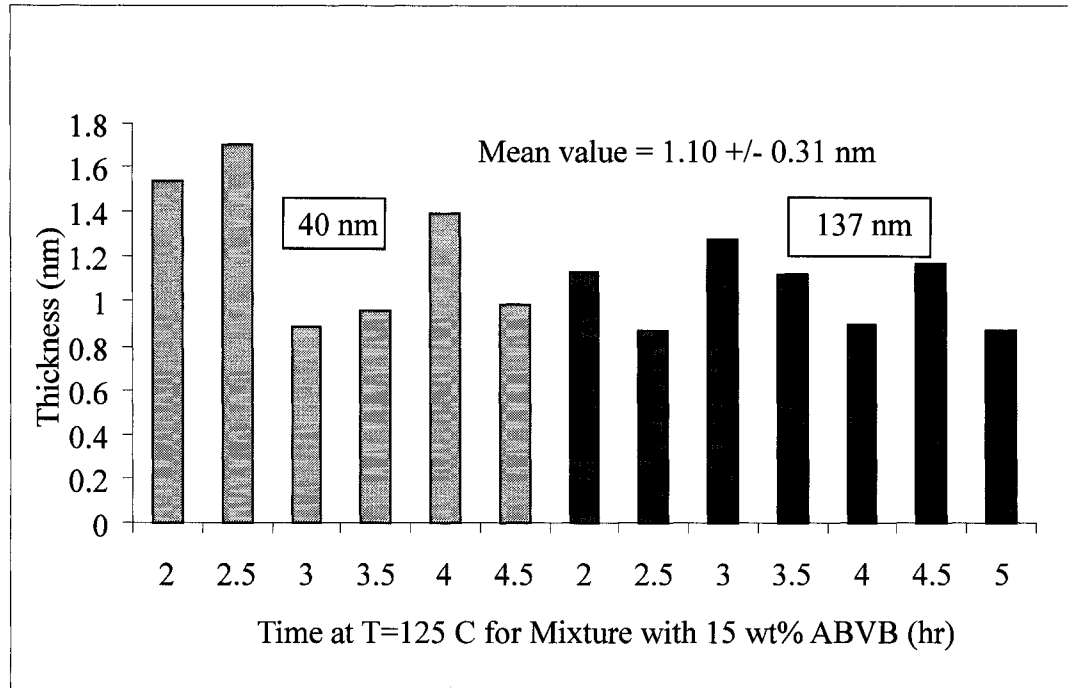


Figure 4.10: Thickness of deposit on the iron oxide surface vs. t_1 at $t_2 = 30$ minutes

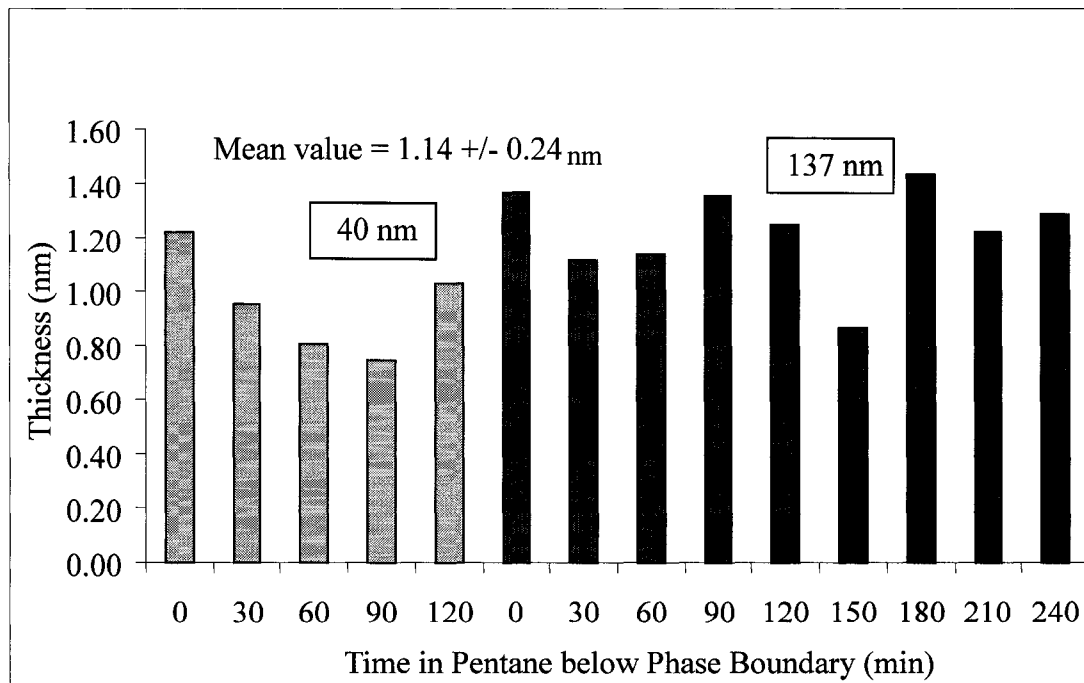


Figure 4.11: Thickness of deposit on the iron oxide surface vs. t_2 at $t_1 = 3.5$ hours

Figures 4.10 and 4.11 show that the thickness of the iron oxide film, t_1 and t_2 , have no measurable effect on deposit thickness which is ~ 1.12 nm on iron oxide surfaces.

4.4.2 Thickness of Deposits on Neutral Surfaces

4.4.2.1 Thickness of Deposits vs. Time Variable

The thickness of the deposit on the nickel/nickel oxide surface was evaluated as a function of variable t_1 . The thickness of the nickel film was 100 nm. t_2 was fixed at 30 minutes, and the composition was fixed at 15 wt % ABVB. The IMFP (λ) of nickel element with a kinetic energy of 620 eV is 0.60 nm.

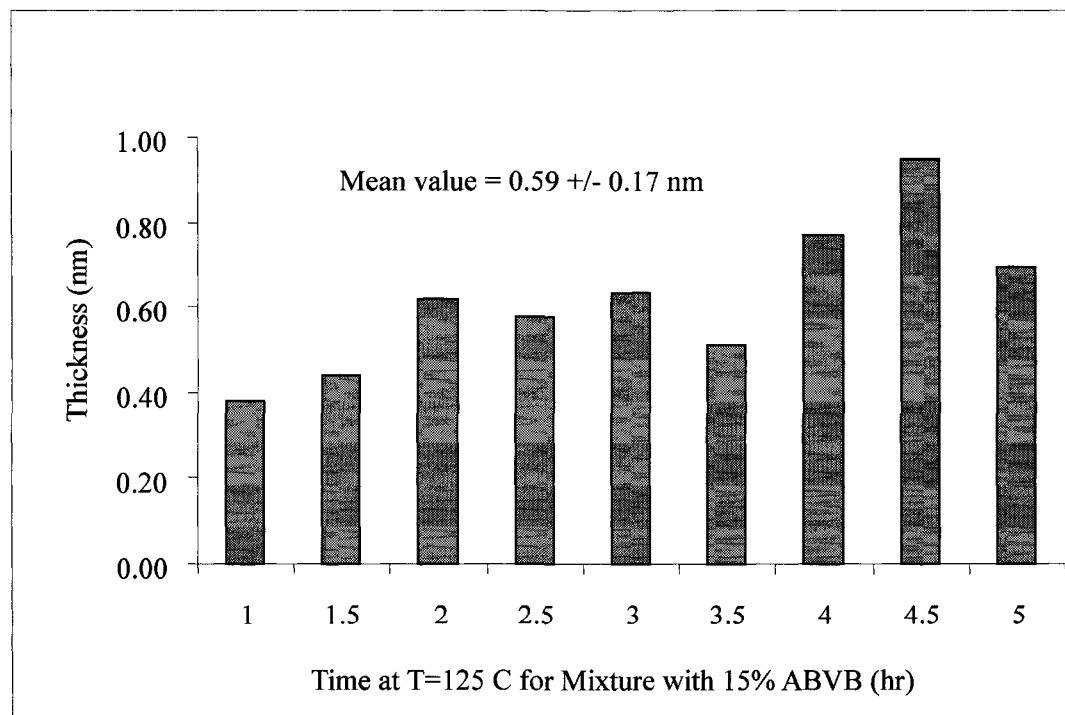


Figure 4.12: Thickness of deposit on nickel surface vs. t_1 at $t_2 = 30$ minutes

The thickness of deposit on the nickel/nickel oxide surface increases slightly with t_1 .

However, the mean value of the thickness on the nickel/nickel oxide surface is ~ 0.59 nm which is about half the thickness on the iron oxide surface (~ 1.12 nm).

4.4.3 Thickness of Deposits on Acidic Surfaces

4.4.3.1 Thickness of Deposits vs. Time Variable

The same experiments performed on the nickel surface were also performed on the silica surface. The IMFP (λ) of silicon element with a kinetic energy of ~ 1380 eV is 2.37 nm. Figure 4.13 shows the deposit thickness on silica is not affected by variable t_1 . The thickness of the deposit on the silica surface, for $t_2 = 30$ minutes and ABVB wt % = 15%, and over the range of t_1 values, is on average ~ 2.88 nm. Experiments performed on the iron sulfide surface, which is also an acidic surface, with t_1 of 3.5 hours, t_2 of 30 minutes and ABVB 15 wt%, yielded an average deposit thickness of 1.41 ± 0.25 nm which is lower than that from the silica surface but still larger than that from iron oxide and nickel surfaces.

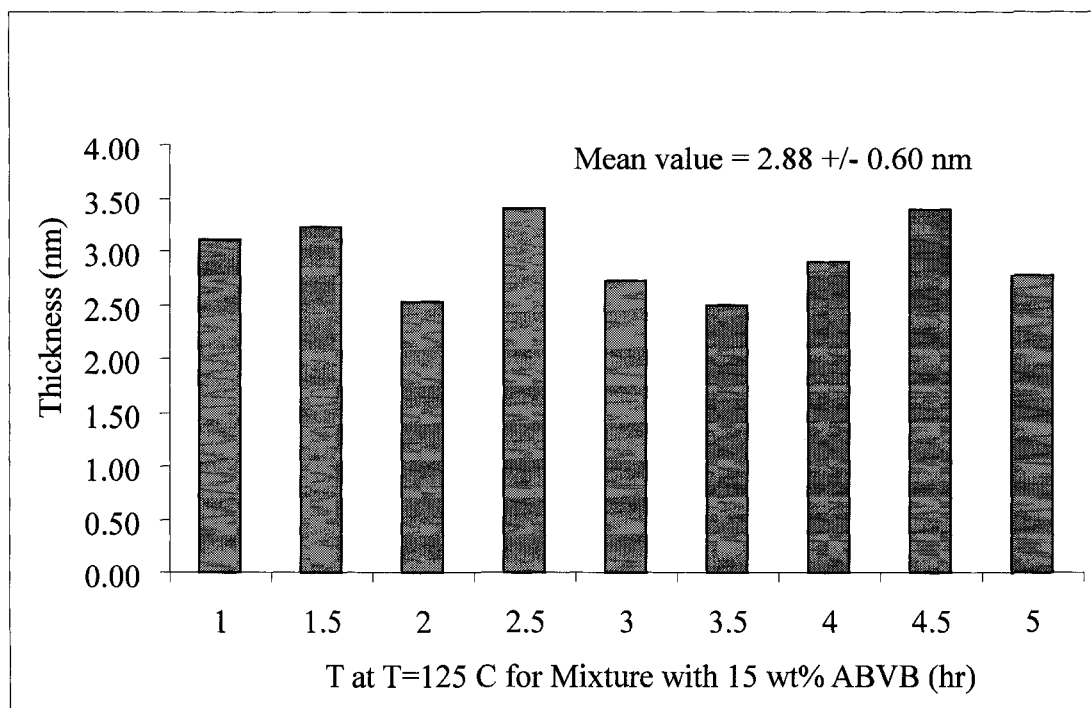


Figure 4.13: Thickness of deposit on the silica surface vs. t1 at t2 = 30 minutes

4.4.4 Comparison of Thickness of Deposits on all Surfaces

The thicknesses of deposits on iron oxide, nickel, iron sulfide and silica surfaces are plotted together in Figure 4.14 and Figure 4.15. In Figure 4.15, it is evident that the thickness is highest on the acidic silica surface (3.26 +/- 0.45 nm), lower on the basic iron oxide surface (1.41 +/- 0.27 nm) and lowest on the neutral nickel/nickel oxide surface (0.84 +/- 0.21 nm). The greatest deposit thickness tends to take place at ABVB 45 wt% on all three surfaces. There is a weak indication that ABVB + pentane deposition is somehow connected to its phase behavior as shown in Figure 1.3. The thickest deposit appears to be greatest within the four-phase zone as shown in Figure 4.16 where the phase diagram is superimposed on the deposit thickness results. The average organic deposit thicknesses for sets of experiments are shown in Table 4.10.

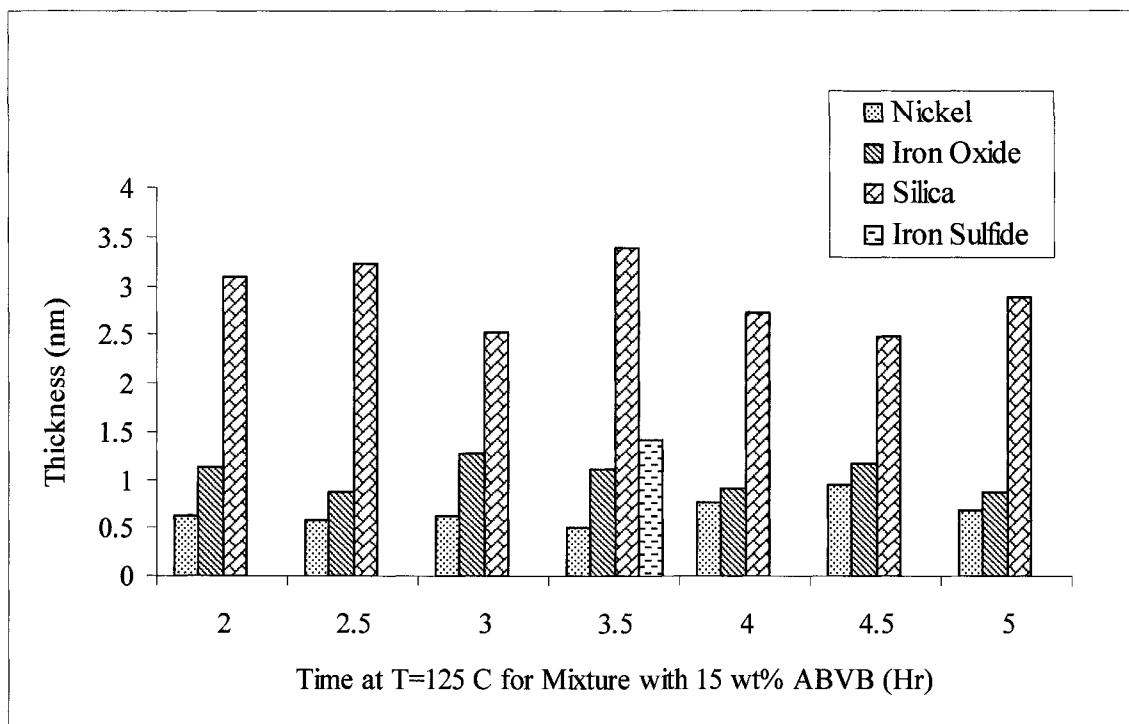


Figure 4.14: Thickness of deposits on iron oxide, nickel, iron sulfide and silica surfaces vs. t1 at t2 = 30 minutes

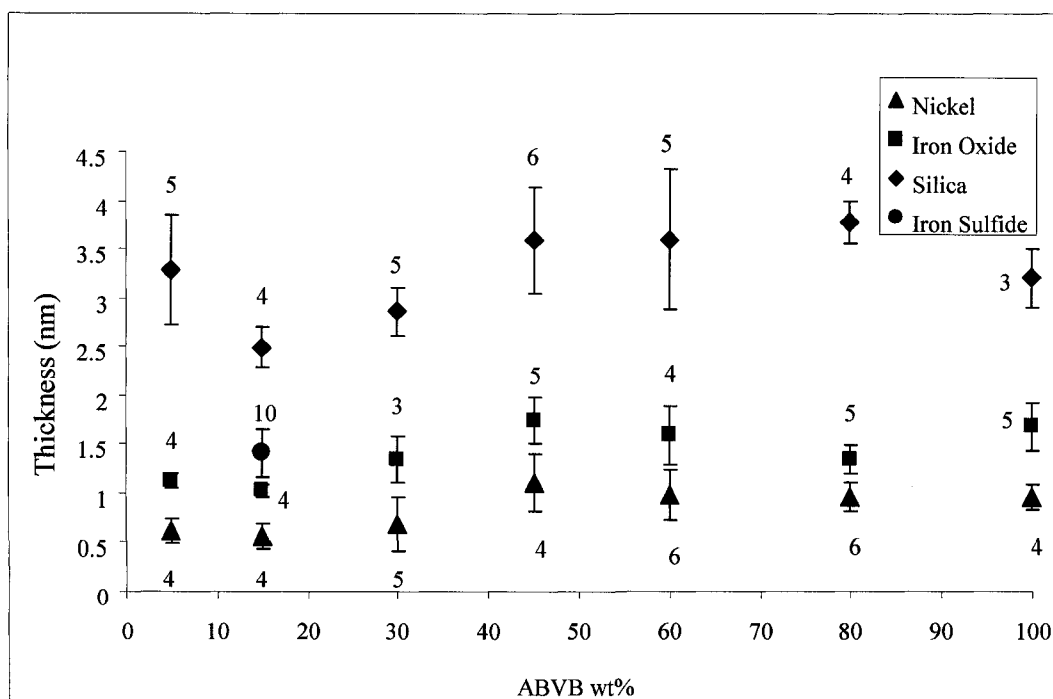


Figure 4.15: Thickness of deposits on iron oxide, nickel and silica surfaces vs. ABVB mass fraction at t1 = 3.5 hours and t2 = 30 minutes. (The numbers of repetitions of each experiment is a parameter.)

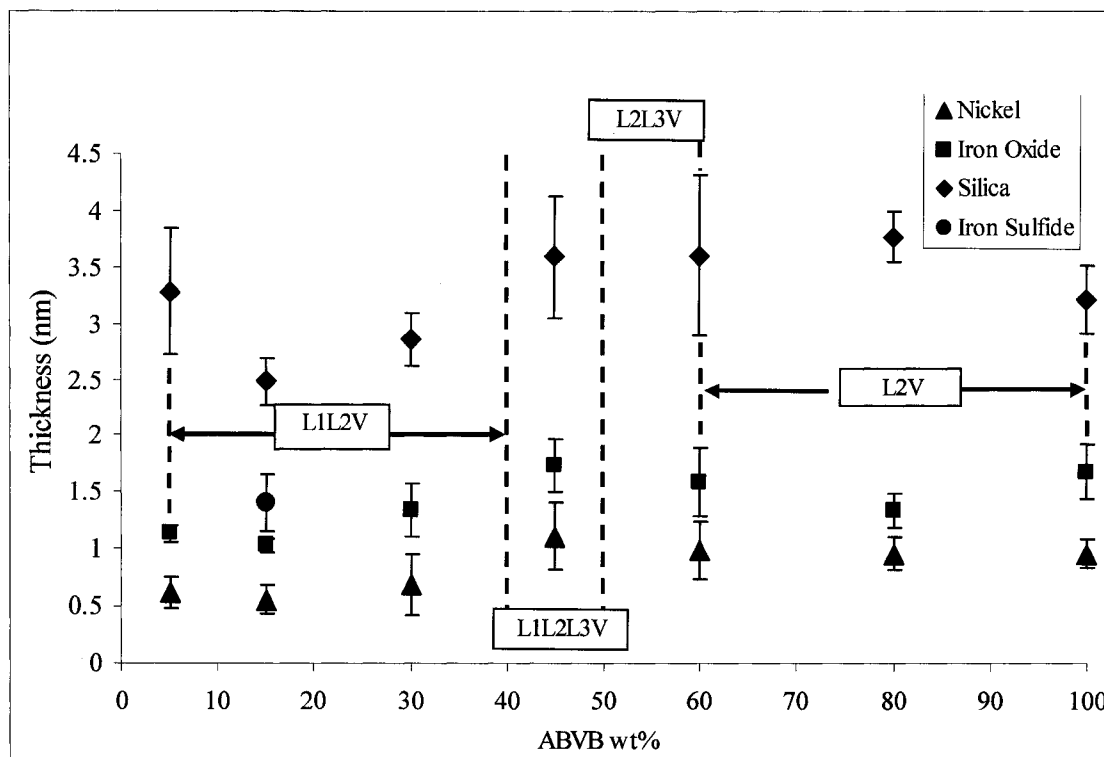


Figure 4.16: Connection between thickness of deposit and phase behavior

Table 4.10: Organic deposit thickness from experiment set 1 and 2

Deposit Thickness	Experiment Set 1 (t1 as variable)		Experiment Set 2 (composition as variable)	
	t2=30 min, ABVB wt%=15%	# of Exp.	t1=3.5 hr, t2=30 min	# of Exp.
Iron Oxide	1.10 +/- 0.31 nm	23	1.41 +/- 0.27 nm	30
Nickel	0.59 +/- 0.17 nm	34	0.84 +/- 0.21 nm	33
Iron Sulfide	1.41 +/- 0.25 nm	16	N/A	
Silica	2.88 +/- 0.60 nm	20	3.26 +/- 0.45 nm	32

4.5 ABVB Deposit Composition

In this section, the composition of deposits is discussed on a contaminant free basis. As the deposits are thick compared to those of model compounds, compositions on a contamination free basis are robust for detectible constituents with significant mass fractions. From the elemental analysis of ABVB, Tables 3.9 and 3.10, the easiest and least ambiguous way to present the composition data is in the form of carbon to sulfur ratios. These are presented here as functions of the time variables and ABVB mass fraction. The carbon to sulfur ratio for Athabasca bitumen vacuum residue (ABVB), 11.9, Athabasca maltenes (asphaltene free oil), 13.0, and Athabasca asphaltenes, 10, are used as benchmarks.

4.5.1 Composition of Deposit on Basic Surfaces

The whole experimental matrix was performed on iron oxide surfaces. Experiments where t_1 , t_2 and substrate surface thickness were variables were performed. Figures 4.17 and 4.18 show that variable t_1 , t_2 and iron oxide film thickness do not affect C1/S ratio at ABVB 15 wt %. The value of C1/S ratio is ~ 11.3 for both the 40 nm and 137 nm thick films. The deposit is slightly enriched in asphaltene-like materials relative to the feed. The deposits are not asphaltenes per se.

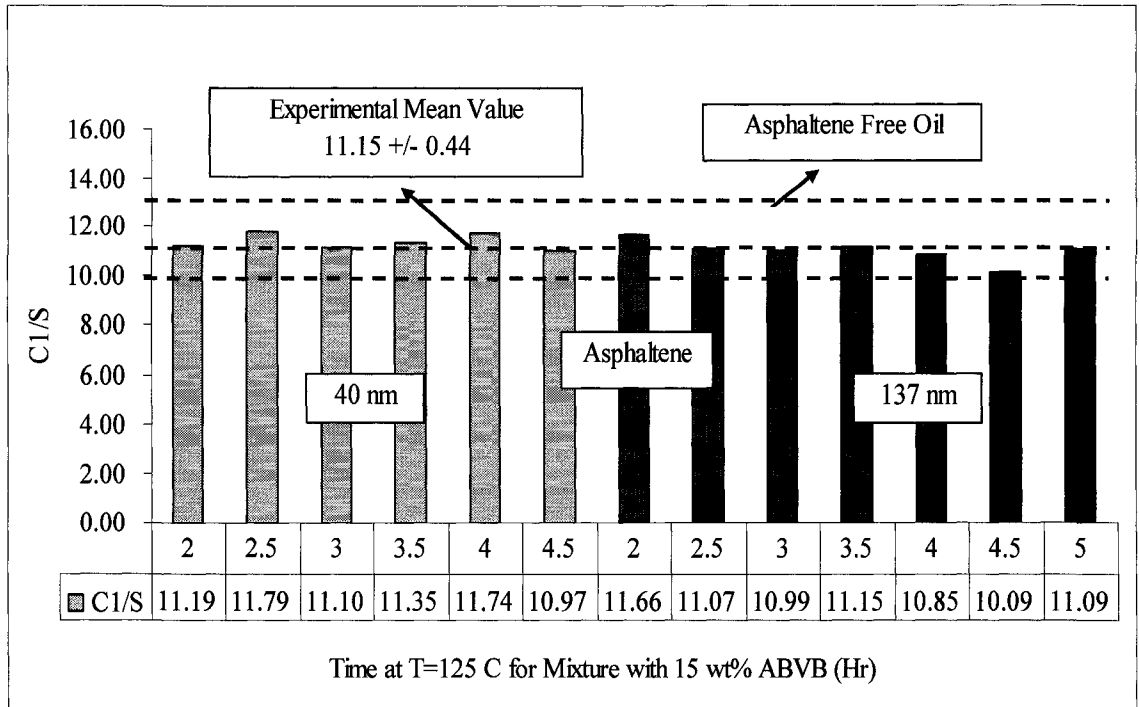


Figure 4.17: C1/S on iron oxide surface vs. t1 at t2 = 30 minutes and ABVB composition = 15 wt %

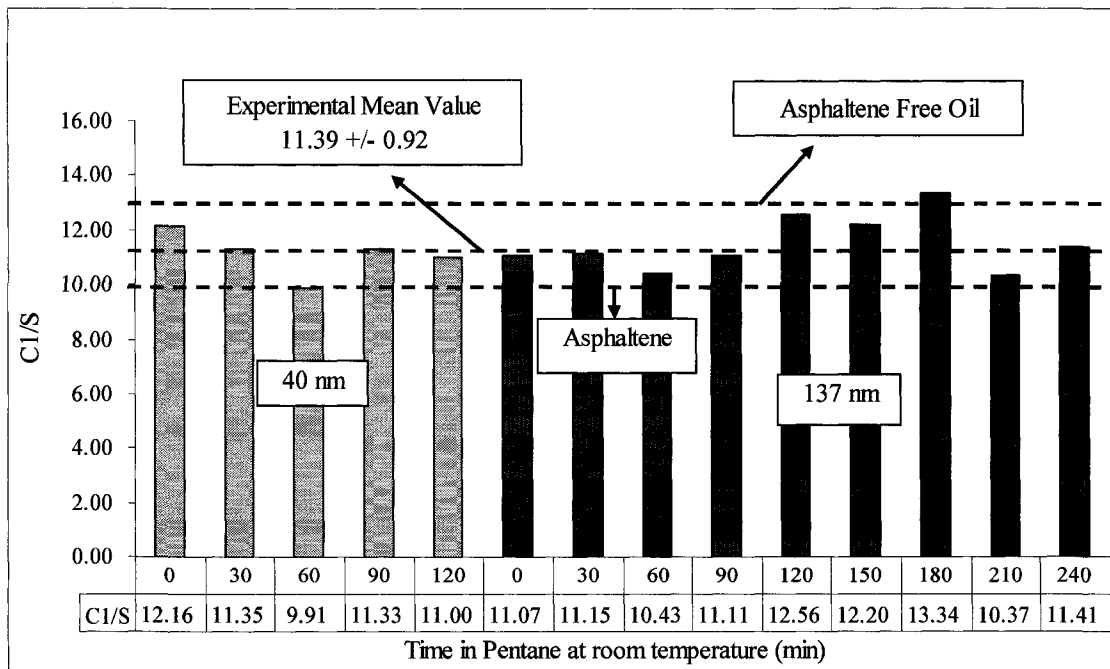


Figure 4.18: C1/S on iron oxide surface vs. t2 at t1 = 3.5 hours

The effect of ABVB mass fraction on C1/S ratio is shown in Figure 4.19. Experiments are performed over the ABVB weight percent ranging from 0 to 100 on the 137 nm thick iron oxide surface. t_1 is fixed at 3.5 hours and t_2 is fixed at 30 minutes. ABVB mass fraction has no effect on the C1/S of deposits which is ~ 11.33 nm. Again, the deposit is slightly enriched in asphaltene like materials relative to the feed. The deposits are not asphaltenes per se.

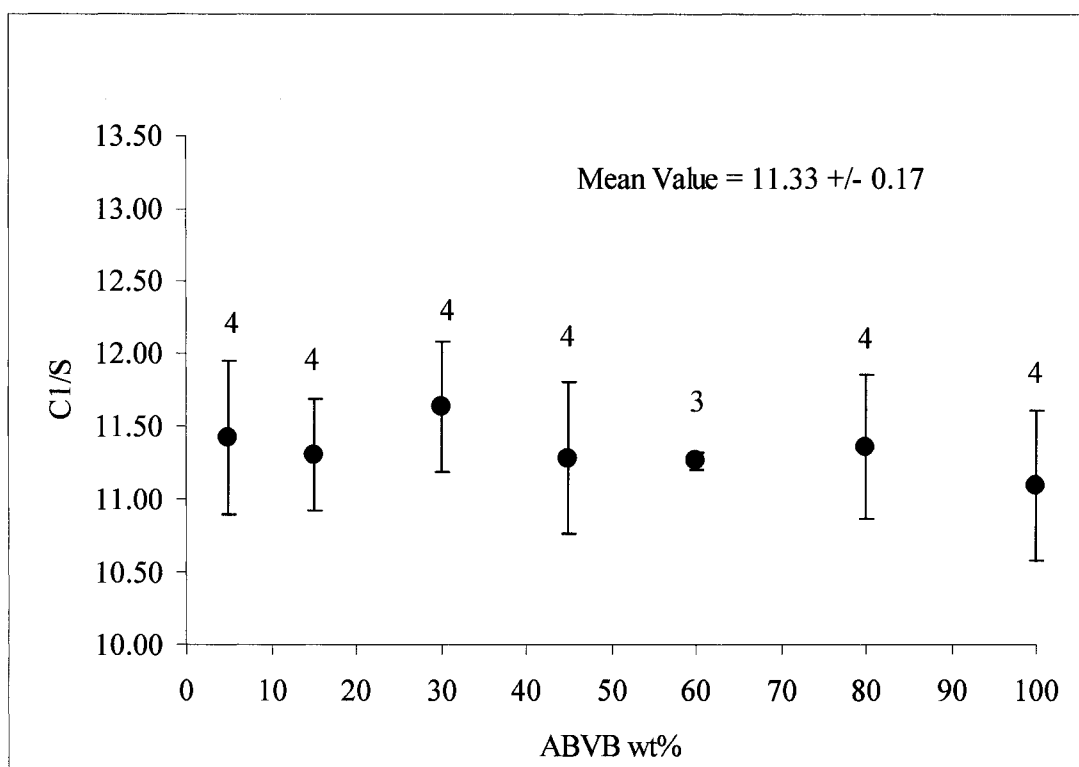


Figure 4.19: C1/S on iron oxide surface at different ABVB mass fractions in pentane

4.5.2 Composition of Deposit on Neutral Surfaces

Since neither the thickness of the film nor the time variables play a role to the

composition of deposit, the composition of deposit on nickel surface is only evaluated with variable t_1 . The thickness of the nickel film is 100 nm. t_2 is fixed at 30 minutes and ABVB composition is fixed at 15 wt %. As expected, C1/S ratio does not vary with t_1 as shown in Figure 4.20. The value of C1/S on nickel surface is ~ 11.35 which is very close to that on the iron oxide surface. Figure 4.21 shows that the C1/S on nickel surface does not vary with ABVB mass fraction either. The mean value of C1/S is ~ 11.29 over the entire composition range.

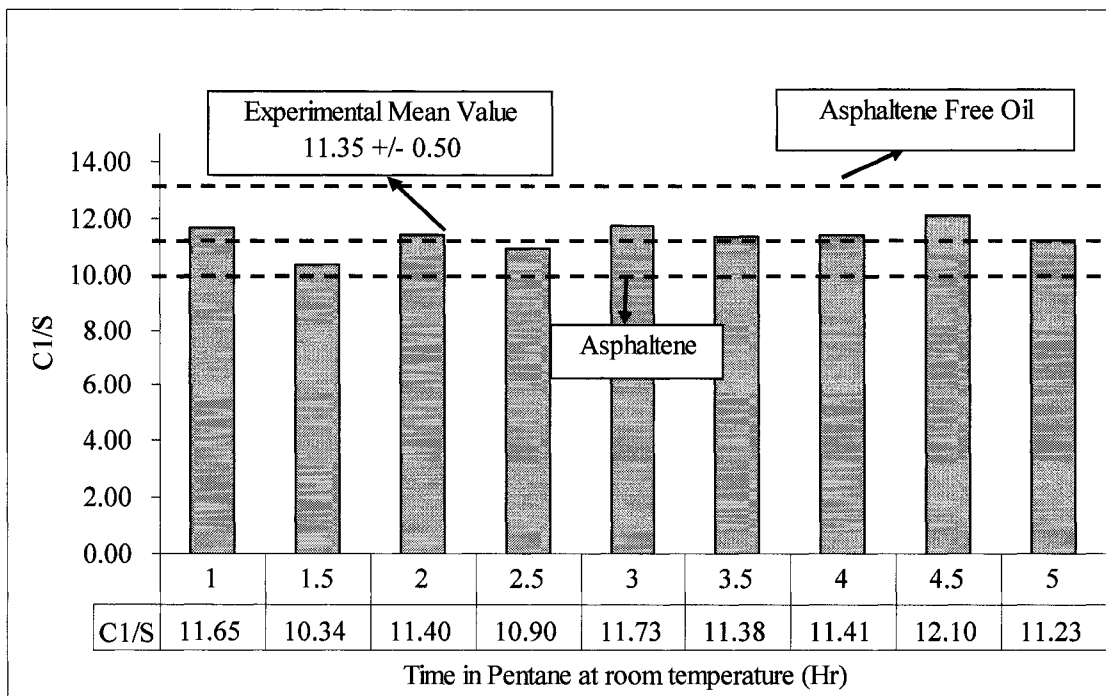


Figure 4.20: C1/S on nickel surface vs. t1 at t2 = 30 minutes and ABVB composition = 15 wt %

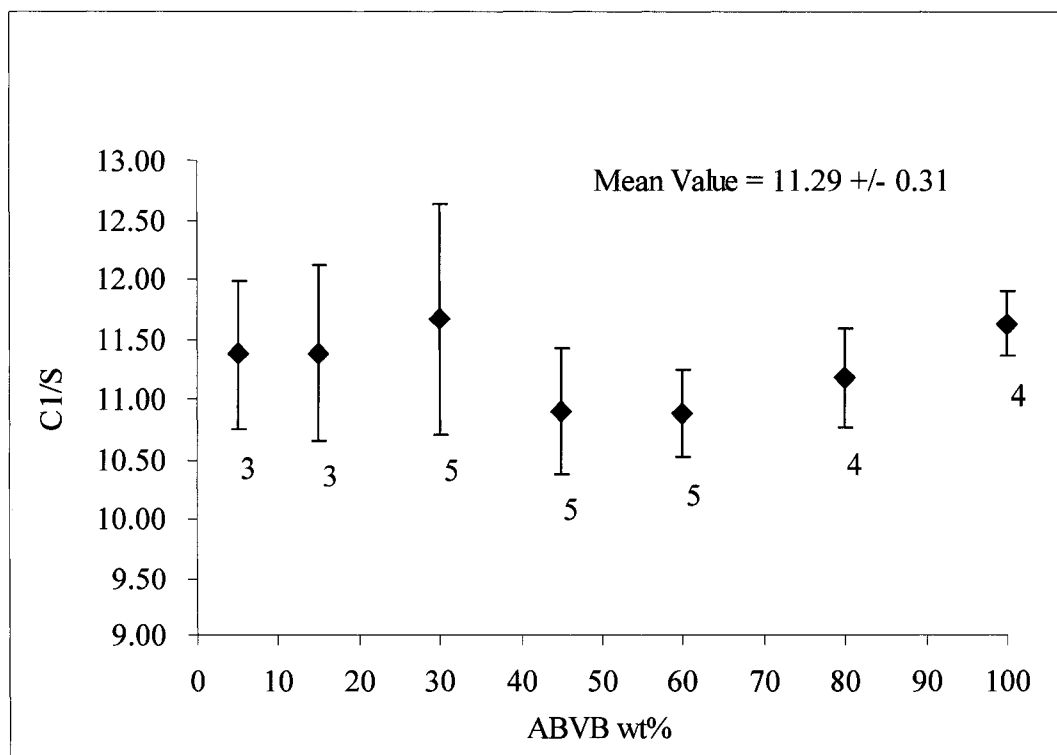


Figure 4.21: C1/S on nickel surface at different ABVB mass fractions in pentane

4.5.3 Composition of Deposit on Acidic Surfaces

The same experiments performed on nickel surfaces were also performed on silica surfaces. Figure 4.22 shows the C1/S ratio on silica surface is not affected by t_1 at fixed $t_2 = 30$ minutes and ABVB = 15 wt %. However, the value of C1/S on silica surfaces is higher (~12.63 nm). Figure 4.23 shows the C1/S ratio on silica surfaces as a function of ABVB mass fraction.

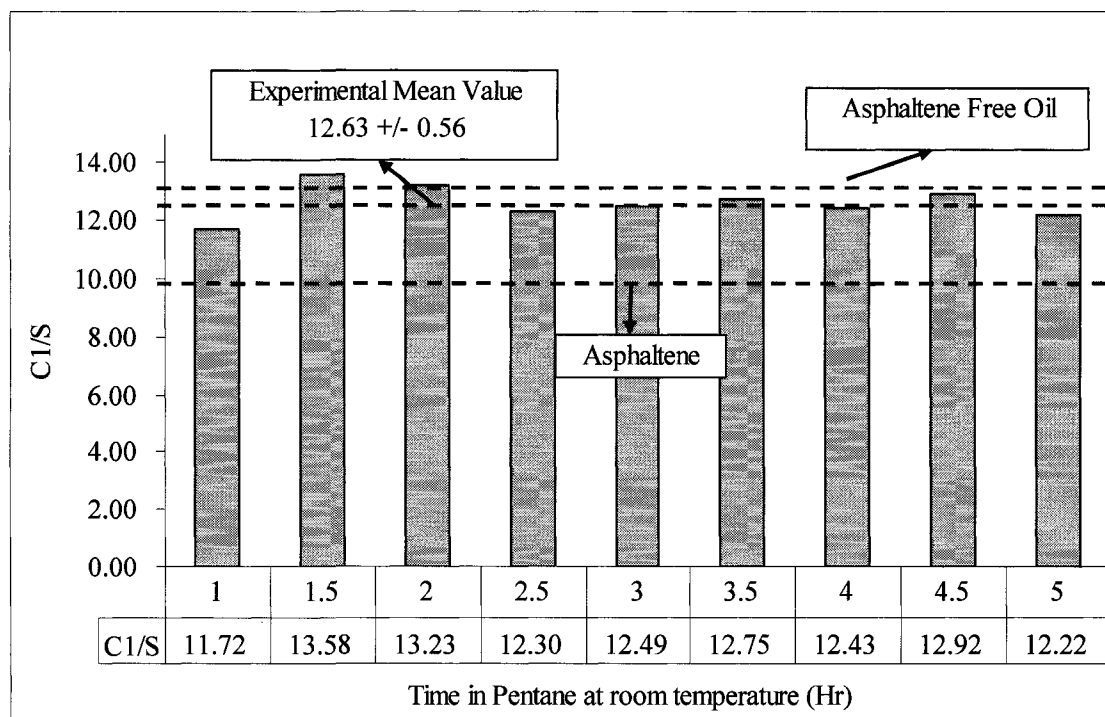


Figure 4.22: C1/S on silica surface vs. t_1 at $t_2 = 30$ minutes and ABVB composition = 15 wt %

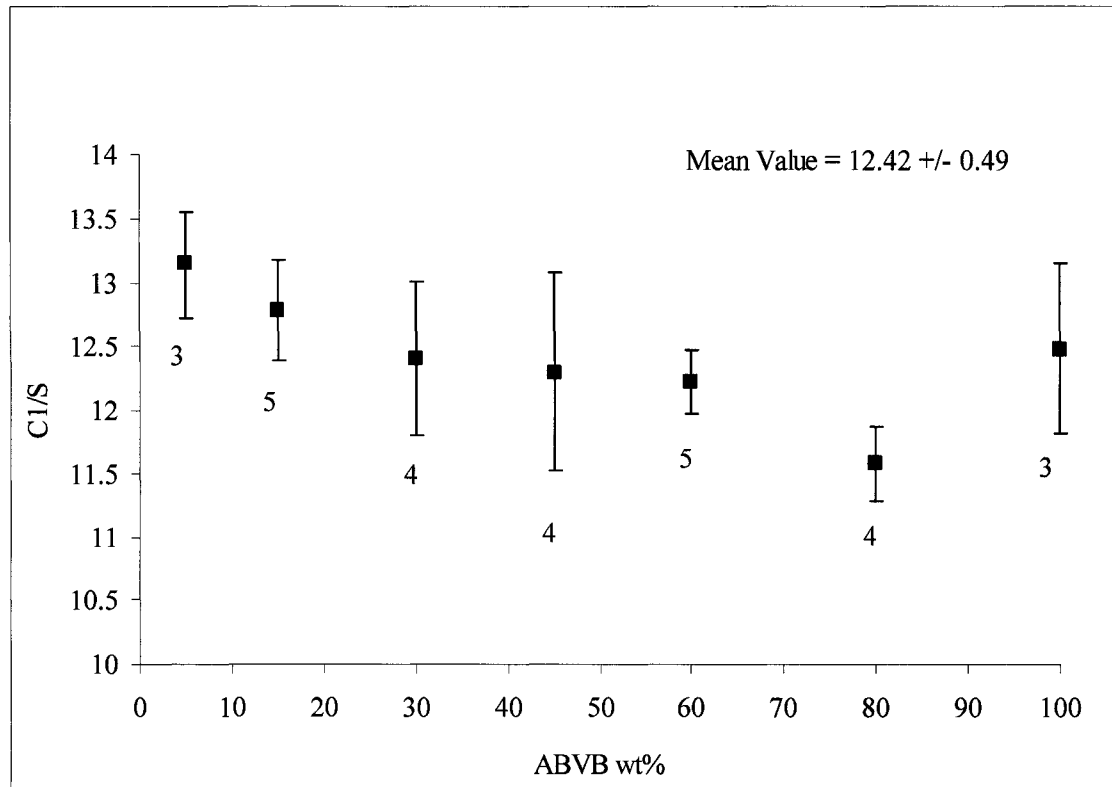


Figure 4.23: C1/S on silica surface at different ABVB mass fractions in pentane

4.5.4 Comparison of Composition of ABVB Deposits on all Surfaces

The C1/S ratios on iron oxide, nickel and silica surfaces are compared in Figure 4.24 and Figure 4.25. Figure 4.24 shows the C1/S ratio at a ABVB 15 wt %. It is evident that the ratio is highest on silica surface and more or less the same on the iron oxide and nickel surfaces. Figure 4.25 presents the C1/S ratio on all the surfaces at different ABVB mass fractions. It is again noted that the C1/S is higher on silica surface and lower but similar on the iron oxide and nickel surfaces. Mixture composition does not appear to have an appreciable effect. The connection between C1/S ratio and phase behaviour is indicated in Figure 4.26. Again there is no appreciable effect. The average C1/S ratio for sets of

experiment is shown in Table 4.11. The adherent deposits sorbed on the silica surface are enriched with maltenes, while the neutral and basic surfaces are enriched in asphaltenes relative to the feed. This effect is weak.

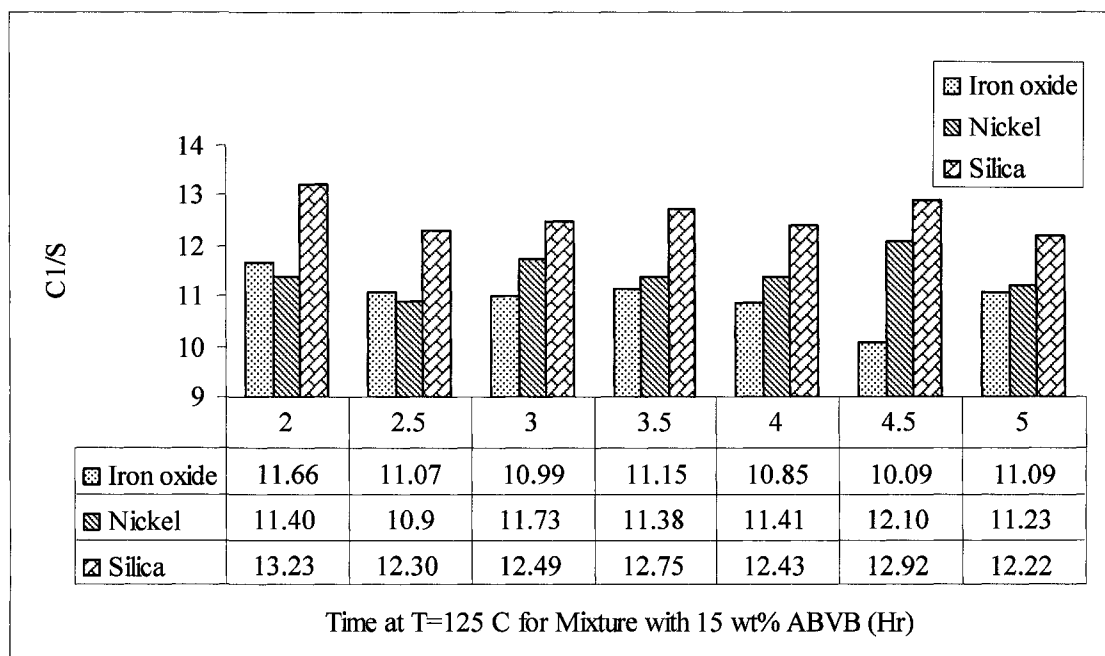


Figure 4.24: C1/S ratio vs. t1 on iron oxide, nickel and silica surfaces at t2 = 30 minutes

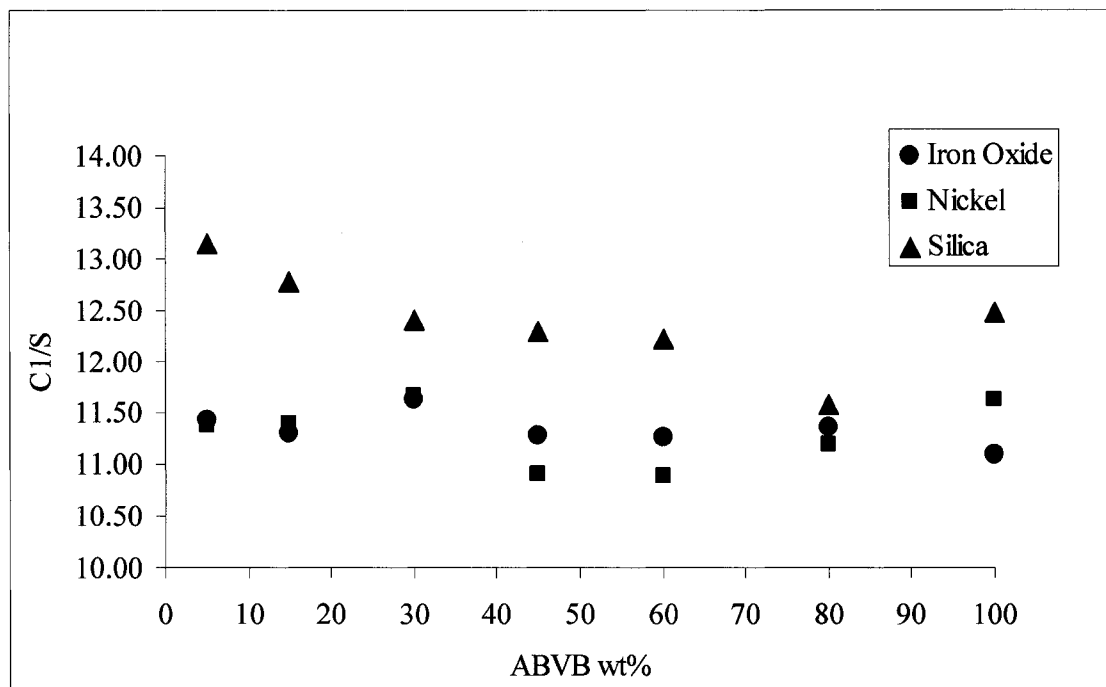


Figure 4.25: C1/S ratio on iron oxide, nickel and silica surfaces as a function of ABVB wt % in pentane

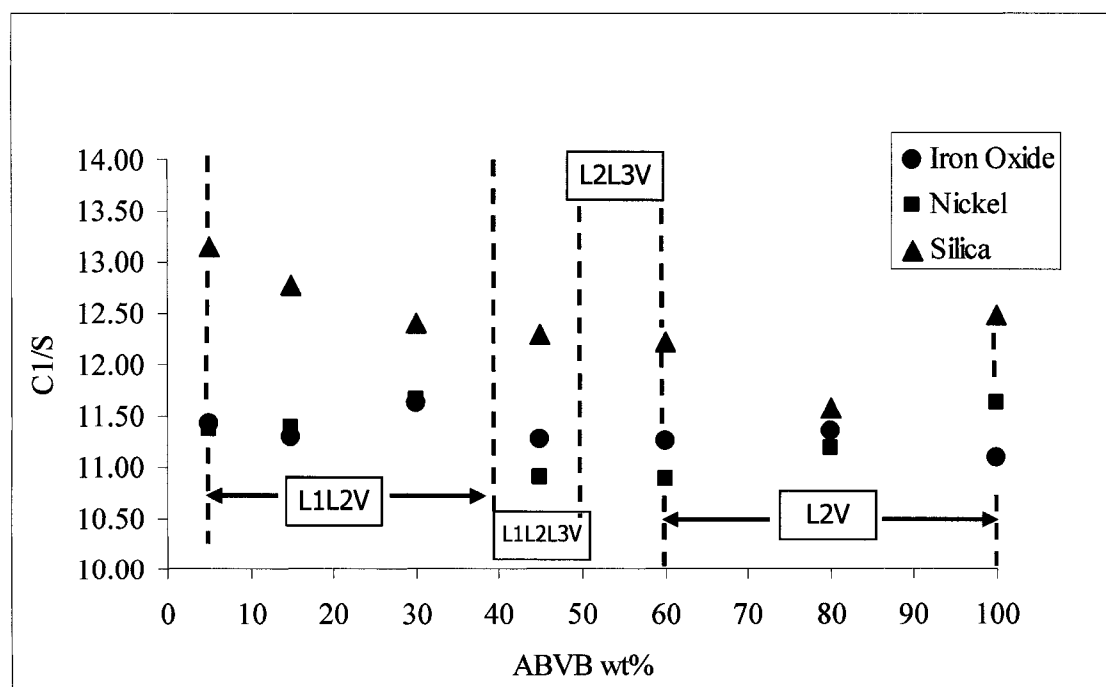


Figure 4.26: Connection between C1/S ratio and phase behaviour

Table 4.11: C1/S ratio from experiment set 1 and 2

C1/S	Experiment Set 1 (t1 as variable)		Experiment Set 2 (composition as variable)	
	t2=30 min, ABVB wt%=15%	# of Exp.	t1=3.5 hr, t2=30 min	# of Exp.
Iron Oxide	11.15 +/- 0.40	21	11.33 +/- 0.17	27
Nickel	11.35 +/- 0.50	24	11.29 +/- 0.31	29
Silica	12.63 +/- 0.56	23	12.42 +/- 0.49	28

Chapter 5 Conclusions and Future Work

5.1 Conclusions

From the discussion presented in Chapter 4, the following conclusions can be drawn:

1. Acidic, basic and neutral surfaces were prepared. Surface contamination was explored in detail and a clear understanding of surface properties was achieved. Two surfaces, notably FeO and a mixed Ni/NiO were unexpected based on the literature and the starting materials employed. Fe₂O₃ and NiO surfaces had been anticipated.
2. Contaminants on substrates were not removed during the experimental and analytical procedures.
3. Negative and positive organic deposition control experiments were performed with different model compounds. Results were consistent with expectations and suggested that the technique employed is sensitive enough to detect partial coverage and monolayer coverage on acidic or basic surfaces.
4. By contrast organic deposit composition is less well defined and the errors are significant with respect to identifying species present, whether model compounds or Athabasca vacuum residue constituents.
5. Deposit thickness for Athabasca bitumen + pentane mixtures varies with surface properties and ranges from 0.5 to 4 nm and is greatest on a strongly acidic surface and least on a neutral surface. For the surfaces tested, the order of organic deposit

thickness is $\text{SiO}_2 > \text{FeS} > \text{FeO} > \text{Ni/NiO}$. Deposit thickness also varies with mixture composition. The dependence is weak but appears to reach a maximum in the L1L2L3V zone at around 45 wt. % bitumen.

6. Substrate layer thickness and details of the experimental conditions appear to have a limited influence on deposit composition or thickness.
7. Contamination between substrate and the base of the organic deposit layer is significant and persistent.
8. Contamination on the upper surface of the organic deposit does not appear to be significant.
9. Deposits from ABVB onto basic and neutral surfaces comprise ABVB enriched in asphaltenes, while on acidic surfaces and on SiO_2 in particular, the deposit appears to be asphaltene deficient.

5.2 Future Work

Based on the present work, the following recommendations are made for the extension of this research:

1. Sample storage and handling present specific and significant challenges, in this application and for the surface science literature more broadly.
2. Speciation of surface sorbed organic species is a second challenge, which should be

pursued, even with the samples obtained from this study. Wet chemistry, and analytical techniques such as acoustic IR or ^{13}C -NMR could be applied to the species to obtain more details concerning their composition and molecular structure.

REFERENCES

1. Canada's Oil Sands. Opportunities and Challenges to 2015: An Update. In National Energy Board of Canada: June 2006.
2. Gray, M. R., Upgrading Petroleum Residues and Heavy Oils. Marcel Dekker: New York, 1994.
3. Speight, J. G., The Chemistry and Technology of Petroleum. Marcel Dekker: New York, 1999.
4. Zou, X. Y. Selective Removal of Inorganic Fine Solids, Heavy Metals and Sulfur from Bitumen/Heavy Oils. PhD Thesis. University of Toronto, 2003.
5. Gray, M. R., Hydrocarbon Fluid Properties and Processing. In University of Alberta: 2003.
6. Ali, V. A. The Impact of Phase Behaviour on Coke Formation in Delayed Cokers. University of Toronto, Toronto, 2002.
7. Richard, M. Evaluation of New Co-Volume Mixing Rules for the Peng-Robinson Equation of State. University of Alberta, Edmonton, 2007.
8. Speight, J. G., The chemical and physical structure of petroleum: effects on recovery operations. Journal of Petroleum Science and Engineering 1999, 22, (1-3), 3-15.
9. Sheu, E. Y.; Detar, M. M.; Storm, D. A.; Decanio, S. J., Aggregation and Kinetics of Asphaltenes in Organic-Solvents. Fuel 1992, 71, (3), 299-302.

10. Lian, H. J.; Lin, J. R.; Yen, T. F., Peptization Studies of Asphaltene and Solubility Parameter Spectra. *Fuel* 1994, 73, (3), 423-428.
11. Mansoori, G. A., Asphaltene, resin, and wax deposition from petroleum fluids: Mechanisms and modeling. *Arabian Journal for Science and Engineering* 1996, 21, (4B), 707-723.
12. Escobedo, J.; Mansoori, G. A. In Asphaltene and other heavy organic particle deposition during transfer and production operations, Proceedings of the 1995 SPE Annual Technical Conference, Richardson, TX, 1995; The Society of Petroleum Engineers: Richardson, TX, 1995; pp 343-358.
13. Lichaa, P. M., Asphaltene deposition problem in Venezuela crudes - usage of asphaltenes in emulsion stability. *Canadian Petroleum Technology Journal* 1977, 15.
14. Escobedo, J.; Mansoori, G. A. In Heavy Organic Deposition and Plugging of Wells (Analysis of Mexico's Experience), Proceedings of the II LAPEC, Richardson, TX, 1992, 1992; Society of Petroleum Engineers: Richardson, TX, 1992.
15. Escobedo, J.; Mansoori, G. A.; Balderas-Joers, C.; Carranza-Becerra, L. J.; Mendez-Garcia, M. A. In Heavy organic deposition during oil production from a hot deep reservoir: A field experience, Proceedings of the 5th Latin American and Caribbean Petroleum Engineering Conference and Exhibition, 1997; The Society of Petroleum Engineers: 1997.

16. Reynolds, J. G., Metals and heteroatoms in heavy oils. In *Petroleum Chemistry and Refining*, Speight, J. G., Ed. Taylor & Francis Press: Washington DC, 1999.
17. Reynolds, J. G., Effects of asphaltene precipitation on the size of Vanadium-, Nickel- and Sulfur-containing compounds in heavy crude oils and residua; Asphaltenes and asphalts, 1. In Yen, T. F.; Chilingarian, G. V., Eds. Elsevier Science Press: New York, 1994.
18. Yen, T. F., Genesis and Degradation of Petroleum Hydrocarbons in Marine Environments. *ACS Symposium Series* 1975, (18), 231-266.
19. Zou, X. Y.; Shaw, J. M., The Phase Behavior of Athabasca Bitumen Vacuum Bottoms + Alkane Solvent Systems. In *HOD 2002*, Mexico.
20. Speight, J. G.; Francisco, M. A., Studies in Petroleum Composition - Changes in the Nature of Chemical-Constituents during Crude-Oil Distillation. *Revue De L Institut Francais Du Petrole* 1990, 45, (6), 733-740.
21. Speight, J. G., Petroleum asphaltenes - Part 2 - The effect of asphaltenes and resin constituents on recovery and refining processes. *Oil & Gas Science and Technology-Revue De L Institut Francais Du Petrole* 2004, 59, (5), 479-488.
22. Chung, K. H.; Xu, C. M.; Hu, Y. X.; Wang, R. N., Supercritical fluid extraction reveals resid properties. *Oil & Gas Journal* 1997, 95, (3), 66-69.
23. Zhao, B.; Shaw, J. M., Composition and size distribution of coherent nanostructures in Athabasca bitumen and Maya crude oil. *Energy & Fuels* 2007, 21, (5), 2795-2804.

24. Mullins, O. C.; Sheu, E. Y.; Hammami, A.; Marshall, A. G., *Asphaltenes, Heavy Oils and Petroleomics*. Springer: New York, 2007.
25. Long, R. B., *Chemistry of Asphaltenes*. American Chemical Society: 1981.
26. Long, R. B., *The Concept of Asphaltenes*. *Advances in Chemistry Series* 1981, (195), 17-27.
27. Sheu, E. Y.; Detar, M. M.; Storm, D. A., *Interfacial Properties of Asphaltenes*. *Fuel* 1992, 71, (11), 1277-1281.
28. Storm, D. A.; Sheu, E. Y., *Characterization of Colloidal Asphaltene Particles in Oil*. *Fuel* 1995, 74, (8), 1140-1145.
29. Maham, Y.; Chodakowski, M. G.; Zhang, X. H.; Shaw, J. M., *Asphaltene phase behavior: prediction at a crossroads*. *Fluid Phase Equilibria* 2005, 227, (2), 177-182.
30. Wiehe, I. A., *The Pendant Core Building-Block Model of Petroleum Residue*. *Energy & Fuels* 1994, 8, (3), 536-544.
31. Speight, J. G., *The Chemistry and Technology of Coal*. Marcel Dekker: New York, 1994.
32. Kim, H. G.; Long, R. B., *Characterization of Heavy Residuum by a Small-Angle X-Ray-Scattering Technique*. *Industrial & Engineering Chemistry Fundamentals* 1979, 18, (1), 60-63.
33. Zhao, S.; Kotlyar, L. S.; Woods, J. R.; Sparks, B. D.; Hardacre, K.; Chung, K. H., *Molecular transformation of Athabasca bitumen end-cuts during coking and*

- hydrocracking. *Fuel* 2001, 80, (8), 1155-1163.
34. Murgich, J.; Abanero, J. A.; Strausz, O. P., Molecular recognition in aggregates formed by asphaltene and resin molecules from the Athabasca oil sand. *Energy & Fuels* 1999, 13, (2), 278-286.
 35. Strausz, O. P.; Mojelsky, T. W.; Lown, E. M., The Molecular-Structure of Asphaltene - An Unfolding Story. *Fuel* 1992, 71, (12), 1355-1363.
 36. Sheremata, J. M.; Gray, M. R.; Dettman, H. D.; McCaffrey, W. C., Quantitative molecular representation and sequential optimization of athabasca asphaltenes. *Energy & Fuels* 2004, 18, (5), 1377-1384.
 37. Li, S. H.; Liu, C. G.; Que, G. H.; Liang, W. J.; Zhu, Y. J., Colloidal structures of three Chinese petroleum vacuum residues. *Fuel* 1996, 75, (8), 1025-1029.
 38. Bardon, C.; Barre, L.; Espinat, D.; Guille, V.; Li, M. H.; Lambard, J.; Ravey, J. C.; Rosenberg, E.; Zemb, T., The colloidal structure of crude oils and suspensions of asphaltenes and resins. *Fuel Science & Technology International* 1996, 14, (1-2), 203-242.
 39. Branco, V. A. M.; Mansoori, G. A.; Xavier, L. C. D.; Park, S. J.; Manafi, H., Asphaltene flocculation and collapse from petroleum fluids. *Journal of Petroleum Science and Engineering* 2001, 32, (2-4), 217-230.
 40. Priyanto, S.; Mansoori, G. A.; Suwono, A., Measurement of property relationships of nano-structure micelles and coacervates of asphaltene in a pure solvent. *Chemical Engineering Science* 2001, 56, (24), 6933-6939.

41. Pacheco-Sanchez, J. H.; Mansoori, G. A., Prediction of the phase behavior of asphaltene micelle aromatic hydrocarbon systems. *Petroleum Science and Technology* 1998, 16, (3-4), 377-394.
42. Rogacheva, O. V.; Rimaev, R. N.; Gubaidullin, V. Z.; Khakimov, D. K., Investigation of The Surface-Activity of The Asphaltenes of Petroleum Residues. *Colloid Journal of the Ussr* 1980, 42, (3), 490-493.
43. Sheu, E. Y.; Liang, K. S.; Sinha, S. K.; Overfield, R. E., Polydispersity Analysis of Asphaltene Solutions in Toluene. *Journal of Colloid and Interface Science* 1992, 153, (2), 399-410.
44. Leontaritis, K. J.; Mansoori, G. A. In *Asphaltene Deposition During Oil Production and Processing: A Thermodynamic Colloidal Model*, SPE International Symposium on Oilfield Chemistry, San Antonio, TX, 1987; Society of Petroleum Engineers: San Antonio, TX, 1987.
45. Andersen, S. I.; Stenby, E. H., Thermodynamics of asphaltene precipitation and dissolution investigation of temperature and solvent effects. *Fuel Science & Technology International* 1996, 14, (1-2), 261-287.
46. Mohamed, R. S.; Loh, W.; Ramos, A. C. S.; Delgado, C. C.; Almeida, V. R., Reversibility and inhibition of asphaltene precipitation in Brazilian crude oils. *Petroleum Science and Technology* 1999, 17, (7-8), 877-896.
47. Kokal, S. L.; Najman, J.; Sayegh, S. G.; George, A. E., Measurement and Correlation of Asphaltene Precipitation from Heavy Oils by Gas Injection. *Journal*

- of Canadian Petroleum Technology 1992, 31, (4), 24-30.
48. Buckley, J. S. Sill North American Chemical Congress; 1997.
 49. Hammami, A.; Changyen, D.; Nighswander, J. A.; Stange, E., An Experimental-Study of The Effect of Paraffinic Solvents on The Onset and Bulk Precipitation of Asphaltenes. Fuel Science & Technology International 1995, 13, (9), 1167-1184.
 50. Chung, F. T.-H.; Sarathi, P.; Jones, R. Modeling of Asphaltene and Wax Precipitation; NIPER-498: 1991.
 51. Hischberg, A.; de Jong, L. N. J.; Schipper, B. A.; Meijers, J. G., Influence of temperature and pressure on asphaltene precipitation. Society of Petroleum Engineers 1984, 283.
 52. Hsu, C. S.; Dechert, G. J.; Robbins, W. K.; Fukuda, E. K., Naphthenic acids in crude oils characterized by mass spectrometry. Energy & Fuels 2000, 14, (1), 217-223.
 53. Gutzeit, J., Naphthenic Acid Corrosion in Oil Refineries. Materials Performance 1977, 16, (10), 24-35.
 54. Slavcheva, E.; Shone, B.; Turnbull, A., Review of naphthenic acid corrosion in oil refining. British Corrosion Journal 1999, 34, (2), 125-131.
 55. Strausz, O. P. AOSTRA/University Reports for Industry Agreement; 1979.
 56. Brandal, O.; Sjoblom, J., Interfacial behavior of naphthenic acids and multivalent cations in systems with oil and water. II: Formation and stability of metal naphthenate films at oil-water interfaces. Journal of Dispersion Science and

- Technology 2005, 26, (1), 53-58.
57. Piehl, R. L., Naphthenic Acid Corrosion in Crude Distillation Units. *Materials Performance* 1988, 27, (1), 37-43.
 58. Pathak, A. K.; Kumar, T. In *Study of Indigenous Crude Oil Emulsions and their Stability*, Proceedings of PETROTECH-95, New Delhi, 1995; *Technology Trends in Oil Industry*: New Delhi, 1995; pp 217-224.
 59. Acevedo, S.; Escobar, G.; Ranaudo, M. A.; Khazen, J.; Borges, B.; Pereira, J. C.; Mendez, B., Isolation and characterization of low and high molecular weight acidic compounds from Cerro Negro extraheavy crude oil. Role of these acids in the interfacial properties of the crude oil emulsions. *Energy & Fuels* 1999, 13, (2), 333-335.
 60. Ese, M. H.; Kilpatrick, P. K., Stabilization of water-in-oil emulsions by naphthenic acids and their salts: Model compounds, role of pH, and soap: Acid ratio. *Journal of Dispersion Science and Technology* 2004, 25, (3), 253-261.
 61. Dzidic, I.; Somerville, A. C.; Raia, J. C.; Hart, H. V., Determination of Naphthenic Acids in California Crudes and Refinery Wastewaters by Fluoride-Ion Chemical Ionization Mass-Spectrometry. *Analytical Chemistry* 1988, 60, (13), 1318-1323.
 62. Fan, T. P., Characterization of Naphthenic Acids in Petroleum by Fast-Atom-Bombardment Mass-Spectrometry. *Energy & Fuels* 1991, 5, (3), 371-375.
 63. Wong, D. C. L.; vanCompernelle, R.; Nowlin, J. G.; Oneal, D. L.; Johnson, G. M., Use of supercritical fluid extraction and fast ion bombardment mass spectrometry

- to identify toxic chemicals from a refinery effluent adsorbed onto granular activated carbon. *Chemosphere* 1996, 32, (8), 1669-1679.
64. Gabryelski, W.; Froese, K. L., Characterization of naphthenic acids by electrospray ionization high-field asymmetric waveform ion mobility spectrometry mass spectrometry. *Analytical Chemistry* 2003, 75, (17), 4612-4623.
 65. St John, W. P.; Rughani, J.; Green, S. A.; McGinnis, G. D., Analysis and characterization of naphthenic acids by gas chromatography electron impact mass spectrometry of tert.-butyldimethylsilyl derivatives. *Journal of Chromatography A* 1998, 807, (2), 241-251.
 66. Holowenko, F. M.; MacKinnon, M. D.; Fedorak, P. M., Characterization of naphthenic acids in oil sands wastewaters by gas chromatography-mass spectrometry. *Water Research* 2002, 36, (11), 2843-2855.
 67. Seifert, W. K., *Carboxylic acids in petroleum and sediments*. Springer-Verlag: Berlin, Germany, 1975; Vol. 32.
 68. Tomczyk, N. A.; Winans, R. E.; Shinn, J. H.; Robinson, R. C., On the nature and origin of acidic species in petroleum. 1. Detailed acid type distribution in a California crude oil. *Energy & Fuels* 2001, 15, (6), 1498-1504.
 69. Rudzinski, W. E.; Oehlers, L.; Zhang, Y., Tandem mass spectrometric characterization of commercial naphthenic acids and a Maya crude oil. *Energy & Fuels* 2002, 16, (5), 1178-1185.
 70. Robbins, W. K., Challenges in the characterization of naphthenic acids in

- petroleum. Abstracts of Papers of the American Chemical Society 1998, 215, U119-U119.
71. Brient, J. A., Commercial utility of naphthenic acids recovered from petroleum distillates. Abstracts of Papers of the American Chemical Society 1998, 215, U119-U119.
 72. Turnbull, A.; Slavcheva, E.; Shone, B., Factors controlling naphthenic acid corrosion. *Corrosion* 1998, 54, (11), 922-930.
 73. Yopez, O., On the chemical reaction between carboxylic acids and iron, including the special case of naphthenic acid. *Fuel* 2007, 86, (7-8), 1162-1168.
 74. Rousseau, G.; Zhou, H.; Hurtevent, C., Calcium Carbonate and Naphthenate Mixed Scale in Deep-offshore Fields. In *SPE Oilfield Scale Symposium, Aberdeen, U.K., 2001; Vol. SPE 68307*.
 75. Vindstad, J. E.; Bye, A. S.; Grande, K. V.; Hustad, B. M.; Hustvedt, E.; Nergaard, B., Fighting naphthenate deposition at the Statoil-operated heidrun field. In *SPE 5th International Symposium on Oilfield Scale, Aberdeen, U.K., 2003; Vol. SPE 80375*.
 76. S. J. Dyer, G. M. G. a. C. A. In *Proc.-SPE 5th Int. Symp. on Oilfield Scale, Aberdeen, 2003; SPE 80395: Aberdeen, 2003*.
 77. Lutnaes, B. F.; Brandal, O.; Sjoblom, J.; Krane, J., Airchzeal C-80 isoprenoid tetraacids responsible for naphthenate deposition in crude oil processing. *Organic & Biomolecular Chemistry* 2006, 4, (4), 616-620.

78. Brandal, O.; Hanneseth, A. M.; Hemmingsen, P. V.; Sjoblom, J.; Kim, S.; Rodgers, R. P.; Marshall, A. G., Isolation and characterization of naphthenic acids from a metal naphthenate deposit: Molecular properties at oil-water and air-water interfaces. *Journal of Dispersion Science and Technology* 2006, 27, (3), 295-305.
79. Poggesi, G.; Hurtevent, C.; and Buchart, D., Multifunctional Chemicals for West African Deep Offshore Fields. In *SPE Oilfield Scale Symposium*, Aberdeen, U.K., 2002; Vol. SPE 74649.
80. Gallup, D. L., Soap sludges: Aggravating Factors and Mitigation Measures. In *6th SPE Oilfield Scale Symposium*, Aberdeen, U.K., 2004; Vol. SPE 87471.
81. Hanneseth, A. M. D.; Brandal, O.; Sjoblom, J., Formation, growth, and inhibition of calcium naphthenate particles in oil/water systems as monitored by means of near infrared spectroscopy. *Journal of Dispersion Science and Technology* 2006, 27, (2), 185-192.
82. <http://wordnet.princeton.edu/perl/webwn?o2=&o0=1&o7=&o5=&o1=1&o6=&o4=&o3=&s=surface&i=0&h=0000000000#c>.
83. Lewis, G., *Valence and the Structure of Atoms and Molecules*. The Chemical Catalog Company, inc.: 1923.
84. Laidler, K. J.; Meiser, J. H.; Sanctuary, B. C., *Physical Chemistry*. Houghton Mifflin Company: 2002.
85. Kallay, N., *Interfacial Dynamics*. CRC Press: 2000.

86. Gonzalez, M. F.; Stull, C. S.; Lopez-Linares, F.; Pereira-Almao, P., Comparing asphaltene adsorption with model heavy molecules over macroporous solid surfaces. *Energy & Fuels* 2007, 21, (1), 234-241.
87. Crocker, M. E.; Marchin, L. M., Wettability and Adsorption Characteristics of Crude-Oil Asphaltene and Polar Fractions. *Journal of Petroleum Technology* 1988, 40, (4), 470-474.
88. Pernyeszi, T.; Patzko, A.; Berkesi, O.; Dekany, I., Asphaltene adsorption on clays and crude oil reservoir rocks. *Colloids and Surfaces a-Physicochemical and Engineering Aspects* 1998, 137, (1-3), 373-384.
89. Aske, N. Characterisation of Crude Oil Components, Asphaltene Aggregation and Emulsion Stability by means of Near Infrared Spectroscopy and Multivariate Analysis. Norwegian University of Science and Technology, 2002.
90. Mullins, O. C.; Sheu, E. Y., Structures and Dynamics of Asphaltenes. Springer: 1998.
91. Young, E. C.; Maeng, J. Y.; Seun K. Formation of Highly Ordered Organic Monolayers by Dative Bonding: Pyridine on Ge(100). *Journal of American Chemical Society*. 2003, 125, 7514..
92. Mate, C. M.; Somorjai, G. A.; Tom, H. W.; Zhu, X. D.; Shen, Y.R., Electron correlation described by extended geminal models. *Journal of Chemical Physics*. 1988, 88, 441.
93. Sanchez-Delgado R.A., Organometallic Modelling of the Hydrodesulfurization

and Hydrodenitrogenation Reactions. Kluwer. The Netherlands, 2002.

94. Abdallah, W.; Nelson, A., Pyrrole adsorption and reaction on Mo(110) and C/N - Mo(110). Surface Science 585 (2005) 113 - 122.
95. Abdallah, W.; Nelson, A.; Gray, M., Pyridine adsorption and reaction on Mo(110) and C/N - Mo(110): experiment and modeling. Surface Science 569 (2004) 193 - 206.
96. Abdallah, W., Nelson, A., Density Functional Theory Study of Pyrrole Adsorption on Mo(110). Journal of Physical Chemistry. 2005, 109, 10863-10870
97. Jaeger, R. C., Introduction to Microelectronic Fabrication. Prentice Hall: New Jersey, 2002.
98. http://www.enma.umd.edu/LAMP/Sop/Piranha_SOP.htm.
99. Mattox, D. M., The foundation of vacuum coating technology. William Andrew: Norwich, New York, 2003.
100. Ohring, M., The Materials Science of Thin Films. Academic Pr: 2001.
101. http://en.wikipedia.org/wiki/X-ray_photoelectron_spectroscopy.
102. Ebel, H.; Pohn, C.; Svagera, R.; Wernle, M. E.; Ebel, M. F.; Jablonski, A., Calculation of Escape Depths from Inelastic Mean Free Paths. Journal of Electron Spectroscopy and Related Phenomena 1990, 50, (1-2), 109-116.